

Fluid-Rock Characterization for NMR Well Logging and Special Core Analysis

1st Annual Report

October 1, 2004 – September 30, 2005

George J. Hirasaki (gjh@rice.edu)

and

Kishore K. Mohanty (mohanty@uh.edu)

Issued: November, 2005

DE-FC26-04NT15515

Project Officer:
Chandra Nautiyal, Tulsa

Contract Officer:
Thomas J. Gruber, Pittsburg

Rice University
6100 Main Street
Houston, TX 77005

University of Houston
4800 Calhoun Road
Houston, TX 77204-4004

DISCLAIMER* — The Disclaimer must follow the title page, and must contain the following paragraph:

"This report was prepared as an account of work sponsored by an agency of the United States Government. Neither the United States Government nor any agency thereof, nor any of their employees, makes any warranty, express or implied, or assumes any legal liability or responsibility for the accuracy, completeness, or usefulness of any information, apparatus, product, or process disclosed, or represents that its use would not infringe privately owned rights. Reference herein to any specific commercial product, process, or service by trade name, trademark, manufacturer, or otherwise does not necessarily constitute or imply its endorsement, recommendation, or favoring by the United States Government or any agency thereof. The views and opinions of authors expressed herein do not necessarily state or reflect those of the United States Government or any agency thereof."

ABSTRACT

Abstract for Project

NMR well logging provides a record of formation porosity, permeability, irreducible water saturation, oil saturation and viscosity. In the absence of formation material, the NMR logs are interpreted using default assumptions. Special core analysis on core samples of formation material provides a calibration between the log response and the desired rock and/or fluid property. The project proposes to develop interpretations for reservoirs that do not satisfy the usual assumptions inherent in the interpretation. Also, NMR will be used in special core analysis to investigate the mechanism of oil recovery by wettability alteration and the relative permeability of non-water-wet systems.

Some common assumptions and the reality of exceptional reservoirs are listed in the following and will be addressed in this project.

- (1) *Assumption:* in situ live crude oil and OBM have a relaxation time proportional to temperature/viscosity as correlated from stock tank oils. *Reality:* methane and ethane relax by a different mechanism than for dead oil and GOR is a parameter; carbon dioxide does not respond to proton NMR but influences oil and gas viscosity and relaxation rates.
- (2) *Assumption:* the in situ hydrocarbons have a relaxation time equal to that of the bulk fluid, i.e. there is no surface relaxation as if the formation is water-wet. *Reality:* Most oil reservoirs are naturally mixed-wet and drilling with oil-based mud (OBM) sometimes alters wettability. If the formation is not water-wet, surface relaxation of the hydrocarbon will result.
- (3) *Assumption:* OBM filtrate has the properties of the base oil. *Reality:* OBM filtrate often has some level of the oil-wetting additives and in some cases has paramagnetic particles. It may also have dissolved gas.
- (4) *Assumption:* the magnetic field gradient is equal to that of the logging tool. *Reality:* paramagnetic minerals may result in internal magnetic field gradient much greater than that of the logging tool.
- (5) *Assumption:* pores of different size relax independently. *Reality:* clay lined pores can have significant diffusional coupling between microporosity and macroporosity.

Abstract for 1st-Annual Report

Progress is reported on Tasks: (1.2) Properties of oil-based drilling fluids, (2.2) Application of restricted diffusion for characterization of vuggy carbonate formations, (2.4) Interpretation of systems with diffusional coupling between pores, and (3) Characterization of pore structure and wettability.

TABLE OF CONTENTS

DISCLAIMER.....	2
ABSTRACT.....	3
EXECUTIVE SUMMARY	5
Subtask 1.2: Properties of oil-based drilling fluids.....	8
Subtask 2.2: Application of restricted diffusion for characterization of vuggy carbonate formations.....	33
Subtask 2.4: Interpretation of systems with diffusional coupling between pores.....	111
Task 3: Characterization of pore structure and wettability.	136

EXECUTIVE SUMMARY

Subtask 1.2: Properties of oil-based drilling fluids.

Oil-based drilling fluids can invade formations and contaminate crude oils, hindering logging analysis. This work details ^1H NMR T_2 measurements with mixtures of one drilling-fluid base oil, NovaPlus (SNP), and crude oils to determine the effect of the contamination. Measurements are made using 2 MHz MARAN bench-top instruments on mixtures having various concentrations of SNP, with each of three crude oils (labeled STNS, SMY, and PBB), whose viscosities range from 13.7 to 207 cp. T_2 measurements for mixtures containing SMY and SNP are repeated four times for purpose of statistical analysis.

Two approaches are explored to better relate NMR measurements with contamination. In the first approach, a selective contamination index (SCI) is defined that relates the T_2 distribution to the contamination. Here, a subset of the T_2 data is chosen for analysis based on sensitivity to contamination. In the second approach, the T_2 data are fit to a four-parameter, skewed Gaussian model for T_2 distributions. Two parameters of the model are combined in a distribution parameter index (DPI), which can be related to contamination.

Both the SCI and DPI values can be fit using cubic polynomials, resulting in a functional dependence on concentration. The polynomial functions, used in reverse, yield estimations of the degree of contamination, which for SMY-SNP mixtures are compared to standard $T_{2,LM}$ methods. The comparison of the $T_{2,LM}$, SCI, and DPI methods is done in terms of the estimated error in the degree of contamination. The SCI method provides the best estimate of contamination.

Subtask 2.2: Application of restricted diffusion for characterization of vuggy carbonate formations.

Restricted diffusion measurements have the potential to measure size and connectivity between pores. A method was developed to estimate the relaxation time and size distribution of a system of spheres. A single set of NMR diffusion parameters is sensitive to only a limited range of sphere sizes. Thus a multiple sets of NMR parameters are required to estimate a wide distribution of sphere sizes. The results from each set are combined use of a mask that limits inclusion of only valid results. This results in a composite map of T_2 and sphere size.

Interpretations of carbonate rock and sandpacks were ambiguous because of the difficulty of obtaining fluids and parameters over a wide enough range. However, the method was successful in estimating the drop size distribution of water in oil emulsion.

Subtask 2.4: Interpretation of systems with diffusional coupling between pores.

Pore structure analysis by NMR relaxation assumes that the T_1 or T_2 distribution is directly related to the pore size distribution. This assumption breaks down if the fluid in different sized pores is coupled through diffusion. In such cases, the estimation of formation properties such as permeability and irreducible water saturation using the traditional $T_{2,\text{cutoff}}$ method would give erroneous results. Several techniques like "spectral" BVI and tapered $T_{2,\text{cutoff}}$ have been introduced to take into account the effects of diffusional coupling for better estimation of properties.

We aim to provide a theoretical and experimental understanding of NMR relaxation in systems with diffusional coupling between micro- and macropores. Relaxation is modeled such that the fluid molecules relax at the surface of micropores and simultaneously diffuse between the two pore types. The T_2 distribution of the pore is a function of several parameters including micropore surface relaxivity, fluid diffusivity and pore geometry. The governing parameters are combined in a single coupling parameter (α) which is defined as the ratio of the characteristic relaxation rate of the pore system to the rate of diffusional mixing of fluid molecules between micro- and macropores. It is shown that depending on the value of α , the two pore types can communicate through total, intermediate or decoupled regimes of coupling.

The model is applied to treat diffusional coupling in sandstones with a distribution of macropores lined with clay flakes. Simulations are verified by comparing with experimental results for chlorite coated, North-Burbank sandstone. It is observed that the T_1 distribution shows a bimodal distribution at 100% water saturation but a unimodal distribution when saturated with hexane. This occurs because the extent of coupling is higher for hexane than for water due to lower relaxivity and higher diffusivity of hexane. The α values indicate intermediate coupling for water and strong coupling for hexane.

The model is also applied to grainstone carbonates with intra and intergranular porosity. In this case, α is found to have a quadratic dependence on grain radius and inverse dependence on micropore radius. The theory is experimentally validated on several systems with microporous particles of varying grain diameters and known microporosities. Here too, the T_2 distribution at 100% water saturation varies from bimodal for coarse-grained particles to unimodal for fine-grained particles. The transition from bimodal to unimodal distribution is also predicted theoretically from the values of α .

Task 3: Characterization of pore structure and wettability.

Characterization of pore structure has been completed on 6 carbonate samples. The vug size, distribution and interconnection vary significantly in these six samples. The thin sections have been characterized through their two-point correlation function, chord size distribution and lineal path function. The image analysis using Fourier transform and erosion-dilation algorithms has been completed. The work on NMR response, electrical conductivity and brine permeability has been initiated. We are working on reconstructing three-dimensional pore structures, wettability and relative permeability of these rock samples.

SUBTASK 1.2: Effect of Drilling-Mud Base-Oil Contamination on Crude Oil T_2 Distributions

Motivation and Approach

Oil wells are often drilled with the aid of oil-based fluids. During the drilling process, an oil-based mud (OBM) is formed from the mixture of drilling fluid and drill cuttings. Filtrates from these oil-based muds invade oil-bearing formations and mix with crude oils. OBM filtrates alter the properties of the crude oils with which they mix. In NMR well logging, one concern is whether the measured T_2 relaxation time distribution (or T_2 distribution) changes enough to affect the estimated viscosity, which can be derived from these measurements through existing correlations. Such concerns are particularly valid because OBM filtrates are similar in molecular structure to the crude oils themselves. This inhibits attempts to separate the OBM filtrate signal from the crude oil signal in NMR logs.

Other works have addressed using NMR to investigate OBM contamination of crude oils, mostly in the context of the pumpout phase of downhole fluid sampling. Bouton, *et al.* (2001) developed a sharpness parameter to characterize T_1 relaxation times of mixtures of crude oils and base oils. Base oils are the predominant component in OBM filtrates. The sharpness parameter is at a maximum for the base oil alone and decreases monotonically for higher concentrations of crude oil. Continuing this work, Masak, *et al.* (2002) use a downhole fluid sampler to characterize contamination by measuring T_1 relaxation times during the pumpout process. Here, measurements occur as time progresses, and the change in measured signal amplitudes is used to characterize the contamination. More recently, Akkurt, *et al.* (2004) have extended the analysis by developing time and T_2 domain approaches to assess contamination from the pumpout phase in the application of the downhole fluid sampler.

In the present work, new approaches to study contamination are developed based on the following fluids. NovaPlus, a commonly used base oil in drilling, is the contaminant. NovaPlus (3 cp) is a mixture of 16- to 18-carbon internal olefins. Nova Plus will be abbreviated as SNP. The crude oils used are from the North Sea (13.7 cp), from offshore China (207 cp), and from the Gulf of Mexico (18.7 cp). Henceforth, the crude oils will be called STNS, PBB, and SMY, respectively. The above information is summarized in Table 1.

The objective in this study is to relate the degree of contamination to features in the T_2 distributions. Another goal is estimating the extent of contamination from measured T_2 distributions of samples at unknown degrees of contamination. The traditional approach in studying fluids in NMR logs is using a logarithmic-mean T_2 (log-mean T_2 , $T_{2,LM}$). The new approaches are compared with using $T_{2,LM}$ to estimate contamination.

Table 1: Viscosities and Abbreviations for Fluids Investigated

Fluid	Type	Abbreviation	Viscosity (cp)
Nova Plus	Base oil	SNP	3.3
North Sea	Crude oil	STNS	13.7
Offshore China	Crude oil	PBB	206.7
Gulf of Mexico	Crude oil	SMY	18.7

Two new approaches will be described and implemented herein. In one approach, contamination is characterized by amplitudes at a limited range of relaxation times in each T_2 distribution. In contrast, the default approach using $T_{2,LM}$ agglomerates data at all T_2 into a weighted average. Thus, using a limited range of relaxation times from the T_2 distribution would increase NMR sensitivity to contamination. This would salvage information from useful regions of the T_2 distribution, without needing to consider the entire distribution as in $T_{2,LM}$. The second approach uses a hypothesized probability distribution to fit the experimental T_2 distribution. Data in the T_2 domain are fit to a skewed Gaussian distribution, whose parameters can be related to contamination. With either of the two approaches, a polynomial fit extends the characterization over the entire contamination range. The polynomial can then be used to estimate the degree of contamination.

Experimental

The experimental samples are as follows. Crude oil mixtures with the model contaminant, NovaPlus, were prepared at various volumetric concentrations. The concentrations used for STNS and PBB mixtures are 10, 20, 50 and 75% SNP. The crude oil (0% SNP) and SNP (100% SNP) were also included in the measurements. For mixtures of SMY and SNP, concentrations prepared were 0, 10, 20, 50, 80, 90, and 100% SNP. For 20% and 50% SNP, two samples were prepared to assess reproducibility.

The following measurements were performed. For all but the second samples of SMY mixtures at 20% and 50% SNP, the T_2 relaxation time and the viscosity are measured. For the two samples mentioned, the T_2 relaxation time was measured but the sample volume was too low to do the viscosity measurement.

Deoxygenation, the removal of the paramagnetic contaminant oxygen, was not performed before any of the T_2 measurements for two reasons. First,

invading base oil in a drilled formation would contain oxygen (Chen *et al.* 2004). Furthermore, the amount of dissolved oxygen is expected to play only a small role because the relaxation time distributions for the base and crude oils in this study fall below 1 second, for which the effect of oxygen on T_2 distributions is minimal (Lo 1999).

T_2 measurements are made by two 2 MHz MARAN instruments, labeled MARAN-SS and MARAN-M, manufactured by Resonance Instruments. In this measurement, the decay in signal amplitude, or magnetization, is measured as a function of time. The resultant data is said to be in the time domain.

The decay process is characterized by the following equation:

$$M(t) = \sum_j M_{0j} e^{-\frac{t}{T_{2j}}}. \quad (1)$$

In this expression, M is the total magnetization at time t , M_{0j} is the initial magnetization of component j , and T_{2j} is the T_2 value corresponding to component j .

The acquired data is then processed, converting the time-domain data to the T_2 -domain. Before this, the large number of time-domain data points is parsed. This process, called “sampling and averaging”, reduces the computational load in the conversion with minimal sacrifice to data quality (Chuah 1996). The resultant amplitudes in the T_2 domain are placed at predetermined relaxation times, which are spaced apart equally in logarithmic scale. These chosen individual T_2 values, $T_{2,i}$, at which amplitudes are placed, are called bins. An amplitude corresponding to these bins are given the symbol, A_i . The index j is used for the time domain and index i is used for the T_2 domain to signify that bins chosen do not match the intrinsic T_2 values for the mixture components in general.

The number of runs performed for each set of mixtures differs depending on the crude oil. For mixtures containing STNS or PBB, one T_2 distribution measurement is done. For the SMY mixtures, four separate T_2 -distribution measurements of the same set of samples are made, for the statistical analysis below. The separate measurements will be called Run 1, Run 2, Run 3, and Run 4.

NMR data were obtained using the following conditions. Runs 1, 2, and 3 were performed with MARAN-SS and Run 4 was performed with MARAN-M. In experiments for the mixtures mentioned above, the acquisition conditions used are 128 scans, 9216 (9k) echoes (time-domain data points), 320 μ s echo spacing (time between echoes in each scan), and a 5 s wait time between neighboring scans. The only exception to this is that for Run 3 and Run 4, the number of

scans was not 128, but was adjusted such that the signal-to-noise ratio is 100. Data acquisition software automatically determines the actual number of scans.

The viscosities are measured using a Brookfield viscometer, Model LVDV-III+. Measurements are made near the maximum shear rate that does not exceed torque limits or the rotation speed of the instrument. For the STNS and PBB mixtures, the viscosity for each set was measured after the T_2 distribution was obtained. For the SMY samples, only samples having enough volume had their viscosity measured. This measurement was done after Run 1. The temperature of both T_2 relaxation time measurements and viscosity measurements is 30 °C.

Overview of Approach

The results will be divided into three approaches. The first approach is traditional, characterizing mixture viscosity and log-mean T_2 . The second approach applies a selective contamination index (SCI) for relating measured T_2 distributions to contamination. The third approach shows how a skewed Gaussian model for the relaxation time distributions performs in estimating contamination.

Before proceeding, a brief explanation as to the difference in the methods used for the $T_{2,LM}$ approach, the SCI approach, and the distribution parameter approach is warranted. Using $T_{2,LM}$ involves a one-stage analysis. All the data contributes to $T_{2,LM}$. The value of $T_{2,LM}$ equally involves all bins, depending only on the signal amplitudes in all the bins. The methods in the SCI approach and distribution parameter approach involve two stages.

The two stages in the SCI approach and the distribution parameter approach are described below. In the first stage of the SCI approach, a subset of the available T_2 bins is used to define intermediate quantities, called binwise contamination indices. The second stage creates a quantity, the selective contamination index or SCI, from a function of these intermediate quantities. For the distribution parameter approach all the data is used, similar to using $T_{2,LM}$. However, the approach is still in two stages. In the first stage, one obtains the parameters of the skewed Gaussian model used to fit the data. The second stage defines a single figure, the distribution parameter index (DPI), which is a function of a subset of these parameters.

Preliminary Measurements

Fig. 1 shows the incremental T_2 distributions (as opposed to cumulative distributions) for mixtures of STNS and SNP. The plots represent data from 50 T_2 bins. The top panel shows the distribution for the contaminant SNP, and

subsequent panels contain increasing amounts of STNS. For a light crude oil

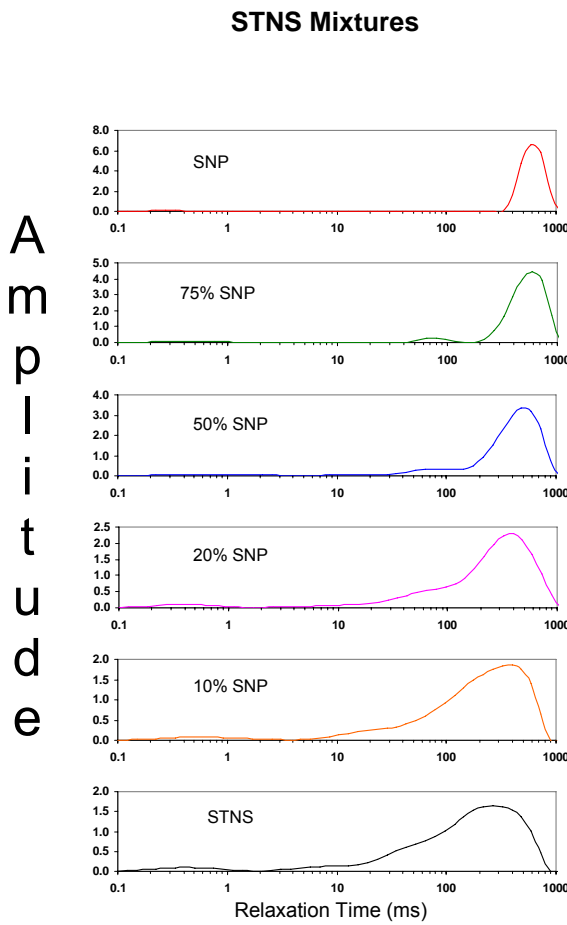


Figure 1: Stacked plots showing incremental T_2 relaxation time distributions for mixtures of STNS crude oil and SNP base oil. Note that the amplitude axis is not to scale for all curves in the stack.

not differ greatly from the base oil, SNP. As SNP contamination decreases, the most noticeable change is that the T_2 distribution becomes more skewed toward shorter relaxation times. However, much of the amplitude for all contamination levels is localized at relatively high relaxation times.

The situation is different for PBB mixtures, Fig. 2. Fig. 2 shows T_2 distributions for mixtures in the same format as for Fig. 1. In these mixtures, all measured contamination levels can be differentiated. Both the mode and the tail of the distribution shift noticeably as the contamination level changes. These features are seen even at a contamination of 10% SNP.

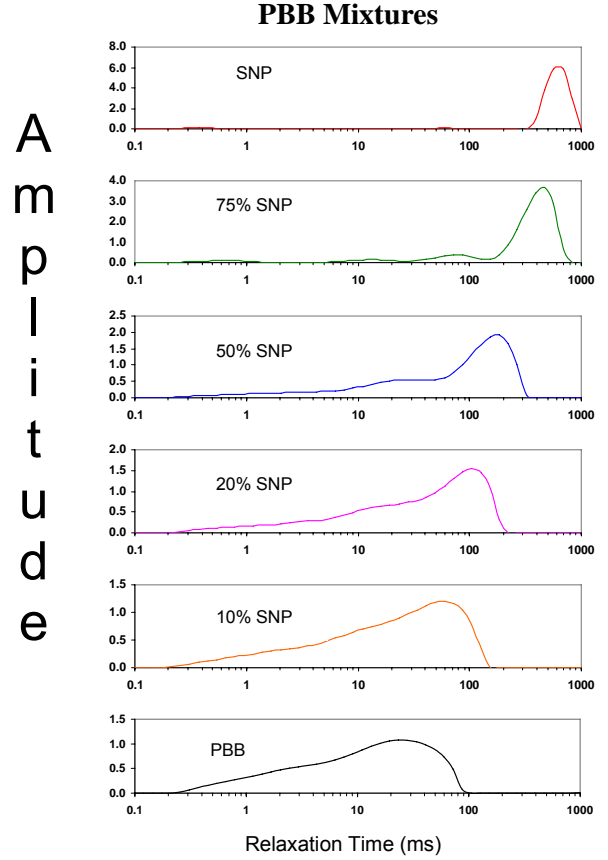


Figure 2: Stacked plots showing incremental T_2 relaxation time distributions for mixtures of PBB crude oil and SNP base oil. Note that the amplitude axis is not to scale for all curves in the stack.

like STNS, the mode, or T_2 value corresponding to the highest amplitude in the distribution, does

Fig. 3 shows the same diagram for six of the samples from Run 1 with SMY mixtures. The mode and tail of the T_2 distributions vary less than PBB mixtures and more than STNS mixtures. This is expected given that the viscosity of SMY lies between the other two crude oils. The trends for SMY are reproducible in the other runs. The reproducibility is demonstrated at a base oil volume fraction of 0.5 in Fig. 4.

The T_2 distributions in Figs. 1-3 can be assessed in terms of the logarithmic mean relaxation times ($T_{2,LM}$), which appear in Table 2 and Table 3. Table 2 shows the log-mean relaxation times for mixtures containing STNS or PBB crude oils with SNP. One trend from Table 2 is that $T_{2,LM}$ increases as more base oil is added. A second trend is that this increase in $T_{2,LM}$ is more severe for PBB, the heavier crude oil. $T_{2,LM}$ values for Run 1 through Run 4, on mixtures containing the crude oil SMY, are shown in Table 3. As with STNS and PBB mixtures, $T_{2,LM}$ increases with increasing concentrations of base oil.

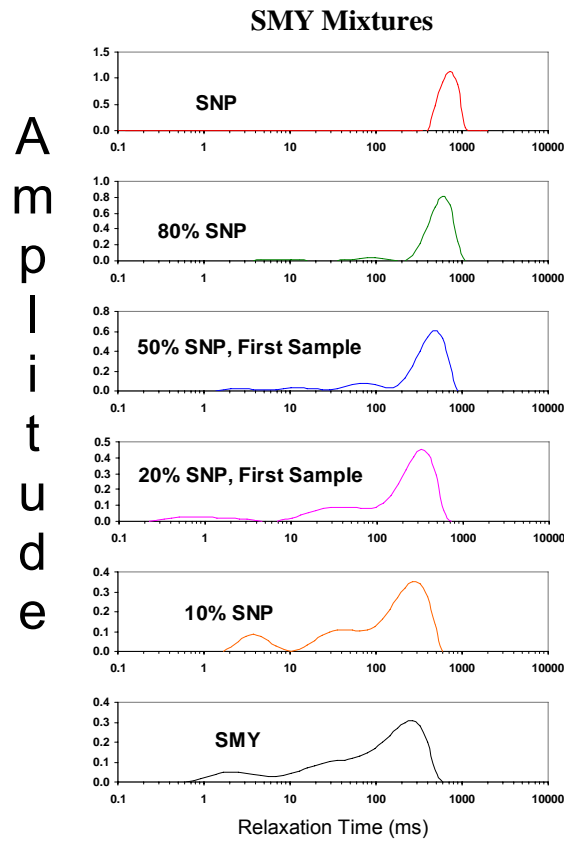


Figure 3: Stacked plots showing incremental T_2 relaxation time distributions for mixtures of SMY crude oil (Run 1) and SNP base oil. Note that the amplitude axis is not to scale for all curves in the stack.

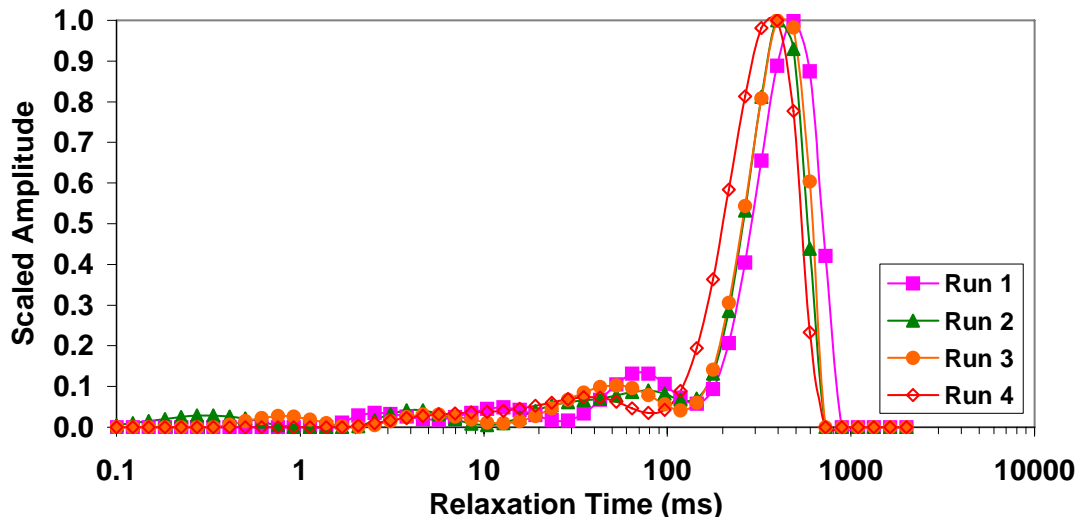


Figure 4: Incremental T_2 distributions for repeated measurements of the first sample containing 50% SMY crude oil and 50% SNP base oil.

Viscosities appear in Table 4 and Table 5. Table 4 shows the measured viscosities for the same mixtures in Table 2, namely for mixtures containing STNS or PBB crude oils. As with $T_{2,LM}$, the viscosity changes more drastically for heavier crude oils. However, viscosity decreases as more base oil, SNP, is present in the mixture. A similar table for viscosity of SMY mixtures is shown in Table 5. Note that some samples have insufficient volume for the measurement of viscosity.

Table 2: Log-mean T_2 Values for Mixtures of STNS and PBB crude oils with SNP base oil

SNP Content (Volume Fraction)	$T_{2,LM}$ (ms)	
	STNS	PBB
0.00	114.7	9.9
0.10	145.3	16.4
0.20	171.7	27.8
0.50	288.3	52.6
0.75	403.2	233.5
1.00	534.6	512.4

Table 3: Log-mean T_2 Values for Mixtures of SMY crude oil with SNP base oil

SNP Content (Volume Fraction)	$T_{2,LM}$ (ms)			
	Run 1	Run 2	Run 3	Run 4
0.00	72	70	70	54
0.10	94	93	88	56
0.20 (1 st)	112	110	117	95
0.20 (2 nd)	157	109	139	106
0.50 (1 st)	251	180	214	214
0.50 (2 nd)	343	262	255	248
0.80	448	N/A	N/A	425
0.90	586	586	641	622
1.00	660	587	728	685

Fig. 5 shows a cross-plot between $T_{2,LM}$ and viscosity for the three sets of mixtures. For the SMY mixtures, $T_{2,LM}$ comes from Run 1, because the viscosity measurement corresponds to Run 1. The line is the expected behavior based on an existing correlation between $T_{2,LM}$ and viscosity, η , for dead crude oils. The correlation is given by

$$T_{2,LM} = \frac{1200}{\eta^{0.9}}, \quad (2)$$

and is called the Morriss Correlation (Morriss, *et al.* 1997). As Fig. 5 shows, the mixtures appear to follow this expected behavior.

Table 4: Viscosities for Mixtures of STNS and PBB crude oils with SNP base oil

SNP Content (Volume Fraction)	Viscosity (cp)	
	STNS	PBB
0.00	13.7	206.7
0.10	11.1	103.0
0.20	9.2	57.0
0.50	5.8	26.8
0.75	4.3	6.3
1.00	3.3	3.3

Table 5: Viscosities for Mixtures of SMY Crude Oil with SNP Base Oil

SNP Content (Volume Fraction)	Viscosity (cp)
0.00	18.7
0.10	14.8
0.20 (1 st)	11.0
0.20 (2 nd)	No measurement
0.50 (1 st)	6.2
0.50 (2 nd)	No measurement
0.80	4.0
0.90	3.4
1.00	3.1

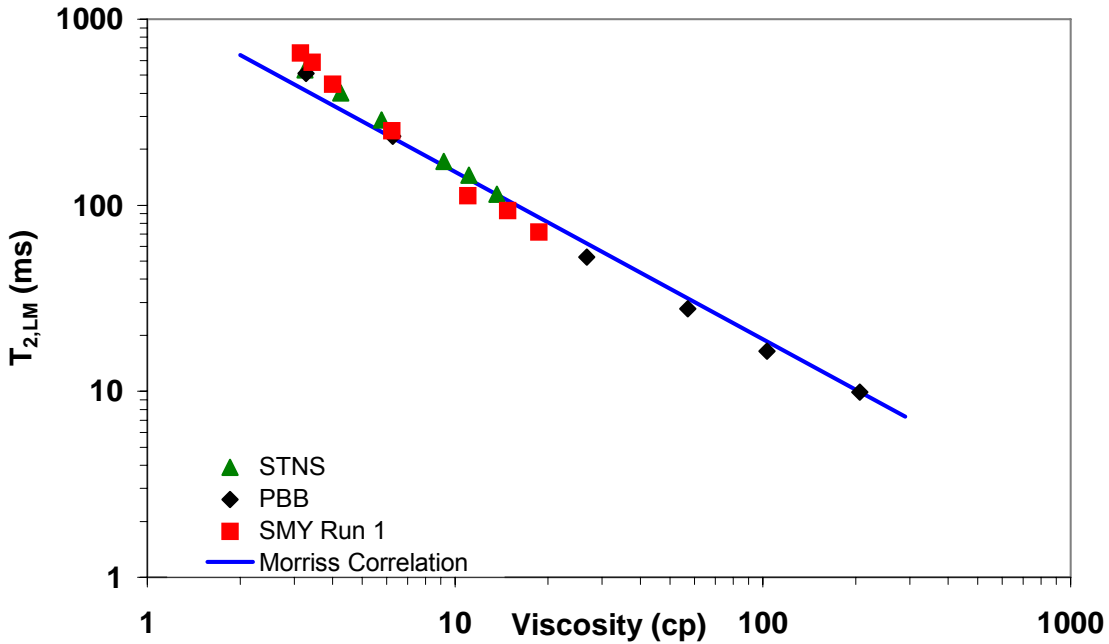


Figure 5: Relationship between viscosity and $T_{2,LM}$: Comparison to Moriss Correlation.

Fig. 5 showed how $T_{2,LM}$ and η are related for each of the measured samples. To observe trends in either of these quantities, one can represent the measured data in terms of their variation with contamination level. This is shown in Figs. 6 and 7.

Fig. 6 compares measured and interpolated $T_{2,LM}$ for the mixtures of each crude oil with SNP. The experimental values of $T_{2,LM}$ are compared with a linear interpolation between the measured log-mean T_2 values for the crude oil and for SNP. The interpolations are based on the $T_{2,LM}$ values for SNP and the crude oil in question according to the following equation:

$$T_{2,LM}^{mix} = (T_{2,LM}^{crude})^{1-f} (T_{2,LM}^{SNP})^f. \quad (3)$$

In Eq. 3, $T_{2,LM}^{mix}$ is the interpolated log-mean relaxation time of the mixture, and $T_{2,LM}^{crude}$ and $T_{2,LM}^{SNP}$ are the experimental log-mean relaxation times for the crude oil and for SNP, respectively. The quantity f is the volume fraction of SNP. In Fig. 6, experimental data are shown as points and interpolated data are represented as lines. Only one run is shown for mixtures of SMY for illustrative purposes. Other runs show similar behavior. Fig. 6 shows that the characterization of $T_{2,LM}$ as a weighted log-mean of the $T_{2,LM}$ values of the two components provides a fair description of the trend seen in the experimental data.

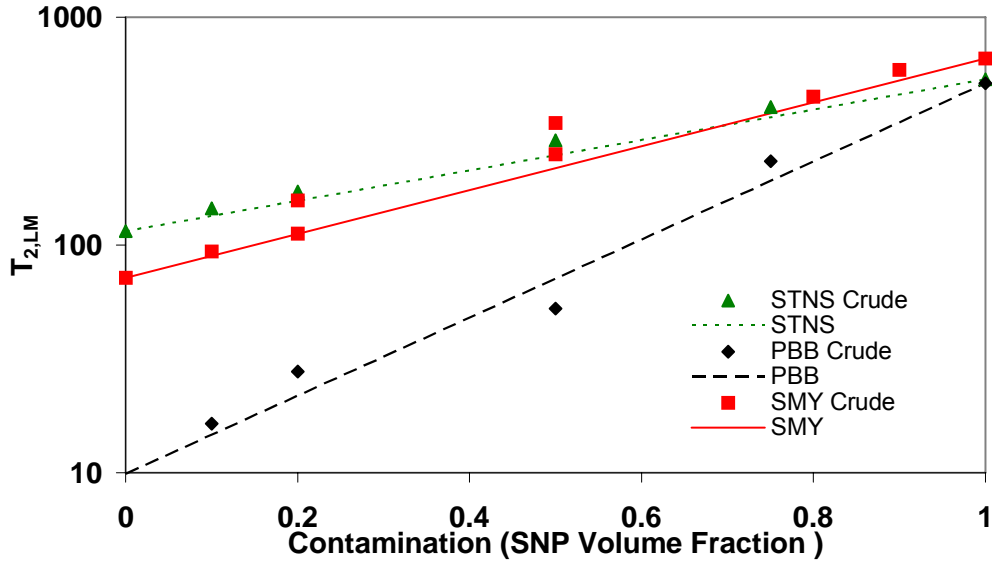


Figure 6: Comparison of experimental $T_{2,LM}$ values with interpolations for mixtures of crude oil and SNP based on Equation 3.

Fig. 7 repeats the comparison for viscosities. The equation for the interpolation of mixture viscosities is analogous to that for $T_{2,LM}$:

$$\eta^{\text{mix}} = (\eta^{\text{crude}})^{1-f} (\eta^{\text{SNP}})^f \quad (4)$$

In this expression, η^{mix} is the interpolated viscosity of the mixture, η^{crude} is the experimental crude oil viscosity, and η^{SNP} is experimental SNP viscosity. Again, f is the SNP volume fraction. As with Fig. 6, the interpolated equation (lines in Fig. 7) describes the trend of the experimental data (points in Fig. 7).

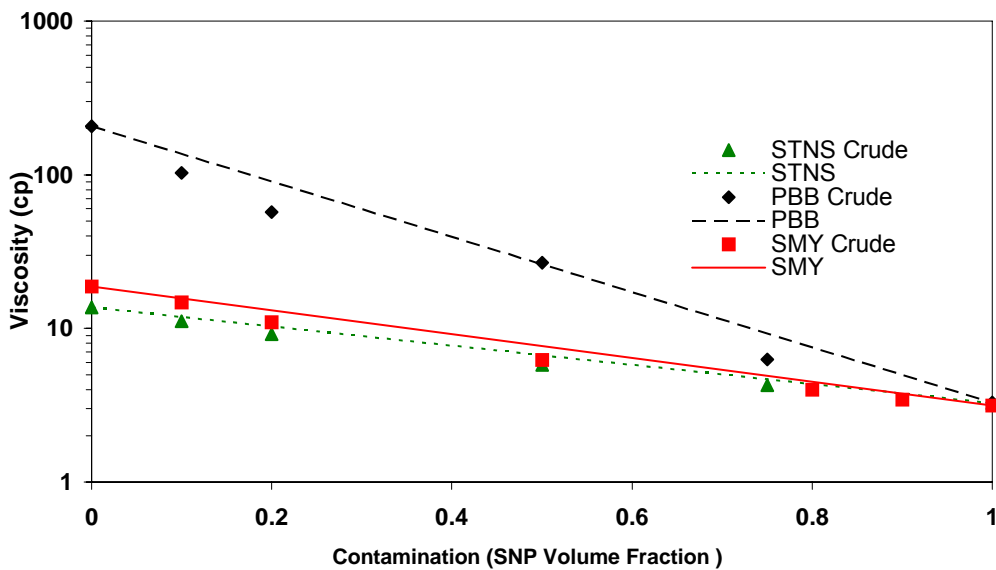


Figure 7: Comparison of experimental viscosities with interpolations for mixtures of crude oils and SNP based on Equation 4.

Selective Contamination Index Approach

Although Figs. 6 and 7 suggest a trend from concentration-weighted logarithmic-mean averages for mixtures of SNP and crude oils, deviations of up to 60% are observed. In order to improve the characterization of contamination from T_2 distributions, an attempt is made to utilize a more appropriate summary of NMR T_2 behavior than the log-mean value, $T_{2,LM}$. Using signal amplitudes at specifically chosen T_2 bins allows a portion of the collected data to serve in mixture analysis, without being lumped in an overall average like the logarithmic mean.

To do this, it is convenient to use cumulative distributions. The amplitude of a cumulative distribution at a specific bin is a running sum of amplitudes from the earlier incremental T_2 distributions, belonging to that bin and to all bins at lower values of T_2 . Thus, cumulative distributions continually increase from low to high relaxation times. Cumulative distributions are preferred because they exhibit a more monotonic behavior when the same T_2 bin is compared for different contamination levels. The cumulative distributions here are in the T_2 domain, just like incremental distributions, and are normalized such that the final amplitude (after amplitudes from all relaxation times have been summed) for each sample is equal to 1.

For illustration, Fig. 8 shows the cumulative distribution for PBB mixtures with the base oil SNP. The information in Fig. 8 is the same as in Fig. 2, presented in a different form. Fig. 8 demonstrates the monotonic increase in amplitude at a given T_2 as the base oil content decreases. Note that the T_2 bins are shown explicitly as points in Fig. 8.

In Fig. 9, cumulative amplitudes from 11 of the 50 bins used to obtain T_2 distributions are shown for Run 1 SMY mixtures. The data in each bin, plotted as separate entities in Fig. 9, includes information from T_2 distributions at all measured contamination levels. Note that bins placed in the upper part of the legend are the bins with the highest cumulative amplitudes in the plot. The lines shown result from linear regression. Those bins having regression lines of the greatest slope are most responsive to contamination and thus would be more useful in characterizing the relative amounts of SNP and crude oil.

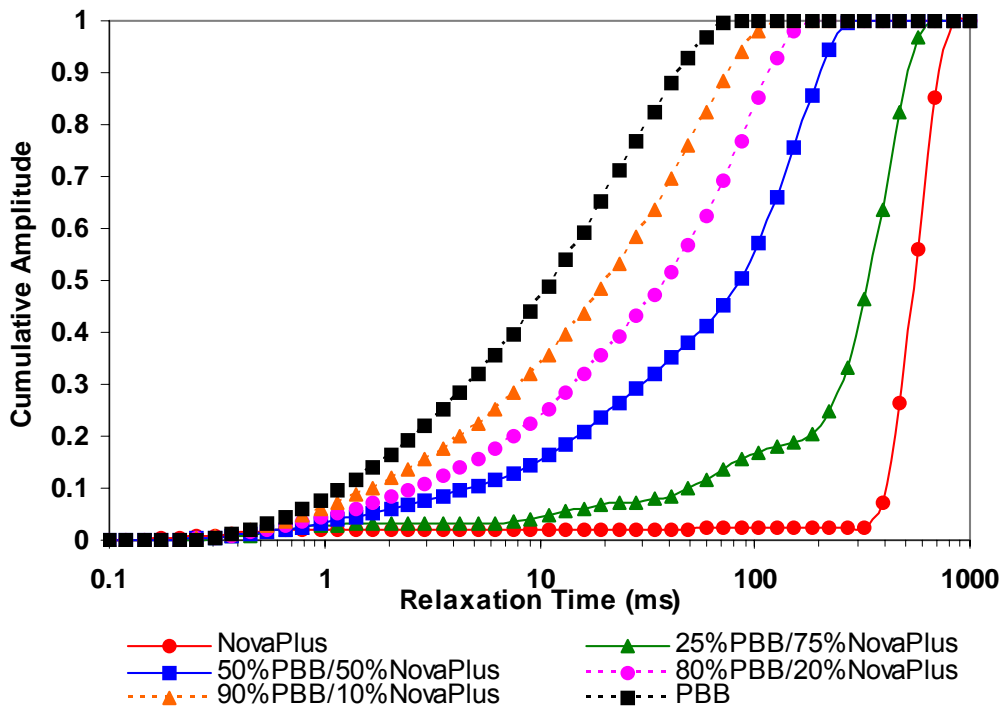


Figure 8: Normalized, cumulative T_2 distributions for mixtures of PBB crude oil and SNP base oil.

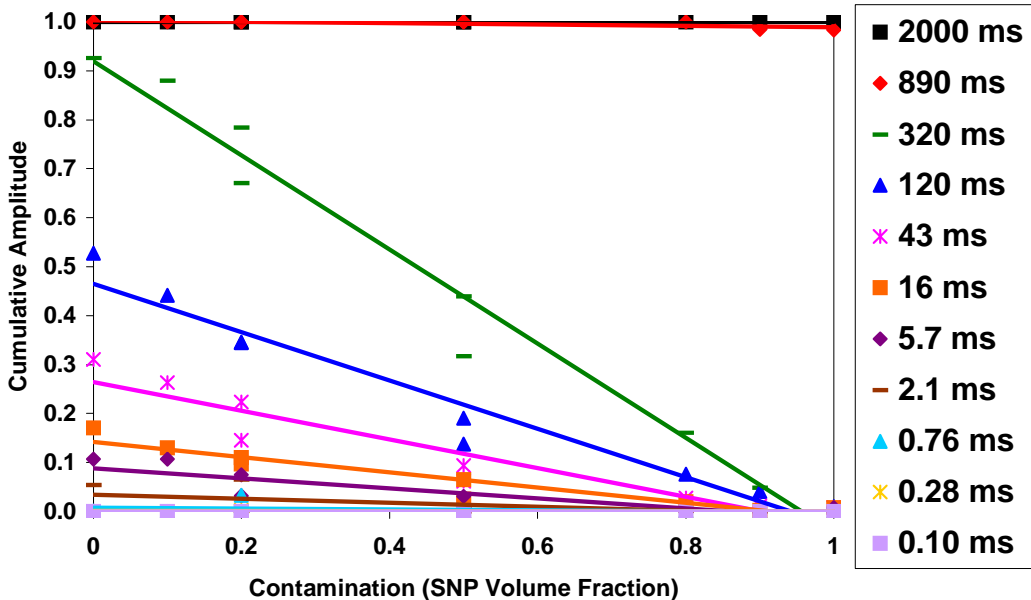


Figure 9: Behavior of signal amplitude in selected T_2 bins as a function of SNP concentration in Run 1 of mixtures of SMY crude oil and SNP base oil.

Fig. 10 is a direct representation of slopes in plots such as Fig. 9, for STNS mixtures. Fig. 10 includes all 50 bins (shown as points), whereas Fig. 9 showed only 11 bins. Note that the plotted slope is large, as desired, only for a limited range of relaxation times. Also, more bins appear on the left side of the maximum slope, corresponding to the peak in Fig. 10, than on the right. In fact, the SCI approach uses only those bins on the left side of the maximum slope whose slopes are between 20% and 80% of the maximum slope in figures such as Fig. 10. This choice of bins to use in determining SCI results from considering both sensitivity to contamination, as indicated by the aforementioned slopes, and the consistency of the binwise contamination index, defined below, for the selected bins.

The binwise contamination indices are determined for the selected bins as follows:

$$I_{f,i} = \frac{G_i^{\text{sample}} - G_i^{\text{crude}}}{G_i^{\text{SNP}} - G_i^{\text{crude}}} \quad (5)$$

In this equation, $I_{f,i}$ is the binwise contamination index (not yet the SCI) for SNP volume fraction f and bin i . $G_{f,i}^{\text{sample}}$ refers to the cumulative amplitude for sample with SNP concentration f for bin i and G_i^{SNP} and G_i^{crude} are the cumulative amplitudes in bin i of SNP and of the appropriate crude oil, respectively. The binwise contamination index is defined such that it runs from 0 (for crude oils) to 1 (for SNP). The goal of such a characterization is to calculate a quantity that correlates with the contamination in terms of the SNP volume fraction f .

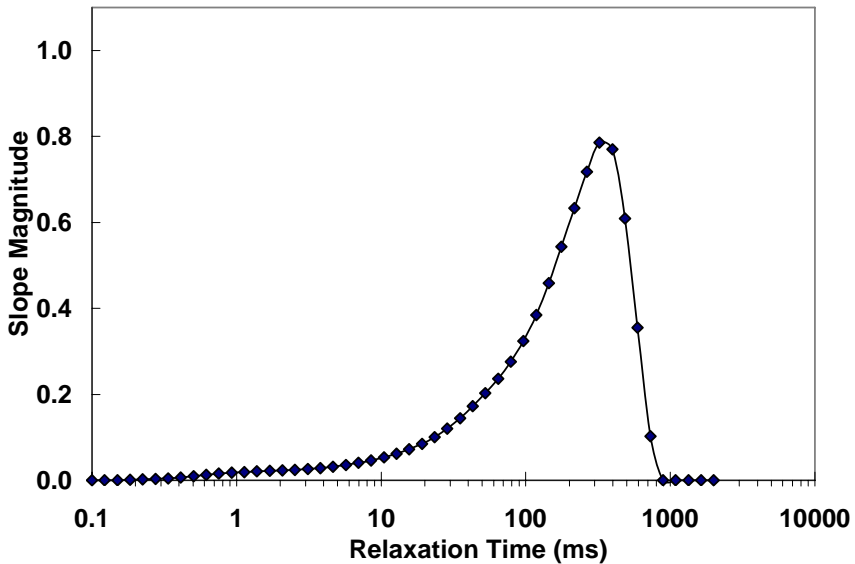


Figure 10: Linear regression parameters of T_2 cumulative amplitude against contamination for all bins in mixtures of STNS crude oil and SNP base oil.

The SCI is determined by taking the arithmetic means of binwise contamination indices for the pre-selected bins. So, SCI can be expressed as

$$SCI = I_f = \sum_{selected\ bins} I_{f,i} . \quad (6)$$

Table 6 shows the SCI values for each concentration of SMY and PBB mixtures. Table 7 shows the SCI values for the SMY measurements. In Table 7, the SCI shown is a mean SCI for each concentration across the four runs. For 80% SNP, only the SCI values from Run 1 and Run 4 are used because instrumental errors caused erroneous results in the other runs. Note that all error values shown are standard deviations. Standard deviations for SNP and for the crude oil are zero because of the definition of the binwise contamination index and SCI.

Table 6: Selective Contamination Indices for Mixtures of STNS and PBB Crude Oils with SNP Base Oil

SNP Content (Volume Fraction)	SCI	
	STNS	PBB
0.00	0.00 ± 0.00	0.00 ± 0.00
0.10	0.20 ± 0.05	0.28 ± 0.03
0.20	0.36 ± 0.02	0.50 ± 0.04
0.50	0.70 ± 0.02	0.68 ± 0.04
0.75	0.88 ± 0.03	0.94 ± 0.02
1.00	1.00 ± 0.00	1.00 ± 0.00

Table 7: Selective Contamination Indices for Mixtures of SMY Crude Oil with SNP Base Oil

SNP Content (Volume Fraction)	SCI
0.0	0.00 ± 0.00
0.1	0.16 ± 0.03
0.2 (1 st)	0.33 ± 0.02
0.2 (2 nd)	0.42 ± 0.04
0.5 (1 st)	0.67 ± 0.04
0.5 (2 nd)	0.76 ± 0.03
0.8	0.90 ± 0.02
0.9	0.96 ± 0.01
1.0	1.00 ± 0.00

Figs. 11-13 show the SCI values in Table 6 and Table 7. The curves shown on the figures represent cubic polynomial interpolations of the data points. Fig. 11 is the cubic polynomial interpolation for mixtures containing STNS crude oil. Fig. 12 shows this data for PBB crude oil mixtures. Fig. 13 shows SCI data for SMY mixtures in Runs 1-4. In Fig. 13, the data correspond to the mean SCI values shown in Table 7 and the bars are the corresponding standard deviations. For each set of mixtures, Figs. 11-13 provide a relationship between SCI and contamination level.

From this relationship, the degree of contamination is estimated as follows. T_2 distributions of an unknown mixture of a particular system (for example, SMY and SNP) are measured. Then, binwise contamination indices are calculated for bins previously identified as optimal. This requires the distributions of the crude oil and base oil separately, which are available because they go into developing the interpolation. The average of the values calculated gives an SCI. This value can be used with the polynomial interpolation, which is of the following form:

$$I_f = P(f). \quad (7)$$

I_f is the SCI for a particular SNP volume fraction, f . This is the quantity that would be calculated from the measurement. P is the functional form of the polynomial in f . The equation can then be placed in the following form:

$$P(f) - I_f = 0 \quad (8)$$

The only physical root of this equation, namely when f is between 0 and 1, yields the SNP volume fraction or contamination level, f .

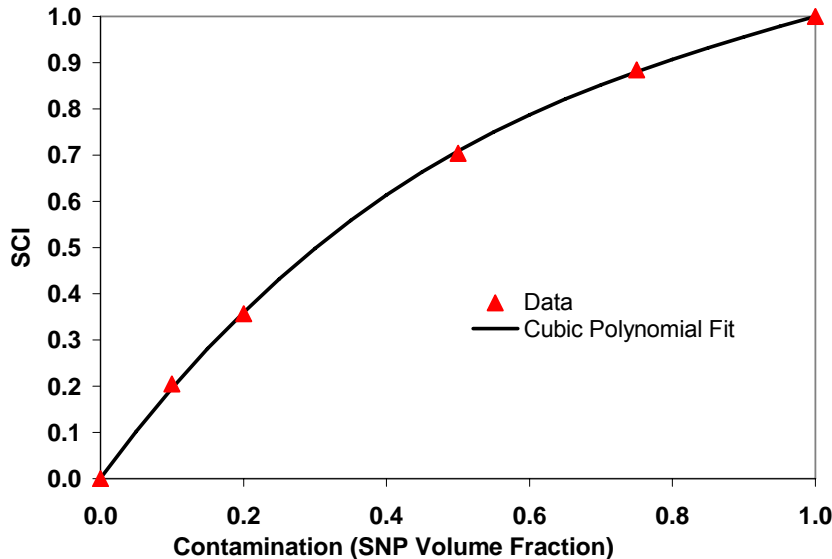


Figure 11: Selective contamination index and polynomial interpolation for mixtures of STNS crude oil and SNP base oil.

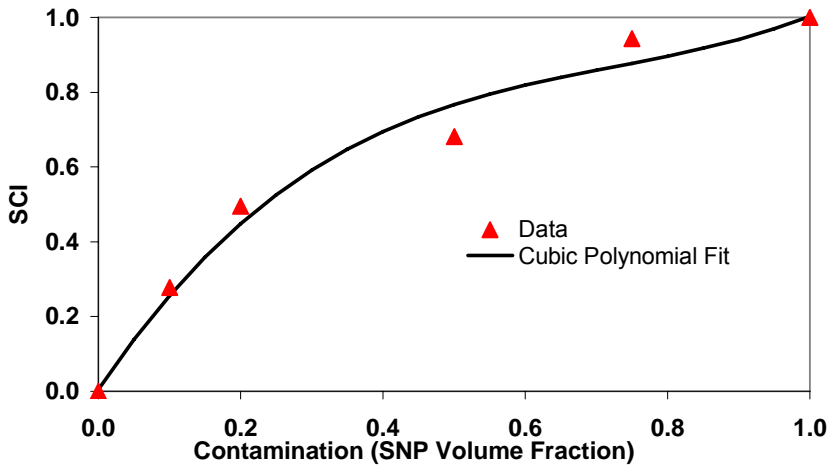


Figure 12: Selective contamination index and polynomial interpolation for mixtures of PBB crude oil and SNP base oil.

The result of this procedure can be compared statistically with contamination levels estimated from $T_{2,LM}$ for SMY. Such a comparison for SMY is shown in Fig. 14. Fig. 14 shows both SCI (plot on the left) and $T_{2,LM}$ (on right) as a function of contamination. The points represent the data from Runs 1-4. The central line in both cases is a cubic polynomial interpolation. For the SCI, the construction of the cubic polynomial was mentioned above. For $T_{2,LM}$, the cubic polynomial is constructed between the logarithm (base 10) of $T_{2,LM}$ and contamination. The two curves flanking the central line on each plot are 95% confidence intervals for the respective polynomial interpolation.

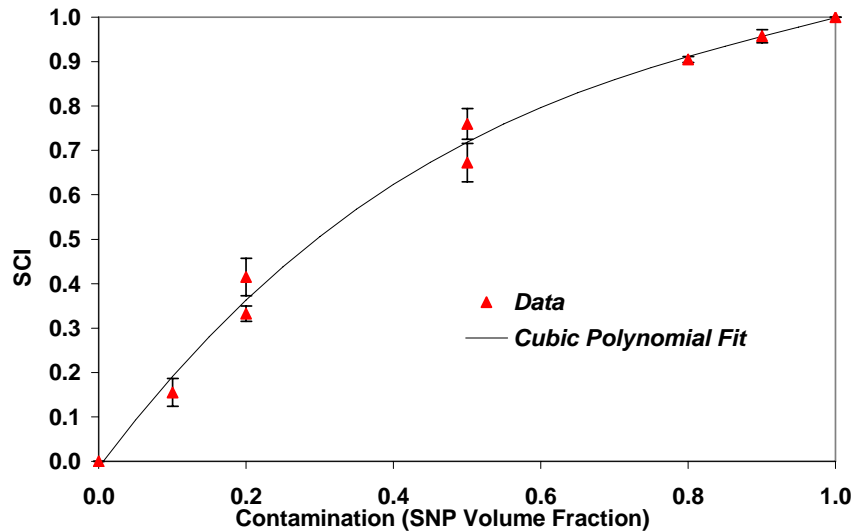


Figure 13: Selective contamination index and polynomial interpolation for repeated measurements of mixtures containing SMY crude oil and SNP base oil.

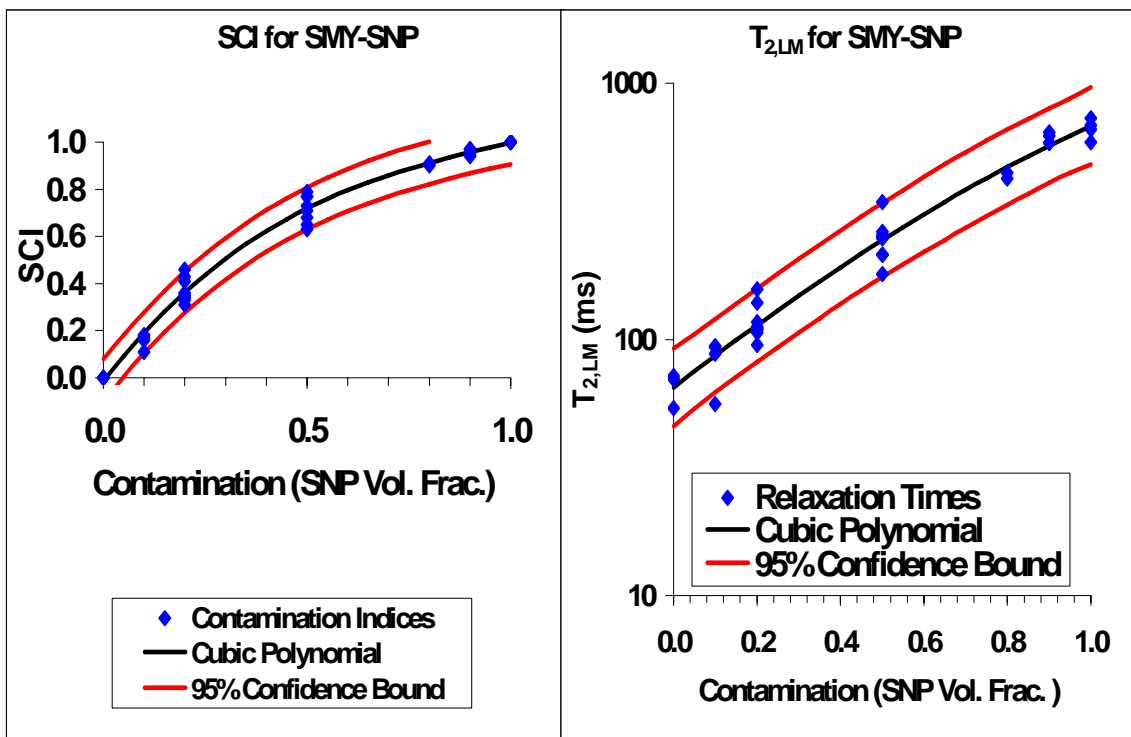


Figure 14: Selective contamination index and $T_{2,LM}$, each with polynomial interpolation and confidence intervals for repeated measurements of mixtures containing SMY crude oil and SNP base oil.

The width of these confidence intervals shows the uncertainty in contamination level given a particular parameter, whether $T_{2,LM}$ or SCI. Notice that the width of the interval is smaller for the SCI measurements than for $T_{2,LM}$ over a large concentration range. In particular at contaminations near 20% SNP, the width of the confidence interval is 0.23 for $T_{2,LM}$ and 0.11 for the SCI, both in units of SNP volume fraction. This shows that a particular measured $T_{2,LM}$ for a sample with contamination near a SNP volume fraction of 0.20 would yield twice the uncertainty in contamination level as the corresponding SCI. This suggests that the SCI is better than interpolation of $T_{2,LM}$.

Distribution Parameter Approach

A more intuitive way of addressing NMR contamination data is by using a statistical distribution. In the distribution parameter approach discussed here, a skewed Gaussian distribution models T_2 -domain data. The basis for choosing a skewed Gaussian distribution is as follows. When T_2 domain amplitudes are charted against a logarithmically scaled T_2 axis, a pure component typically shows a Gaussian distribution. Crude oils typically have T_2 distributions that are skewed toward short relaxation times. The skewed Gaussian model allows for

this difference in two sides of the mode and maintains the Gaussian character for single components.

Equation 9 shows the equation for the model itself:

$$A(T_{2,i}^*) = \begin{cases} C_4 \exp\left[-\frac{(T_{2,i}^* - C_1)^2}{2C_2^2}\right]; T_{2,i}^* \leq C_1 \\ C_4 \exp\left[-\frac{(T_{2,i}^* - C_1)^2}{2C_3^2}\right]; T_{2,i}^* \geq C_1 \end{cases} \quad (9)$$

In this equation, $A(T_{2,i}^*)$ is the amplitude of the fitted model at a given T_2 bin, $T_{2,i}^*$. The superscript on $T_{2,i}^*$ indicates that it is the logarithm of $T_{2,i}$ that is fit with a Gaussian distribution, not $T_{2,i}$ itself. C_1 is the logarithmic mode of the skewed Gaussian model and C_4 is the pre-exponential factor. The model is skewed because of C_2 and C_3 , which represent standard deviations on respective sides of the mode of the distribution. C_1 , C_2 , C_3 , and C_4 form the parameters of the model. A non-linear least squares regression was used to achieve the fit between experimental data and the posited model.

The objective function in the fitting procedure is

$$\Phi_{T_2}(C_1, C_2, C_3, C_4) = \sum_i (A(T_{2,i}^*) - A_i)^2. \quad (10)$$

Here, Φ_{T_2} is the objective function for the T_2 domain fit. It depends on the model parameters because these can be changed to achieve the best match between the set of fitted amplitudes $A(T_{2,i}^*)$ and the experimental amplitudes, A_i .

The resulting fits for STNS mixtures are given in Fig. 15. The data points are the experimental data and the line represents the fit. Note that the fit captures the shape of the peak associated with the mode of the distribution. The fits for the tails at shorter relaxation times are still good, but some discrepancies are visible.

Fig. 16 repeats the treatment for mixtures of PBB and SNP. Again, the peaks associated with modes are more accurately fit than the tailing portion of the T_2 distribution. However, the modes are not fit as well as with STNS mixtures. The fits also extend farther toward short relaxation times than with STNS mixtures because of the greater amplitude for PBB mixtures at these relaxation times.

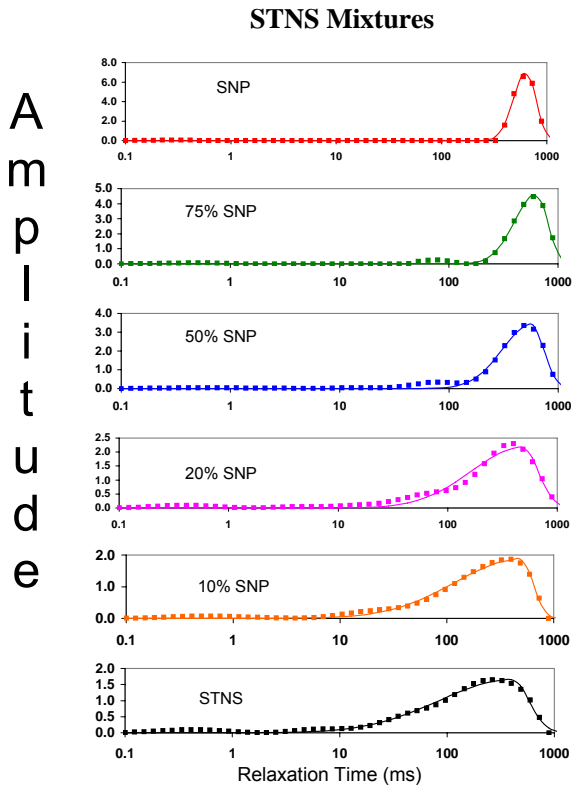


Figure 15: Stacked plots showing T_2 relaxation time distributions and the corresponding fit for mixtures of STNS crude oil and SNP base oil. Note that the amplitude axis is not to scale for all curves in the stack.

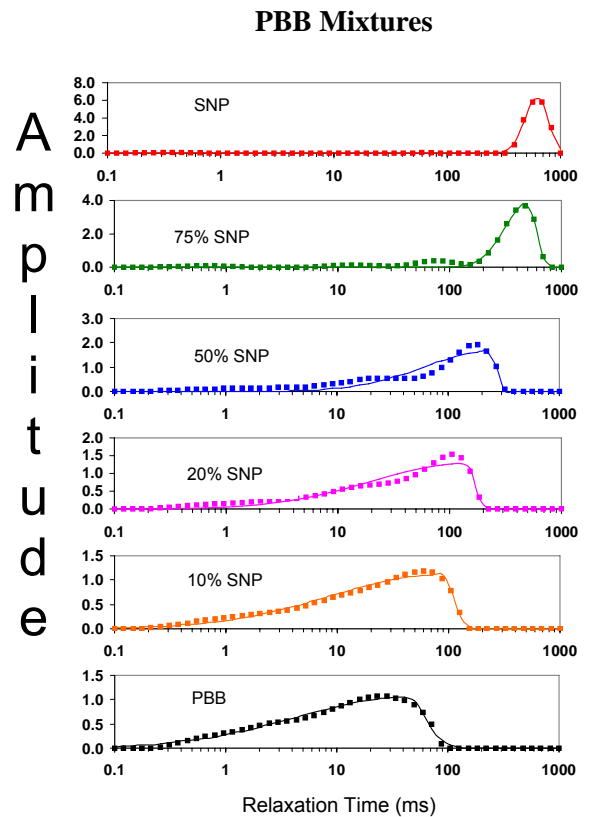


Figure 16: Stacked plots showing T_2 relaxation time distributions and the corresponding fit for mixtures of PBB crude oil and SNP base oil. Note that the amplitude axis is not to scale for all curves in the stack.

Fig. 17 shows fits for six representative samples from Run 1 with SMY mixtures. The nature of the fits for other runs is similar to that for the corresponding concentrations in Run 1. Fig. 17 shows good fits for the peak associated with the mode. As the SNP concentration increases, the mode is fit better but the fit for the tailing portion of the T_2 distribution is poorer. In the fits for all three crude oil mixtures, the skewness of the model is visible in that the two sides of the fitted distribution have noticeably different widths.

As mentioned earlier, the models used to construct the fits have four parameters. The most relevant parameters in terms of their variation with contamination are C_1 and C_2 , the model logarithmic mode relaxation time and the standard deviation at short relaxation times. Specifically, C_1 should increase with contamination, and C_2 should decrease with increasing contamination. The actual variation of the parameters is seen in log-log plots of the two parameters charted against each other, shown in Fig. 18 for PBB mixtures. Fig. 18 shows the expected trend from crude oil (lowest, right-most point) to SNP (highest, leftmost point) for PBB mixtures. Note that the actual plotted quantities are 10^{C_1} and 10^{C_2} , called the model mode and short-time standard deviation factor, respectively. These modifications of the parameters, rather than the parameters themselves, are plotted because the skewed Gaussian model involves a logarithmic representation of T_2 , as mentioned before.

To develop a quantity that is similar in spirit to the SCI, the distribution parameter index (DPI) is defined. This parameter, defined by Equation 11, accounts for both C_1 and C_2 , and is a scaled distance from the crude oil data point in parameter cross-plots like Fig. 18.

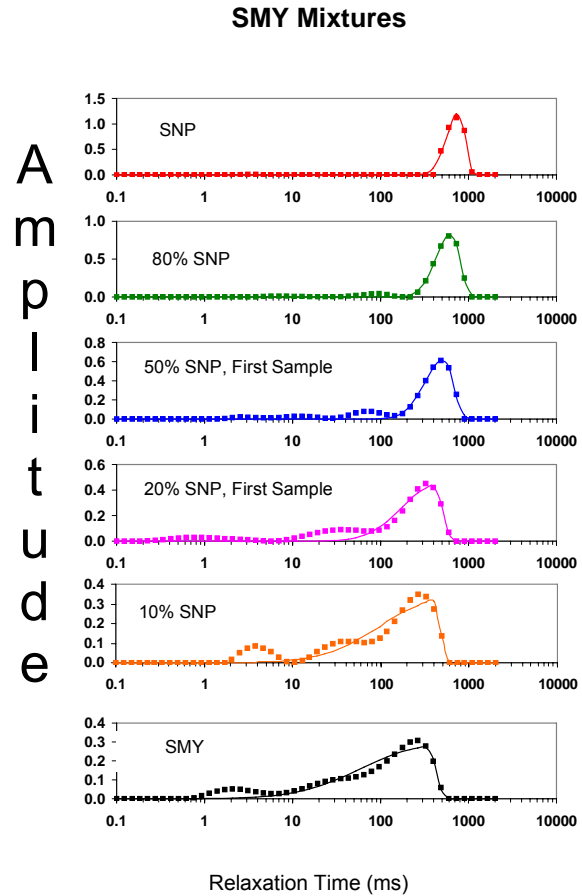


Figure 17: Stacked plots showing T_2 relaxation time distributions and corresponding fits for mixtures of SMY crude oil and SNP base oil (Run 1). The amplitude axis is not to scale for all curves in the stack.

$$DPI = \sqrt{0.5 \left[\left(\frac{C_{1,\text{sample}} - C_{1,\text{crude}}}{C_{1,\text{SNP}} - C_{1,\text{crude}}} \right)^2 + \left(\frac{C_{2,\text{sample}} - C_{2,\text{crude}}}{C_{2,\text{SNP}} - C_{2,\text{crude}}} \right)^2 \right]} \quad (11)$$

In this equation, C_1 and C_2 are the model parameters mentioned earlier. The additional subscripts refer to different T_2 distribution measurements. $C_{1,\text{sample}}$ and $C_{2,\text{sample}}$ refer to the value of C_1 or C_2 for a sample with a particular contamination level, $C_{1,\text{crude}}$ or $C_{2,\text{crude}}$ refer to the parameter value for the T_2 distribution of crude oil in that sample, and $C_{1,\text{SNP}}$ and $C_{2,\text{SNP}}$ refer to the parameters for the T_2 distribution of SNP base oil measured with that mixture set.

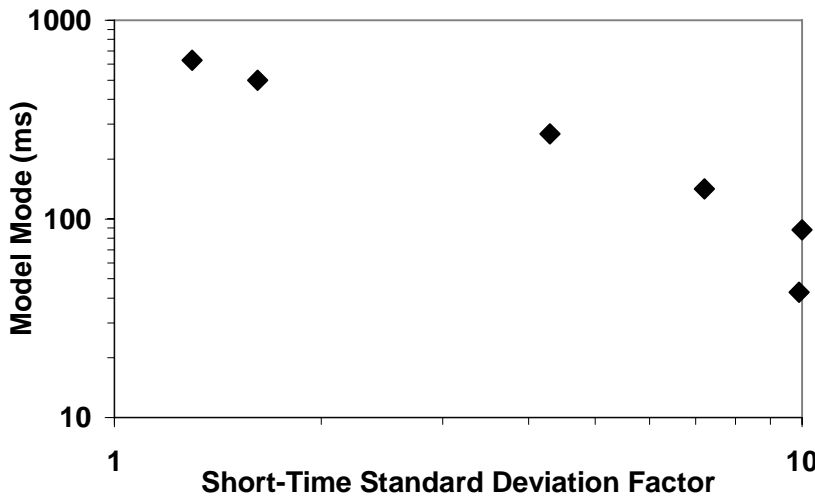


Figure 18: Cross-plot of two parameters of skewed Gaussian model for T_2 domain fits of mixtures of PBB crude oil and SNP base oil.

Figs. 19 and 20 show the respective DPI for mixtures involving STNS and PBB crude oils as a function of the contamination. The DPI is correlated to the contamination with a cubic polynomial (lines in the figures). Figs. 19 and 20 show that the DPI is monotonic with contamination over the entire contamination range. Table 8 shows DPI values for STNS and PBB mixtures.

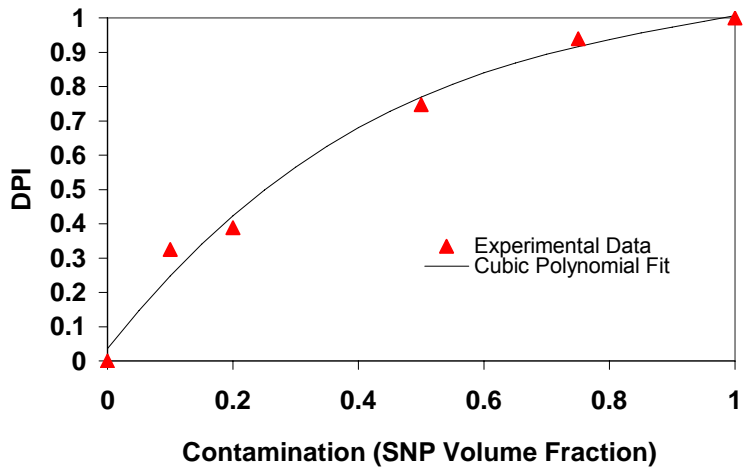


Figure 19: *DPI obtained from model parameters and cubic polynomial fit for T_2 domain fits of mixtures of STNS crude oil and SNP base oil.*

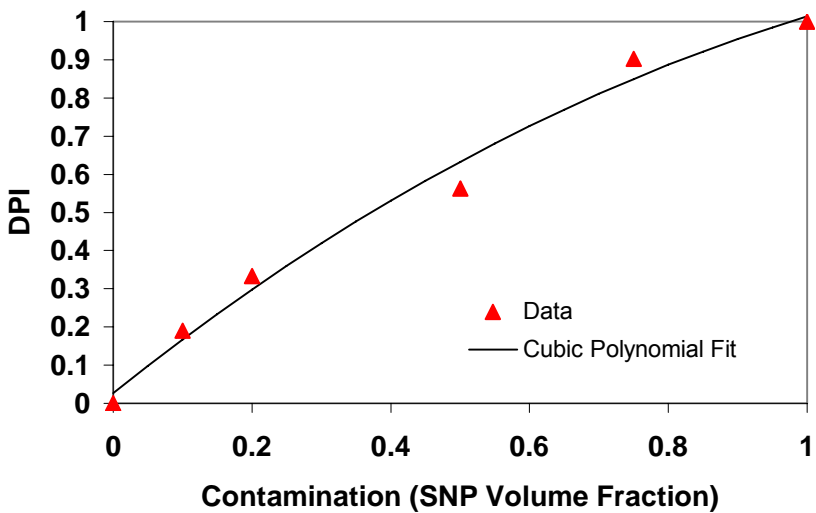


Figure 20: *DPI obtained from model parameters and cubic polynomial fit for T_2 domain fits of mixtures of PBB crude oil and SNP base oil.*

The treatment in Figs. 19 and 20 and in Table 8 can be repeated for SMY mixtures. However for statistical analysis, it is worthwhile to first point out the similarity between the DPI and the SCI. Both are defined such that their value is 0 for a crude oil and 1 for SNP. The DPI, like the SCI, is correlated to contamination with a cubic polynomial. Thus, contamination can be estimated from DPI values from fits of an NMR measurement in the same style as for the SCI. Finding the appropriate roots of the polynomial interpolations developed above for DPI in a manner similar to Equations 7 and 8 for the SCI would provide a contamination level corresponding to an obtained DPI.

Table 8: *DPI Obtained from Model Parameters for T_2 Domain Fits of STNS and PBB Mixtures*

SNP Content (Volume Fraction)	STNS	PBB
0.00	0.000	0.000
0.10	0.325	0.190
0.20	0.388	0.333
0.50	0.747	0.563
0.75	0.939	0.903
1.00	1.000	1.000

Considering the similarity between the DPI and SCI approaches, one can extend the analysis of DPI values in the same manner as was done with the SCI. Fig. 21 shows the DPI for SMY mixtures with 95% confidence intervals included. As such, Fig. 21 resembles the left side of Fig. 14 for the SCI approach. Table 9 shows the mean DPI and the respective standard deviations corresponding to the data in Fig. 21.

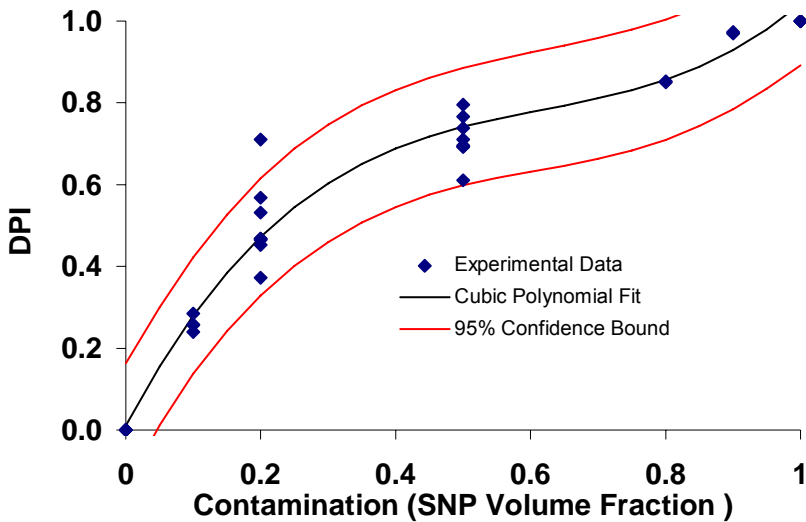


Figure 21: *DPI data and fit with 95% confidence bounds for all runs of mixtures of SMY crude oil and SNP base oil.*

As with SCI, one can compare the reliability of DPI values with the other approaches by comparing the width of the confidence interval at 20% contamination. This width is 0.19 for the DPI in Fig. 21. The units for this quantity are units of SNP volume fraction. This compares to a width of 0.23 for the $T_{2,LM}$ confidence interval and 0.11 for the SCI confidence interval, both at 20% contamination. This implies that the DPI is an improvement over treatment with $T_{2,LM}$, but does not perform as well as the SCI.

Table 9: *DPI Obtained from Model Parameters for T_2 Domain Fits of SMY Mixtures*

SNP Content (Volume Fraction)	Mean
0.0	0.00 ± 0.00
0.1	0.26 ± 0.02
0.2 (Both Samples)	0.50 ± 0.10
0.5 (Both Samples)	0.71 ± 0.06
0.8	0.85 ± 0.00
0.9	1.00 ± 0.03
1.0	1.00 ± 0.00

Conclusions

Mixtures of three crude oils and SNP have been measured, yielding NMR T_2 relaxation times and viscosity values. Incremental T_2 distributions show that more viscous crude oils show a greater effect from contamination with SNP. For all sets of mixtures, effects were more pronounced in samples with more SNP content. The mixtures behave according to the Morriss correlation, relating viscosity to $T_{2,LM}$. Furthermore, mixture log-mean relaxation times and viscosities can be interpolated to a moderate degree of accuracy with Equations 3 and 4, respectively.

In order to improve accuracy, a scheme to use the data in T_2 relaxation time bins was used. Starting with cumulative distributions in the T_2 domain, a selective contamination index is calculated from bins that show a strong dependence on concentration. This method yields strong correlations for contamination when appropriate bins are selected. For these bins, the binwise contamination indices at measured SNP concentrations are consistent, as indicated by the small standard deviations in Table 6 and 7. Polynomial interpolations are then used to construct curves that extend over the entire SNP concentration range. These curves can be used to obtain concentrations, or contamination levels, from the SCI.

Another method pursued is the characterization of contamination by fitting CPMG data to a skewed Gaussian distribution. An index is developed from a subset of the parameters in this distribution. Namely, the model mode and short-time standard deviation factor, are combined into a distribution parameter index (DPI). DPI can be correlated to contamination.

Comparing the two methods above, the DPI is less reliable than the SCI in terms of the uncertainty in degree of contamination corresponding to a particular index value. However, it does outperform the $T_{2,LM}$ method using the same criteria. Thus, using the SCI or DPI approaches would be recommended improvements to characterizing contamination using $T_{2,LM}$.

Acknowledgements

The authors would like to acknowledge the Consortium on Processes in Porous Media at Rice University and the US DOE Grant DE-PS26-04NT15515 for financial support. In addition, Dr. Robert Freedman of Schlumberger was instrumental in motivating the measurements mentioned.

References Cited

- Akkurt, R., Fransson, C.-M., Witkowsky, J.M., Langley, W.M., Sun, B., and McCarty, A. 2004. "Fluid Sampling and Interpretation with the Downhole NMR Fluid Analyzer." Paper 90971 presented at the 2004 SPE ATCE. Houston, TX.
- Bouton J., Prammer M. G., Masak P., and Menger S. 2001. "Assessment of Sample Contamination by Downhole NMR Fluid Analysis." Paper 71714 presented at 2001 SPE ATCE. New Orleans, LA.
- Chen, S., Zhang, G, Kwak, H., Edwards, C.M., Ren, J., and Chen, J. 2004. "Laboratory Investigation of NMR Crude Oils and Mud Filtrates Properties in Ambient and Reservoir Conditions". Paper 90553 presented at 2004 SPE ATCE. Houston, TX.
- Chuah, T. L. 1996. *Estimation of Relaxation Time Distribution for NMR CPMG Measurements*. M.S.Thesis. Rice University, Houston, TX.
- Lo, S.-W. 1999. *Correlations of NMR Relaxation Time with Viscosity/Temperature, Diffusion Coefficient and Gas/Oil Ratio of Methane-Hydrocarbon Mixtures* Ph.D. Thesis. Rice University, Houston, TX.
- Masak P. C., Bouton J., Prammer M. G., Menger S., Drack E., Sun B., Dunn K.-J., Sullivan, M. "Field Test Results and Applications of the Downhole Magnetic Resonance Fluid Analyzer," paper GGG, presented at SPWLA 43rd Annual Logging Symposium. Oiso, Japan (2002).
- Morriss, C.E., Freedman, R., Straley, C., Johnston, M., Vinegar, H.J., and Tutunjian, P.N. 1997. "Hydrocarbon Saturation and Viscosity Estimation from NMR Logging in the Belridge Diatomite." *The Log Analyst*. March-April, p. 44.

Subtask 2.2: Application of restricted diffusion for characterization of vuggy carbonate formations.

Parameter Selection for Restricted Diffusion in Pores Modeled as Spheres

Introduction

The use of restricted diffusion measurements to evaluate pore size distributions can be approached by approximating the pore network as a system of spheres of varying sizes. Pores are represented as a distribution of spheres with radii matching the characteristic length scales of the pore network. Long-range connectivity would be represented by a series of spheres of increasing radius. Preferred parameters for Pulsed Field Gradient – Stimulated Echo Diffusion Editing (PFG-SE DE) measurements in rocks modeled as a set of spheres are determined using an existing model for NMR signal attenuation in spheres. This model is commonly employed in evaluated emulsion systems, but has not previously been carefully examine for use in rock samples^{2,3,8,9}.

The first step is to establish a procedure for determining preferred parameters for a PFG-SE DE pulse sequence to evaluate a given pore size. Then a set of multiple pulse sequences can be designed to best evaluate a wide range of pore sizes. The results of these pulse sequences can be inverted as two-dimensional pore size (a) vs T_2 relaxation maps. These maps are only valid for a range of pore sizes dependant on the selected parameters, and each map must only be considered within the range of its own validity. A method of combining multiple maps is developed to present the results as a weighted combination of the valid ranges of all the contributing maps. The combining process uses masks to eliminate artifacts from regions of a and T_2 space where a particular set of parameters does not provide sensitivity. The masked data is then normalized to determine the scale factor for each mask. Finally the masks are applied and the masked data summed to a single composite map.

To demonstrate the effectiveness of this technique, simulated NMR data for small groups of spheres are developed and the masks are applied. Following that, experiments on grain packs of dolomite sands saturated with water and pentane were performed. Finally, the interpretation techniques were applied to diffusion data from vuggy carbonate rocks obtained before the optimization techniques were developed. The carbonate samples were saturated with methane, water, and in some cases ethane.

The PFG-SE DE Pulse Sequence

The PFG-SE DE sequence is shown in Fig. 1⁵. The equation for the estimation of apparent diffusivity and T_2 distribution function, $f(D, T_2)$, from magnetization is shown in Equation 1. The parameter δ refers to the gradient

pulse duration. The parameter Δ refers to the spacing between the gradient pulses. The sum of the gradient pulse duration and the gradient pulse spacing is often called the diffusion time, t_D . g is the gradient strength, D is the fluid diffusivity, and γ is the gyromagnetic ratio (in radians) of the protons being observed. T_1 and T_2 are the characteristic longitudinal and transverse relaxation times of the system. A typical single data set consists of the collection of 3000 to 5000 echoes with g , δ , and Δ held constant. A suite of data would include data sets collected at 15 to 20 values of g , with δ and Δ still held constant. A suite of data can be inverted to determine the populations of D and T_2 through an algorithm discussed below¹¹.

$$M(g,t) = \iint dDdT_2 f(D,T_2) e^{-t/T_2} \frac{1}{2} \exp\left\{-\gamma^2 g^2 \delta^2 D \left(\Delta - \frac{\delta}{3}\right)\right\} \times \exp\left\{-\frac{\Delta + \delta}{T_1} - 2\delta \left(\frac{1}{T_2} - \frac{1}{T_1}\right)\right\} \quad (1)$$

Model for Attenuation in Spheres

The series solution for magnetization attenuation in a sphere (A_{sp}) for a PFG-SE measurement is shown in Equations 2 through 4^{3,4,5}. Equation 5 shows the asymptotic solution for large values of a , or free diffusion. Equation 6 shows the asymptotic solution for small values of a , or complete restriction. For a given sphere radius a , the attenuation depends on the NMR pulse sequence parameters as well as the self-diffusion constant of the saturating fluid. This suggests that the selection of pulse sequence NMR parameters has a strong effect on the sensitivity of the signal attenuation to the sphere size. When designing an experiment to evaluate a range of pore sizes in a sample it is necessary to select a list of experimental parameters that will be sensitive to all the length scales of the system.

$$A_{sp} = \exp\left\{-2\gamma^2 g^2 \sum_{m=1}^{\infty} \frac{1}{\alpha_m^2 (\alpha_m^2 a^2 - 2)} \left[\frac{2\delta}{\alpha_m^2 D} - \frac{\Psi}{(\alpha_m^2 D)^2} \right] \right\} \quad (2)$$

$$\Psi = 2 + \exp(-\alpha_m^2 D(\Delta - \delta)) - 2\exp(-\alpha_m^2 D\delta) - 2\exp(-\alpha_m^2 D\Delta) + \exp(-\alpha_m^2 D(\Delta + \delta)) \quad (3)$$

α_m is the m th root of the Bessel function equation

$$\frac{1}{\alpha a} J_{\frac{3}{2}}(\alpha a) = J_{\frac{5}{2}}(\alpha a) \quad (4)$$

$$A_{sp}^{\infty} = \exp(-\gamma^2 \delta^2 g^2 D (\Delta - \frac{\delta}{3})), \quad \Delta \ll \frac{a^2}{2D} \quad (5)$$

$$A_{sp}^0 = \exp(-\gamma^2 \delta^2 g^2 \frac{a^2}{5}), \quad \Delta \gg \frac{a^2}{2D}, \Delta \gg \delta \quad (6)$$

Model Sensitivity

To evaluate the sensitivity of an NMR measurement with experimental parameters Δ , δ , and g and pore size a , it is useful to rewrite the equation with three dimensionless groups⁶. First is the dimensionless gradient momentum factor q_D (Equation 7), where γ is the gyromagnetic ratio (in radians). The second is the dimensionless gradient spacing Δ_D , shown in Equation 8 with Δ as the fluid diffusivity. Third is the ratio of δ to Δ , called r and shown in Equation 9. Equations 10 through 12 show the dimensionless versions of equations 2 through 4. A contour map of signal amplitude at a very small value of r is shown in Figure 2, using the series solution model from Equation 10. This figure indicates that for Δ_D values less than 1, the attenuation is very close to that of free diffusion. In those cases it will be difficult to distinguish restricted and free diffusion, so the experiment will not be sensitive to sphere sizes in this regime. For Δ_D values above 1, attenuation is no longer sensitive to Δ_D . Therefore the minimum Δ_D value for evaluating spheres of a given size would be 1¹. Figure 3 shows a contour plot for $r = 0.2$, the rule-of-thumb maximum value. This solution agree for $\Delta_D < 1$, but shows very different behavior for larger values of Δ_D . In this regime, the attenuation regime is approaching that of a constant gradient spin-echo⁷.

$$q_D = \gamma \delta g a \quad (7)$$

$$\Delta_D = \frac{2D\Delta}{a^2} \quad (8)$$

$$r = \frac{\delta}{\Delta} \quad (9)$$

$$A_{sp} = \exp \left\{ -4 \frac{q_D^2}{r\Delta_D} \sum_{m=1}^{\infty} \frac{1}{\alpha_D^2(\alpha_D^2 - 2)} \left[1 - \frac{\Psi}{r\Delta_D \alpha_D^2} \right] \right\}$$

(10)

$$\Psi = 2 + \exp\left(-\frac{\alpha_D^2 \Delta_D (1-r)}{2}\right) - 2\exp\left(-\frac{\alpha_D^2 r \Delta_D}{2}\right) - 2\exp\left(-\frac{\alpha_D^2 \Delta_D}{2}\right) + \exp\left(-\frac{\alpha_D^2 \Delta_D (1+r)}{2}\right) \quad (11)$$

α_m is the m th root of the Bessel function equation

$$\frac{1}{\alpha_D} J_{3/2}(\alpha_D) = J_{5/2}(\alpha_D) \quad (12)$$

Parameter Selection

The selection of parameters for PFG-SE estimation of sphere sizes takes place in two steps. First, the asymptotic solution can be employed to provide starting estimates of the parameters. For a system defined by its relaxivity, bulk relaxation time, and bulk fluid diffusivity, the parameters necessary to provide attenuation to 1% of the signal remaining can be easily evaluated from asymptotic solution of the model. This serves as a starting estimate; the series solution can be employed to determine exactly what sphere size the parameters selected are most sensitive to. At this point, the mapping between sphere size and NMR parameters is shifted so that for a selected sphere size the most sensitive parameters according to the series solution are used rather than those based on the asymptotic solution.

Figure 2 provides insight into the sensitivity to q_D for small r where the asymptotic solution is applicable. Assuming a sensitive attenuation range between 90% of the signal remaining and 10% of the signal remaining, the range of sensitive q_D values should be determined from the asymptotic solution. Equation 13 show the determination of a_{small} , the smallest sphere radius that will attenuate to 90% of the signal remaining for a set of NMR parameters selected to attenuate sphere a to 10% of the signal remaining.

$$a_{small} = \sqrt{\frac{\ln(0.9)}{\ln(0.1)}} a = 0.214 a \quad (13)$$

The selection of Δ demands that it be as large as possible within the relaxation time of the sample. Therefore it depends on the bulk relaxation of the saturating fluid, the relaxivity of the system, the anticipated sphere sizes being evaluated, and the signal to noise of the system. Equation 14 shows the calculation for the relaxation time for a given a , requiring estimates for the

relaxivity ρ and the bulk $T_{1,2}$. In general, half the relaxation time of the sample should be fine. A larger fraction could be used in systems with high signal-to-noise. When samples with broad distributions of relaxation times are considered, extra considerations should be made. For a sample with fast relaxing components, a Δ value of half of the relaxation time expected for the a_{small} should adequately match the loss of $T_{1,2}$ sensitivity to the loss of diffusion sensitivity. Equation 15 shows the calculation for Δ following this guideline. Examples presented here will follow this guideline, with the understanding that sensitivity to larger pores is reduced in exchange for wider relaxation time sensitivity. The maximum possible sphere size for a sample with given D , ρ , and $T_{1,2,\text{bulk}}$ is a_{max} , determined by the point of intersection between a curve of $\Delta_D = 1$ intersects Equation 15.

$$T_2 = \frac{aT_{2,\text{bulk}}}{3\rho T_{2,\text{bulk}} + a} \quad (14)$$

$$\Delta = \frac{0.214aT_{2,\text{bulk}}}{6\rho T_{2,\text{bulk}} + 0.428a} \quad (15)$$

The selection of δ and g are closely interconnected. Determining both can be simplified by defining two regimes of signal attenuation, g -controlled and δ -controlled, and the sphere radius that separates them, a_{grad} . Equation 16 shows the calculation of a_{grad} , which corresponds to the radius of sphere attenuated to 1% of signal remaining at the maximum possible gradient strength g_{max} and the minimum possible gradient pulse length δ_{min} . For spheres larger than a_{grad} , δ is fixed at δ_{min} , and the gradient is varied so as to sample the full range from 99% of signal remaining ($q_D = 0.225$) to 1% of signal remaining ($q_D = 4.95$). This is the g -controlled range, where g is selected as around 25 values linearly spaced across the range described in Equation 17 and r can be assumed to be very small. In the δ -controlled range, spheres smaller than a_{grad} , it is no longer possible to increase g . The value of δ is determined by equation 18. It should be noted that there are sphere sizes detectable below a_{min} according to Equation 13, so the smallest detectable sphere size will be called $a_{\text{min,small}}$. Figure 4 shows the interactions between $T_{1,2}$, Δ , δ , and g following the guidelines presented here for a system with the diffusivity of methane ($6.8 \times 10^{-4} \text{ cm}^2/\text{s}$), a surface relaxivity of $1.5 \mu\text{m}/\text{s}$, and a bulk relaxation time of 8 seconds.

$$a_{\text{grad}} = \frac{4.95}{\delta_{\text{min}} \gamma g_{\text{max}}} \quad (16)$$

$$\frac{0.225}{a \gamma \delta_{\text{min}}} \leq g \leq \frac{4.95}{a \gamma \delta_{\text{min}}}, \quad a > a_{\text{grad}} \quad (17)$$

$$\delta = \frac{4.95}{a\gamma g_{\max}}, \quad a < a_{grad}, \quad \delta_{\min} \leq \delta \leq 0.2\Delta \quad (18)$$

Determining the ‘shift’ in NMR parameters to match the ideal parameters selected for the asymptotic solution to the sphere size they are most sensitive to for the full series model is straight forward but computationally expensive. For each sphere size between a_{\min} and a_{\max} , the real most sensitive sphere size must be determined.

An example plot of the determination of the most sensitive sphere size using attenuation profiles for a range of sphere sizes is shown in Figure 5. The square of the difference between the attenuation of each sphere and the attenuation of the nearest sphere sizes in either direction is summed over all g values. This sum is then plotted against pore size to determine the range of sphere sizes that show enough difference to be distinguished, based on the signal to noise. Figure 6 shows a plot of the sum of square differences. The maximum range of sensitivity is taken to be all sphere sizes is greater than 45% of the peak sum of squares sphere attenuation for smaller spheres. For larger spheres, where sensitivity is less, the cutoff is 98%. The horizontal cutoff lines are drawn at those values to intersect the curve at the minimum and maximum measurable sphere radii.

Once the corrected most sensitive size for each set of parameters is determined, Fig. 4 can be redrawn with the sizes all shifted, as in Fig. 7. The a_{\min} is increased because as δ increases, a larger q_d is required so at some point dependant on the parameters, simply increasing δ has no effect on the most sensitive sphere size. At this point no smaller spheres can be detected. The new a_{\min} is the point where the most sensitive sphere size is first different than that of the adjacent smaller sphere. a_{\max} also is increased, as the shift also applies to larger spheres. The relaxation time cushion of 0.5 times the T_2 (or $T_{2,\min}$) should be enough to avoid signal to noise limitations due to relaxation.

Multiple Sphere Sizes

Systems with multiple sphere sizes require the extension of the techniques described above to multiple pulse sequences over a wider range of sphere sizes. A series of pulse sequences with parameters selected for sphere sizes logarithmically spaced between the maximum and minimum desired sphere sizes for evaluation would provide a careful sweep of the full range of sphere sizes expected in the system.

The saturating fluid diffusivity is constrained by the fluids available and the temperature. In general, slower-diffusing fluids are most appropriate for very small pores, while faster-diffusing fluids are more appropriate for larger pores. Fast-diffusing fluids often cannot characterize small pores due to equipment limitations on the minimum gradient pulse spacing. Slow-diffusing fluids cannot characterize large pores as they relax before diffusing far enough. A full suite of experiments may integrate multiple saturating fluids, but in the present examples we will consider only one saturating fluid at a time.

Equipment and experimental constraints need to be considered as well. Most NMR apparatuses have a minimum possible diffusion time, as there are limits to how close gradient pulses can be without interfering with each other. Maximum diffusion times remain constrained by the relaxation time of the sample. Minimum gradient pulse durations depend on the linearity of the gradient. Maximum gradient pulse duration tends to depend on the spacing of the gradient pulses. The gradient coil will place a maximum on the possible gradient strength. The coil might also place a minimum on the gradient strength if the coil does not provide a stable gradient for very low gradients.

Mask Design

Mask design is the process of selecting a suite of NMR parameters that will provide sensitivity to the entire desired range of sphere sizes. Each single set of NMR parameters will provide a complete contour map of sphere size and relaxation time, but it will only be sensitive to a relatively narrow range. The masks are employed to weight only the sensitive region of each map, so they can be combined into a summary. The first step is therefore to determine the range of sphere sizes to investigate and selected a logarithmically spaced subset to act as the centers of each mask. The techniques presented above will determine the NMR parameters corresponding to each size in the subset. The sensitive range of each set of parameters is determined as in Fig. 6. To demonstrate this, a simulated system with parameters summarized in Table 1 is examined. Fig. 8 shows the sum of square differences for each of the pulse sequences in the suite, from which the sensitive size ranges can be determined. Note that in this example, methane is used as the saturating fluid.

The next step is to combine the results from each pulse sequence into one result to cover the entire range of pore sizes. The sensitive ranges described by Figure 8 are used to design masks. These masks balance the contributions from each pulse sequence to give the most weight when the sequence is most sensitive. The mask then use a triangular window to reduce the weight till the sequence becomes insensitive. A plot of mask ranges is shown in Figure 9. For this set of masks, the lower limit of the sphere size the sphere that has a square difference in amplitude from adjacent sizes that is 45% of the peak square

difference in sphere amplitudes. The upper limit is 98%, as larger spheres are difficult to resolve and introduce errors in amplitude. If the set of masks left gaps between and of the masks, either a broader mask must be employed, or a larger subset of sphere sizes to be the mask centers should be used.

A set of examples is illustrated to demonstrate the need for masks. Figure 10 shows a simulated data set where the diffusion length is much smaller than the sphere radius. These pulse sequence parameters were not sensitive to spheres of the size used in the simulation. The solid line shows the most sensitive region of the pulse sequence. The dashed lines show the upper and lower boundaries of sensitivity. All contributions from this measurement would be excluded from summary as they fall outside the mask. Figure 11 shows a set of simulated data where the sphere radius and the diffusion length are similar. In this case, all of the results would be included in the composite map. Finally, Figure 12 shows a set of simulated data where the diffusion length is much larger than the sphere radius.

Each pulse sequence also has an inherent valid range in relaxation space in addition to the sensitive range in pore size. Relaxation that occurs during the diffusion time of the measurement is no longer available for evaluation when the first echo is collected. For that reason, it is important to consider each mask in two dimensions – pore size and transverse relaxation time. Depending on signal to noise, relaxation times shorter than a fraction of the diffusion time should be excluded. We will use 50% in these examples. To exclude relaxation times shorter than this limit, a second mask is applied to the results of each pulse sequence, starting at zero for all T_2 less than or equal to half of Δ . The mask then ramps up linearly in log T_2 to 1 when T_2 is equal to Δ , and remains there for all greater T_2 values. Figure 13 shows a set of T_2 masks. A 2-D plot of the sensitive region of the same data set shown in Table 1 is shown in Figure 14. This plot is obtained by summing up all the masks generated for this system, including sphere size and T_2 .

Simulation Background

In order to better understand the relationship between diffusion length and sphere radius, random walk simulations of self-diffusion inside spheres were performed. A number of simulations of diffusion in spheres exist^{2,4,10}, but for this study only a simple investigation is required. The total displacement due to self-diffusion at selected diffusion times was determined in spheres of a range of sizes. The 3-D diffusion length described in Equation 19 can be used to characterize the relationship between the diffusivity of the diffusing fluid and the distance in one direction it would travel if unrestricted. Diffusion length is a measure of diffusion time, but has been transformed to units of length by the molecular diffusivity. It is the root mean squared distance traveled by the bulk probe fluid if it is unrestricted by pore walls. As a unit of length, it can be

compared with the displacement of a molecule in a restricted system to compute the ‘observed diffusivity’.

$$L_d^{3D} = \sqrt{\frac{6D(\Delta + \delta)}{a^2}} \quad (19)$$

The results obtained from the simulation are summarized in Figure 15, showing displacement as a function of diffusion length for a number of sphere radii. The radius of each sphere indicated by an X on the edge of the plot. The limit of the displacement was slightly more than the radius of the sphere for all spheres with radii less than the diffusion length. Free diffusion occurred throughout the simulation for spheres with radii larger than the maximum diffusion length. The same results are plotted again in Figure 16, this time with the displacement and the diffusion length made dimensionless by dividing by the sphere radius. All results fall along the same curve, indicating that restricted diffusion displacement in a sphere scales with the size of the sphere.

The displacements obtained from simulation can be converted to observed diffusivities using Equation 20 for three dimensions. Simulated NMR data for a system of spheres is generated using the simulation results as a guideline for predicting the observed diffusivity of a sphere. The magnetization equation for PFG-DE measurements is shown in Equation 1⁵. The results are then inverted as described below. Multiple NMR simulations on the set of sphere sizes can be performed to generate a suite of data that can be combined into one inclusive result using the masking technique described previously.

$$\frac{D_{obs}}{D_0} = \frac{\langle r^2 \rangle}{6D_0 t_d} = \frac{\langle r^2 \rangle}{l_d^2} \quad (20)$$

Two-Dimensional Inversions for Relaxation and Pore Size

The data generated in a real or simulated NMR response consists of a suite of 10 - 20 sets of echo data, each with a different set of gradient strengths. Each data set in the suite collects several thousand echoes for the sequence for selected values of δ , Δ , and g . The suite collects all data sets that have the same value for Δ . Two-dimensional a - T_2 maps are generated for each data suite using a two-dimensional inversion analogous to that used for inverting D - T_2 information^{5,11}. A sample data set is shown in Figure 17.

The first step of the inversion is to divide a space and T_2 space into bins. T_2 space is usually divided in 100 bins between 1×10^{-4} and 10. Pore size is usually divided into 60 bins between 1×10^{-3} and 1 centimeter. The model in

Equation 2 can be substituted for the diffusion kernel in Equation 1, resulting in Equation 21. A matrix of predicted results for each a and T_2 bin is generated using this model. The two dimensional inversion is used to calculate the population in each $a - T_2$ bin that would be multiplied by the matrix of predicted values to produce a magnetization decay that matches that of the experiment.

The results are smoothed by regularization using an α parameter selected by inspection. The inspection procedure is to prepare $a - T_2$ maps for a series of α values, and select the map that appears most characteristic of the full range of α values. No technique for algorithmically selecting α is available at this time. The current technique is not quantitative so it is useful to check multiple values of α to ensure map features are not regularization artifacts.

$$M(g,t) = \iint dDdT_2 f(a,T_2) e^{-t/T_2} A_{sp}(\Delta_D, q_D, r) \times \exp\left\{-\frac{\Delta + \delta}{T_1} - 2\delta\left(\frac{1}{T_2} - \frac{1}{T_1}\right)\right\} \quad (21)$$

Simulation Results: Spheres

The first suite of simulated data generated using the parameter set described in Table 1 consisted of a single sphere of radius 0.003 cm, with an associated relaxation time of 720 ms. Ten suites of PFG-SE DE measurements at 25 different gradient strength values were generated. The sets were inverted to maps using moderate regularization ($\alpha = 18$) and then combined using 2-dimensional masks. The combined result is shown as a summary map in Figure 18, with sidebars showing the projected results both for relaxation time and pore size. Figure 19 shows the placement of this sphere on the sensitivity map from Figure 14. The sphere is near the border of the sensitive region of the color map, indicating that sensitivity to that sphere size is adequate. Any sphere outside of the most sensitive region would be poorly characterized by this set of parameters, and would require a different set of parameters to evaluate. Figure 20 shows the summary map for a data set where the sphere fell outside of the sensitive region. Signal is only visible in the area overlapped by the sensitive region. Figure 21 shows a summary map for a full set of spheres. The sensitive region is shown in Figure 22. Spheres outside the sensitive region are not retained in the masked map, while spheres inside the region are all recovered. Spheres on the border are quite dispersed, but correctly placed. The peakiness of the spheres depends somewhat on their location, but all spheres away from the left-side limit of the sensitive region have approximately the same integral.

Figure 23 shows an example of randomly oriented cylinders of a single radius (0.003 cm). It is simulated as 11 different orientations spaced evenly between 0 and $\pi/2$ radians, though little difference would be visible for 100 different orientations. The amplitude extends upwards from radius in a streak,

though the amplitude peaks close to the cylinder radius and disappears near the edge of the sensitive region. The amplitude of this streak represents the distribution of diameters a cylinder would show in the plane of the magnetic field gradient using the technique of generating cylinder orientations employed, shown in Figure 24.

Discussion: Simulation.

Having established the effectiveness of the masking process, the selection of the mask width can be revisited. The discrepancies discussed here arise from the differences in model performance in identifying spheres larger than the most sensitive sphere versus those smaller. The shape of Fig. 5 gives a hint of the reason for this discrepancy – larger spheres drop off very quickly, so much of the difference occurs in relatively few points. For the smaller spheres, the difference in amplitudes is developed more gradually. As the diffusion length increases, the fast drop of the larger spheres becomes more pronounced.

In the single-sphere example shown previously in Fig. 18, the total amplitude recovered matches the input amplitude very well. When masks are symmetrically based at 45%, 75%, or 98% of the peak square difference in sphere amplitudes, the total signal amplitude remains within 5% of the input value of 1. This sphere is placed near the lower edge of the sensitive region, where most of the overlap arises from the smaller pore-size region of progressing triangles.

Near the upper edge of the sensitive region, amplitude is not recovered as easily. Figure 25 shows a multiple spheres at the upper edge of the sensitive region with masks based on 45% of the peak square difference in sphere amplitudes. The integral of the upper right peak is only 0.67 when it should be 1. Raising the mask limit value to 75% improves the amplitude to 0.85. Finally, bringing the mask limit to 98% of the peak square difference in sphere amplitudes brings the integral to 0.97. Fig. 26 shows the map that corresponds to these conditions.

Considering this information together, it becomes clear that a very narrow mask provides the most precise information. The obvious trade-off is that a narrow mask covers the narrowest range of sphere sizes. To illustrate this point, compare the set of masks cut off at 45% of the peak square difference in sphere amplitudes shown in Fig. 27 and the set of masks cut off at 98% of peak square difference in sphere amplitudes shown in Fig 28. The narrow set minimizes mask overlap and redundancy, but also minimizes the overall range of sphere sizes evaluated. The obvious compromise is to use a different cutoff for the upper and lower edges of the mask. Based on the performance of the masks in Figures 18, 25, and 26, the masks employed for analyzing experimental results here will use a smallest-size cutoff of 45% of peak, and a largest size cutoff of

98% of the peak value for square difference in attenuation in spheres. A plot of the sphere from Fig. 26 using these masks would be visually indistinguishable. More on the comparison of masks to unmasked data will be presented in the discussion of experimental data.

Results I: Dolomite Grain Packs.

The dolomite grain pack measured here was sieved to include grains between 100 and 140 microns, corresponding to a very well sorted fine grain pack. The porosity is expected to be around 40 p.u., and the permeability should be in the 7-14 darcy range. This grain pack was saturated first with water, and then with pentane. Measurements were performed with parameters selected following the techniques detailed above. The surface relaxivity was assumed to be $1.5 \mu\text{m}/\text{s}$.

The summary map for the water-saturated grain pack is shown in Fig. 29. The details of the summary map are difficult to interpret because the peaks fall very close to the limits of the sensitive region, pictured in Fig. 30. There appears to be a set of pores around 20 microns, and some evidence of larger pores. To better understand the evidence presented in this picture, it is useful to compare it to Fig. 31, which shows the unmasked sum of all the maps developed in this experiment. The summary shows the peak centered around 20 microns or slightly larger, but spread broadly over several decades of sphere sizes. This indicates that several of the experiments were not sensitive to spheres of that size. The sum also shows a very large peak at around 30-70 microns that does not appear in the masked summary. The absence of this peak from the masked version must indicate that this peak is not reliably resolved, and indeed it falls just outside the sensitive region. To better evaluate this region, it is useful to extend the upward spread of the sensitive region, which can be accomplished by using a faster-diffusing fluid such as pentane.

The summary map for the pentane-saturated grain pack is shown in Fig. 32. The sensitive region is shown in Fig. 33, approximately doubling the maximum size available for water-saturated samples. The small peak visible in the water measurements is no longer within the sensitive region, but now a peak around 70 microns, again at the very top of the sensitive region. No tail down to 30 microns is visible, indicating that the range shown in the sum of the water maps was spurious. Looking now at the sum of all the maps from the pentane in Fig 34, the peak at 70 microns appears to extend upward to over 100 microns. The continuing extension of this particular peak to longer times suggests it represents bulk or bulk-like fluid. Bulk-like fluids would include fluid in pores enough larger than the maximum diffusion length that no change in attenuation due to restriction is observed. Bulk-like fluids would also include inter-connected pathways throughout the sample, including the approach to the tortuosity limit. A clearer example of this phenomenon is visible looking at the unmasked sum of

maps for a pack of larger grains (150-300 microns) shown in Fig. 35. For this larger grain pack, no amplitude was observed inside the sensitive range.

Results II: Rock Samples.

Sample 1: 7b

This sample was a vuggy carbonate with a porosity of 22 p.u., a gas permeability of 643 md, and a resistivity-based formation factor of 35. This sample was saturated with water at room temperature and methane at 4000 psi and room temperature. 9 PFG-SE DE measurements were performed. These measurements were performed before the optimization strategy discussed here was developed, so the parameters were not ideal. The masking technique can still be applied.

The summary plot for sample 7b is shown in Fig. 36, and the sensitive region to accompany it is in Fig. 37. One population of pores is visible clustered at the top of the sensitive region. This again suggests that the true pore size is somewhere well above the limits of the sensitive region. Comparing to the unmasked sum in Fig. 38, it is clear that the pores visible in the masked summary make up the smallest section of some far larger system of porosity. The absence of pores between 10 and 100 microns suggests the absence of large pore throats between the vugs of the system, but also the absence of a significant macropore system.

Sample 2: 8a

This sample was a vuggy carbonate with a porosity of 20 p.u., a gas perm of 21 md, and a resistivity-based formation factor of 39. This sample was saturated with water at room temperature, methane at room temperature and 4000 psi, and ethane at room temperature and 600 psi. 12 PFG-SE DE measurements were performed, again without optimized parameters.

The summary plot for sample 8a is shown in Fig. 39, and the associated sensitive region is shown in Fig. 40. Three populations of pore sizes are visible here – small pores between 10 and 30 microns relaxing quick quickly, a second population starting at about 50 microns extending off into very large sizes. The smaller population does not appear to connect to the vugular porosity, suggesting that it does not represent a population of throats connecting the vugular porosity. Examination of the unmasked sum in Fig. 41 suggests that the large pore population may be much larger than the masked data indicates, but otherwise no new information is revealed.

Sample 3: 2433

This sample was a vuggy carbonate with a porosity of 16.5 p.u., a gas perm of 69 md, and a resistivity-based formation factor of 196. This sample was saturated with water at room temperature, methane at room temperature and 4000 psi, and ethane at room temperature and 600 psi. 12 PFG-SE DE measurements were performed, again without optimized parameters.

The summary map for this sample is shown in Fig. 42, with the sensitive region in Fig. 43. The separate sphere sizes are visible, all distributed along the edge of the sensitive region. All are quite large, from 100 microns up to 300 microns. Examining the unmasked sum in Fig. 44 reveals that one large streak from 10 microns all the way up to a millimeter. This suggests another case similar to the grain packs – large pores well above the range measurable by the experiments performed. In this case, though, there are two populations that appear to represent different relaxation times in the system.

Sample 4: 1315

This sample was a vuggy carbonate with a porosity of 14.7 p.u., a gas perm of 485 md.. This sample was saturated with water at room temperature and methane at room temperature and 4000 psi. 9 PFG-SE DE measurements were performed, again without optimized parameters.

The summary map for this sample is shown in Fig. 45, with the sensitive region in Fig. 46. There is a gap in the sensitive region and 20 microns. This gap has no effect on the results, however, as all amplitude is concentrated around 200 microns, with a tail leading into smaller sizes but reaching outside the sensitive region. The unmasked sum, shown in Fig. 47, again shows signs of amplitude larger than the sensitive region, both with amplitude inside the sensitive region that is not correctly characterized and with the presence of a cloud leading up past 1 millimeter sphere size.

Sample 5: 1603

This sample was a vuggy carbonate with a porosity of 15.7 p.u., a gas perm of 1490 md, and a resistivity-based formation factor of 86.1. The sample has a visible fracture as well, possibly accounting for the very high permeability. This sample was saturated with water at room temperature, methane at room temperature and 4000 psi, and ethane at room temperature and 600 psi. 12 PFG-SE DE measurements were performed, without optimized parameters.

The summary map for this sample is shown in Fig. 48, with the sensitive region in Fig. 49. There is a cluster of amplitude visible in the 200-300 micron range, right at the upper limit of the sensitive region. The relaxation time is quite

short for a pore of that size. The unmasked sum is shown in Fig. 50, showing again the evidence of much larger pores. Unusual in this case is the evidence of two separate trails upward, one at short relaxation times and another adjacent at longer relaxation times. This may be evidence of the fractures evident within this sample, a pathway through the rock that does not exchange with the matrix.

Sample 6: Cordova

This sample was a vuggy carbonate with a porosity of 29.5 p.u., a gas perm of 43.2 md, and a resistivity-based formation factor of 53.9. This sample was saturated with water at room temperature and methane at room temperature and 4000 psi. 9 PFG-SE DE measurements were performed, again without optimized parameters.

The summary map for this sample is shown in Fig. 51, with the sensitive region in Fig. 52. The relaxation time of the visible signal is quite long, near the bulk values of the saturating fluids. The unmasked sum in Fig 53 shows minimal amplitude in the region where the masked summary indicates, suggesting again pores considerably larger than the measurements were able to characterize.

Sample 7: ILS

This sample was a vug-free carbonate with a porosity of 17.8 p.u., a gas perm of 1.5 md. This sample was saturated with methane at room temperature and 4000 psi. 5 PFG-SE DE measurements were performed, again without optimized parameters.

The summary map for this sample is shown in Fig. 54, with the sensitive region in Fig. 55. The most significant difference is that the masked and unmasked results shown in Fig 56 largely agree with the masked result. There is a solid streak of amplitude at a relaxation time of 800 milliseconds that begins around 30 microns and extends upward. In the masked case it ends at the top of the mask, in the unmasked case it continues to the limits of the inversion. This behavior would be consistent with that of a cylindrical pore with a radius around 30 microns.

Emulsion Sample

An emulsion was prepared with 20% water in 80% 233 centipoises crude oil. The emulsion was stirred at 6200 RPM for 5 minutes. NMR emulsion characterization by the technique developed by Pena⁸ indicating a log mean droplet size of 6.6 microns.

The summary map for this sample is shown in Fig. 57, with the sensitive region in Fig. 58. The oil peak portion is largely truncated due to relaxation time limitations, but the water portion of the emulsion is clearly visible around a

relaxation time of 1 s. The projection of the water portion to the Y axis is shown in Fig. 59. The log mean droplet size is indicated to be 6.3 microns, which can be considered good agreement with the results of the other technique.

Discussion.

While simulation results are very positive, none of the grain pack and rock samples measured produced results easily compared to the simulations. Most of the samples showed minimal response inside the masked regions. The interpretation of this situation is clear – the length scales of the system are longer than can be evaluated by the experiments performed. Any shorter length scales show relaxation times outside of the range measurable by the same set of masks. These measurements failed to characterize the pore space of the vuggy carbonate samples. The saturating fluids employed were unable to diffuse fast enough or relax slow enough to evaluate the full pore network.

There is still information to be gleaned from some of these examples. First of all, the dolomite grain pack in Fig. 29 and Fig. 32. The only pores detected at all by the masked data are small and fast-relaxing. These pores were not observed in the pentane-saturated example. The peak corresponding to bulk-like water is not detected by the water-saturated sample. The smaller peak is surely an aspect of the pore geometry, either small pores or throats. The larger peak behaves like a bulk fluid, with the indicated sphere size increasing with diffusion time. This may be bulk water, very large pores, or the long-range movement through connected pores in the system. As the relaxation time is well below bulk, it is most likely that this peak is due to connectivity.

The next interesting example is sample 8a shown in Fig. 39. Unlike the other vuggy carbonates, this sample shows significant amplitude within the sensitive region. The first peak occurs between 10 and 20 microns, near the short-relaxation time edge of the sensitive region. This peak appears separate and distinct from a second peak at around 50 microns and stretching upward to around 300 microns. The smaller peak is likely microporosity or geometric detail. The termination of the larger peak before the end of the sensitive region is a strong indication that a significant portion of the vuggy porosity is between 50 and 300 microns. The large population that does not appear to be in a long-range connected pathway should indicate that the vugular porosity is largely unconnected.

The final example that provides extra insight into the sample is the ils sample in Fig. 54. In this sample, there is a single streak of amplitude starting around 30 microns and stretching to the top of the sensitive region, around 200 microns. The sensitive region of this sample doesn't stretch down below 20 microns, so no evidence of smaller porosity can be expected. Therefore this peak should correspond only to the macropore. In this case, rather than

indicating a single pore size, the map suggests a cylinder or group of cylinders. The relaxation time remains constant, indicating that either there is a single cylinder or the cylinders are in strong communication. Strong communication would indicate that instead of cylindrical pores the signal is due to a connected pore network. This seems the most likely interpretation, and the small base diameter of this network, around 20 microns, might indicate a fairly low permeability.

The emulsion sample, on the other hand, is far easier to interpret. The emulsion examined was better suited for the range of sphere sizes and relaxation times this evaluation technique is sensitive to. Interpretation is made still simpler because in this case the droplets are very close to spherical, and the model employed is based on spheres. There are no connected droplets in the system, as they would coalesce into larger but lower energy spheres. Perhaps this is an indication that a more appropriate model for connected systems would be necessary to develop less ambiguous results.

Conclusions.

Guidelines are given for the selection of NMR parameters for PFG-SE DE measurements for a distribution of sphere sizes. Interpreted measurements with different diffusions lengths are compiled into summaries using masks that utilize only the sensitive region of each map. Sphere sizes outside the sensitive region cannot be accurately resolved.

When extending these techniques to experimental results, comparing masked data to unmasked sums of maps adds to the insight gained from the masked results alone. The results remain limited by the probe length of the saturating fluid, but within the sensitive range there is space to obtain useful information about some ranges of pore sizes. Furthermore, amplitude that is observed to exist within the sensitive region in the unmasked picture, but does not appear in the masked results must indicate the presence of pore sizes much larger than the sensitivity of the experiments. By evaluating the approach to this limitation, the presence of large-scale throats or pathways between vugs should be detectable. This will lead to the possibility of estimating vug connectivity through restricted diffusion measurements.

The limitations of the technique may stretch beyond sensitivity limits. The model employed treats pores as spheres, which still provides useful insight but is clearly an assumption of limited validity. The sphere model is more appropriate for truly spherical systems such as emulsions. For complex systems such as vuggy carbonates, it may remove some of the ambiguity of the results to develop a model that doesn't assume the droplets to be spherical.

References.

1. Codd, S. L., Callaghan, P. T.: "Spin Echo Analysis of Restricted Diffusion Under Generalized Gradient Waveforms: Planar, Cylindrical, and Spherical Pores with Wall Relaxivity," *Journal of Magnetic Resonance*, **137**, (1999)
2. Denkova, P. S. et al.: "Evaluation of the Precision of Drop-Size Determination in Oil/Water Emulsions by Low-Resolution NMR Spectroscopy," *Langmuir*, **20**, (2004)
3. Goudappel, G. J. W. van Duynhoven, J. P. M. and Moeren, M. M. W.: "Measurement of Oil Droplet Size Distributions in Food Oil/Water Emulsions by Time Domain Pulsed Field Gradient NMR," *Journal of Colloid and Interface Science*, **239**, (2001)
4. Hagslatt, H., Jönsson, B., Nyden, M., and Soderman, O.: "Predictions of pulsed field gradient NMR echo-decays for molecules diffusing in various restrictive geometries. Simulations of diffusion propagators based on finite element method," *Journal of Magnetic Resonance*, **161**, (2003)
5. Hurlimann, M. D., and Venkataraman, L.: "Quantitative Measurement of Two-Dimensional Distribution Functions of Diffusion and Relaxation in Grossly Inhomogeneous Fields," *Journal of Magnetic Resonance*, **157**, (2002)
6. Murday, J. S., and Cotts, R. M.: "Self-Diffusion Coefficient of Liquid Lithium," *Journal of Chemical Physics*, **48**, No. 11 (1968)
7. Neuman, C. H.: "Echos of spins diffusing in bounded medium," *Journal of Chemical Physics*, **60**, No. 11 (1974)
8. Pena, A., Hirasaki, G. J. "Enhanced characterization of oilfield emulsions via NMR diffusion and transverse relaxation experiments." *Adv. Colloid & Interfacial Sci.* (2003)
9. Packer, K. J., and Rees, C.: "Pulsed NMR Studies of Restricted Diffusion I. Droplet Size Distributions in Emulsions," *Journal of Colloid and Interface Science*, **40**, No. 2 (1972)
10. Sukstanskii, A. L., and Yablonskiy, D., A.: "Effects of Restricted Diffusion on MR Signal Formation," *Journal of Magnetic Resonance*, **157**, (2002)
11. Venkataraman, L., Song, Y.Q., Hurlimann, M. D.: "Solving Fredholm Integrals of the First Kind With Tensor Product Structure in 2 and 2.5 Dimensions," *IEEE Transactions on Signal Processing*, **50**, No. 5 (2002)

Table 1

Parameter	Value
Maximum Gradient Strength (g_{\max})	50 g/cm
Number of Gradient Strengths	25 (spaced linearly)
Minimum Δ Constraint	0.01 s
Number of I_d values	10 (spaced logarithmically)
Fluid Bulk Relaxation	8 s
Fluid Diffusivity	$6.8 \times 10^{-4} \text{ cm}^2/\text{s}$ (methane)
Minimum Gradient Pulse Width (δ_{\min})	0.002 s
Surface Relaxivity	$1.5 \times 10^{-3} \text{ cm/s}$

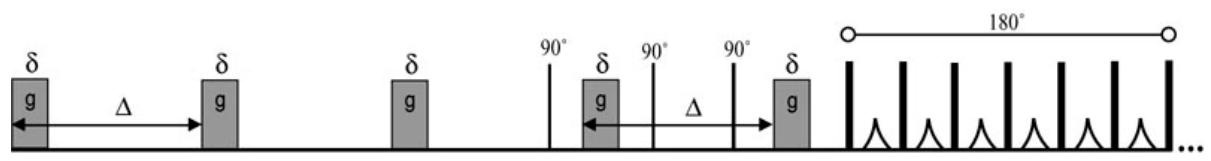


Figure 1: The PFG-SE DE Pulse sequence.

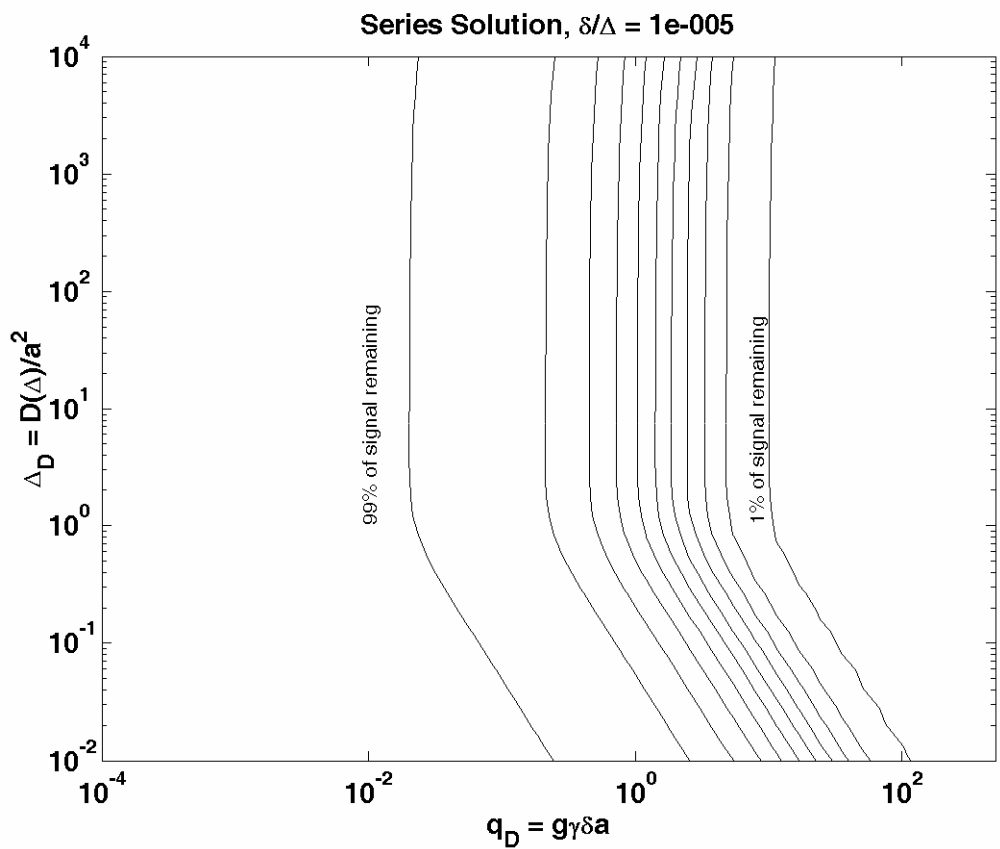


Figure 2: Contour plot of attenuation in spheres for a small value of r , where $r = \delta/\Delta$. The contour lines represent 99, 90, 80, 70, 60, 50, 40, 30, 20, 10, and 1% of the signal remaining.

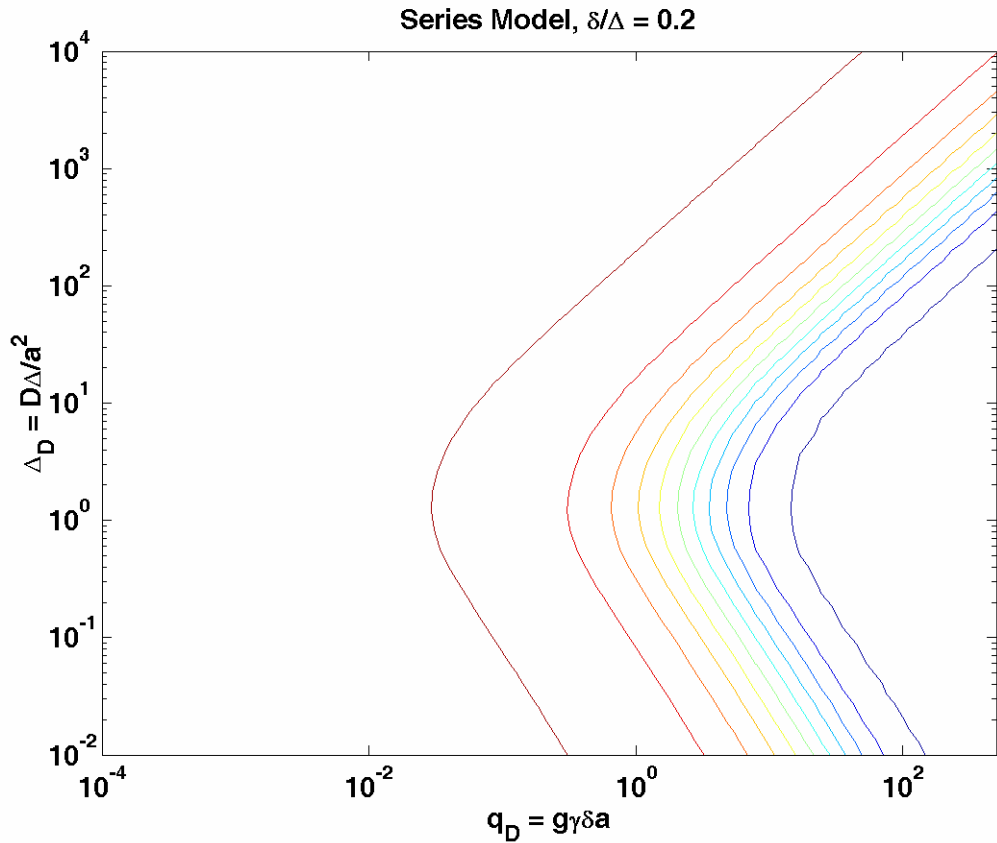


Figure 3: Contour plot of attenuation in spheres for a large value of r , where $r = \delta/\Delta$. The contour lines represent 99, 90, 80, 70, 60, 50, 40, 30, 20, 10, and 1% of the signal remaining.

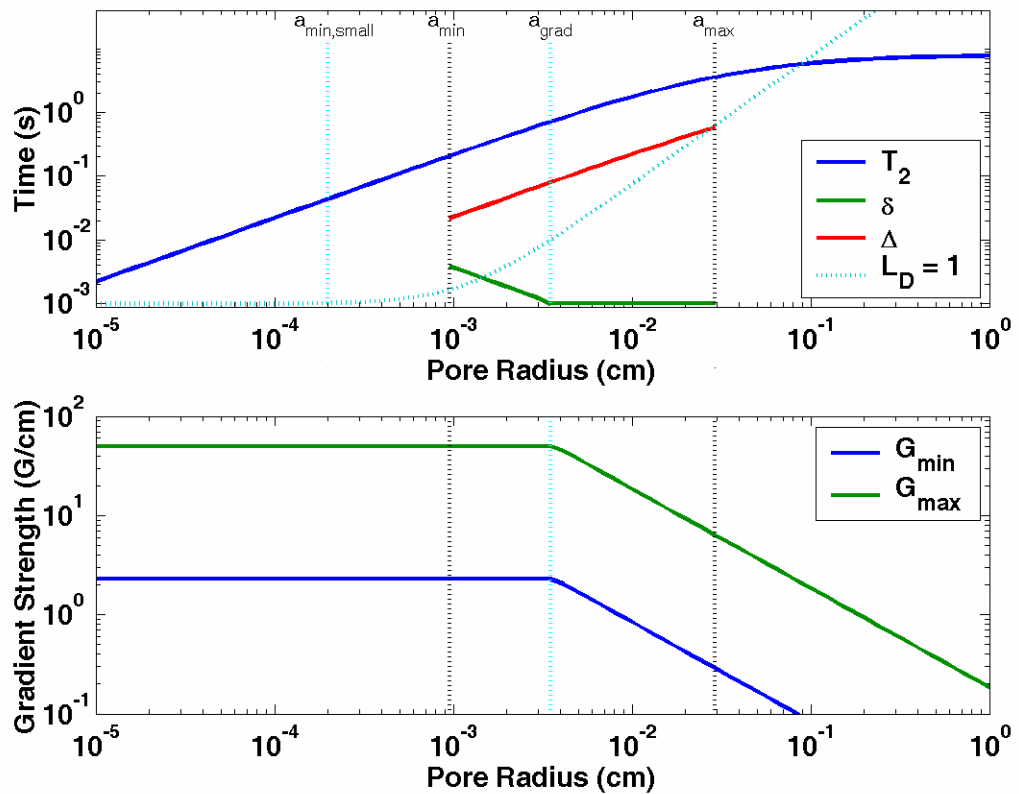


Figure 4: Parameter scheme for a PFG-SE DE measurement based on the asymptotic solution. The input parameters are $D = 6.8 \times 10^{-4} \text{ cm}^2/\text{s}$, $\rho = 1.5 \times 10^{-3} \text{ cm/s}$, and $T_{1,2,\text{bulk}} = 8 \text{ s}$.

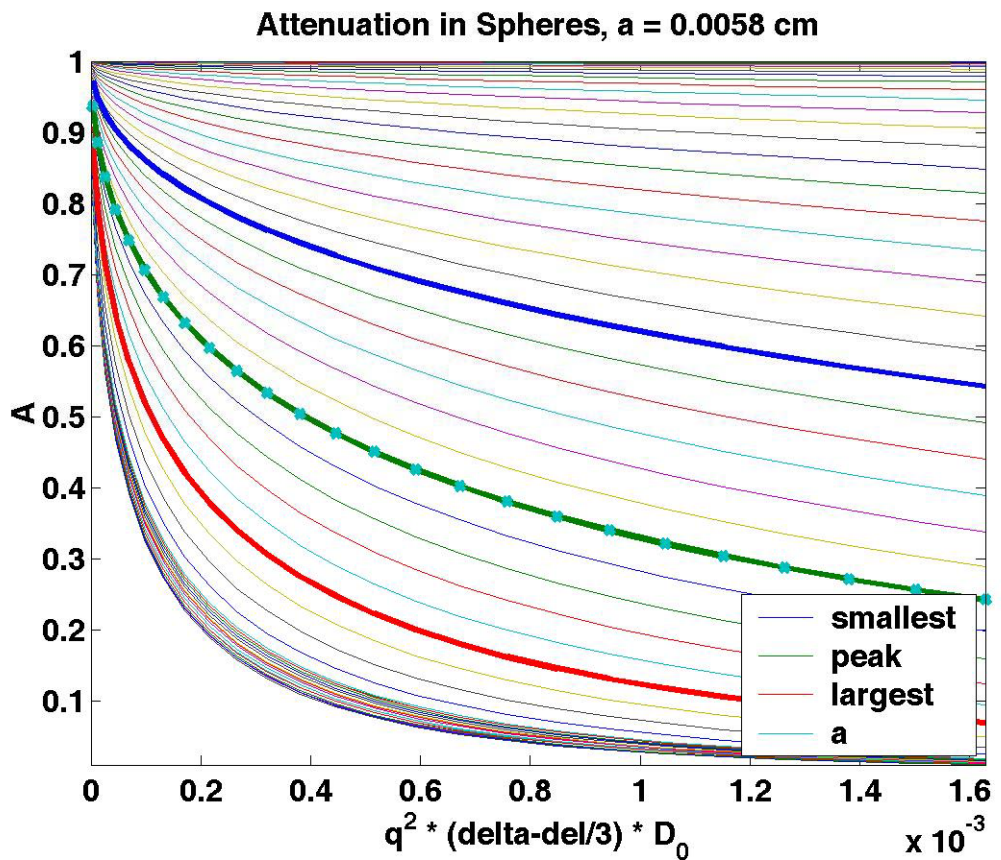


Figure 5: Attenuation in a range of sphere sizes at a selected diffusion length. The δ value here is 0.001 s, diffusivity is 6.8×10^{-4} cm²/s there are 60 radii range spaced logarithmically from 1×10^{-4} cm to 1×10^{-1} cm, and the range in gradient strengths is 1 to 25 g/cm, with 25 values spaced logarithmically. Δ is 0.018 s.

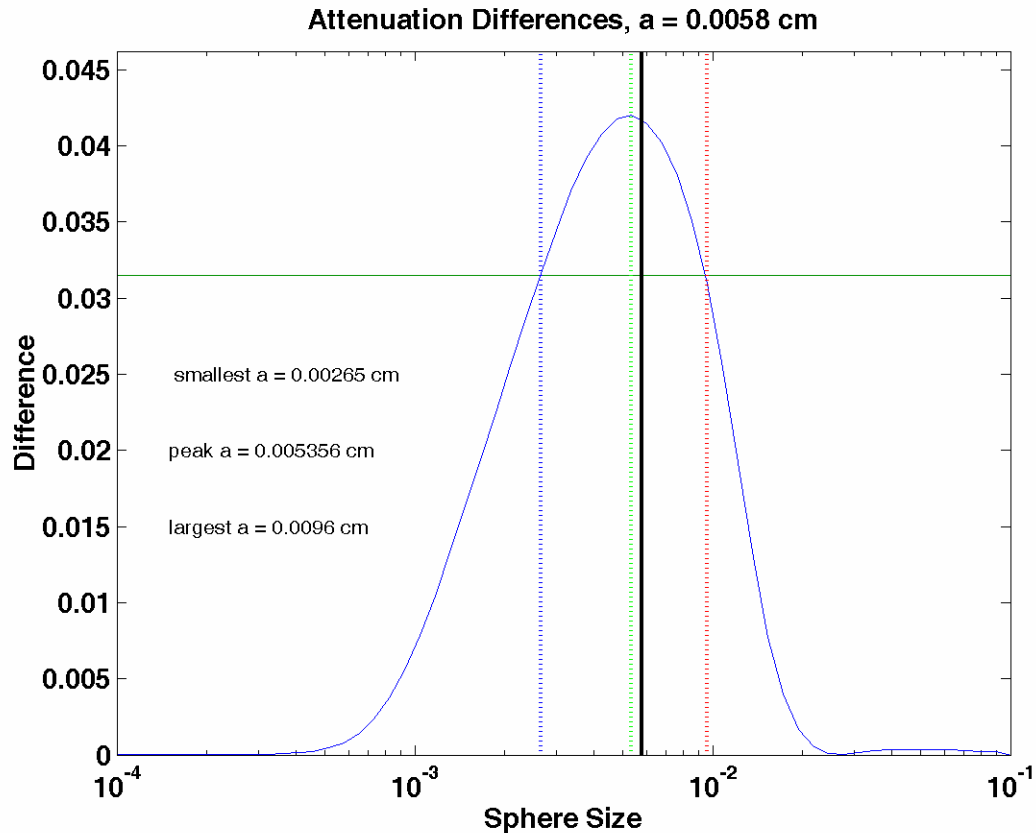


Figure 6: Sum of Square differences for attenuation profiles of spheres. The δ value here is 0.001 s, diffusivity is 6.8×10^{-4} cm²/s, and the range in gradient strengths is 1 to 25 g/cm, with 25 values spaces linearly. Δ is 0.018 s. The green horizontal line indicates 75% of the peak sum of squares. The black vertical indicates the sphere size for which this data set was prepared.

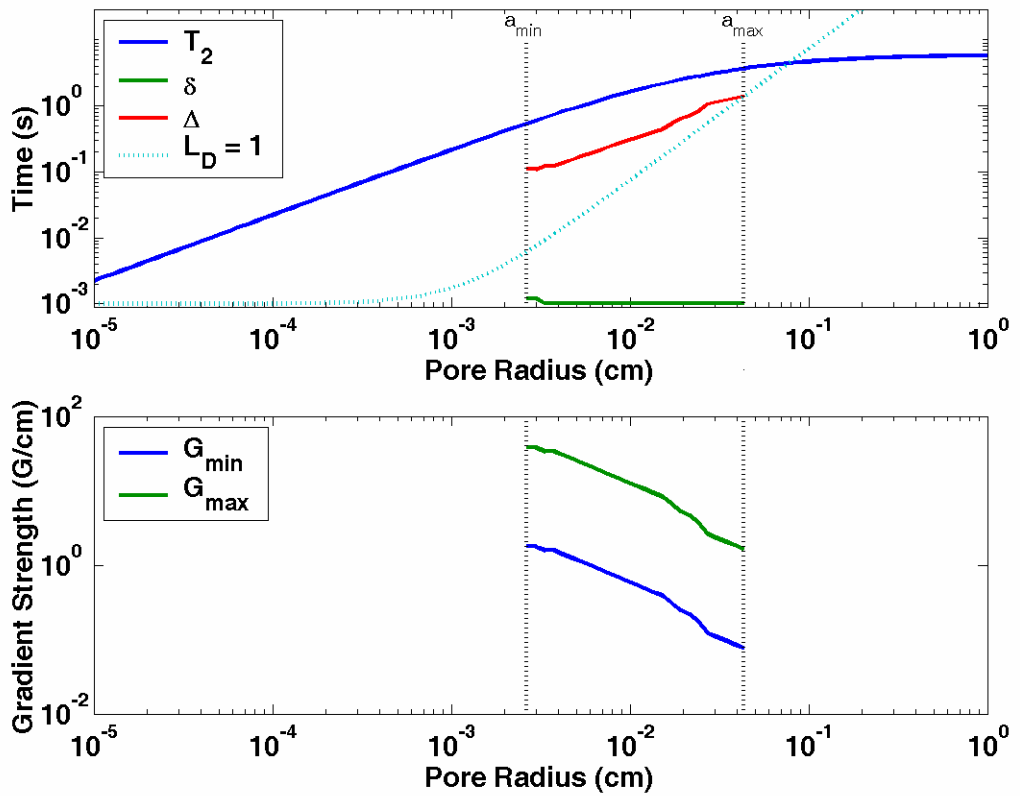


Figure 7: Parameter scheme for a PFG-SE DE measurement based on the full series model, shifted from the asymptotic version in Figure 4. The input parameters are $D = 6.8 \times 10^{-4}$ cm 2 /s, $\rho = 1.5 \times 10^{-3}$ cm/s, and $T_{1,2,\text{bulk}} = 8$ s.

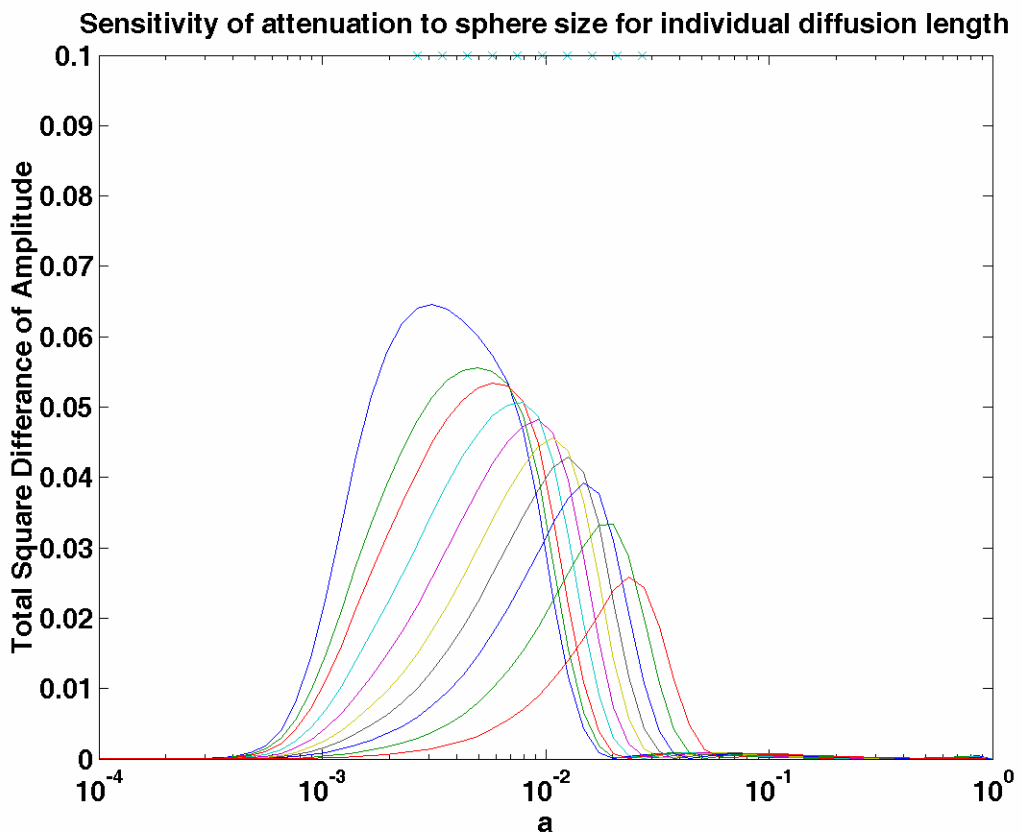


Figure 8: Sum of Square differences for attenuation profiles of spheres over a range of experimental parameters, summarized in Table 1. Diffusivity of the saturating fluid is $6.8 \times 10^{-4} \text{ cm}^2/\text{s}$ (methane). The relaxivity of the system was $1.5 \times 10^{-3} \text{ cm}$ and the bulk relaxation time was 8 s. The x signs indicate the radii for which the parameters of each data set were selected.

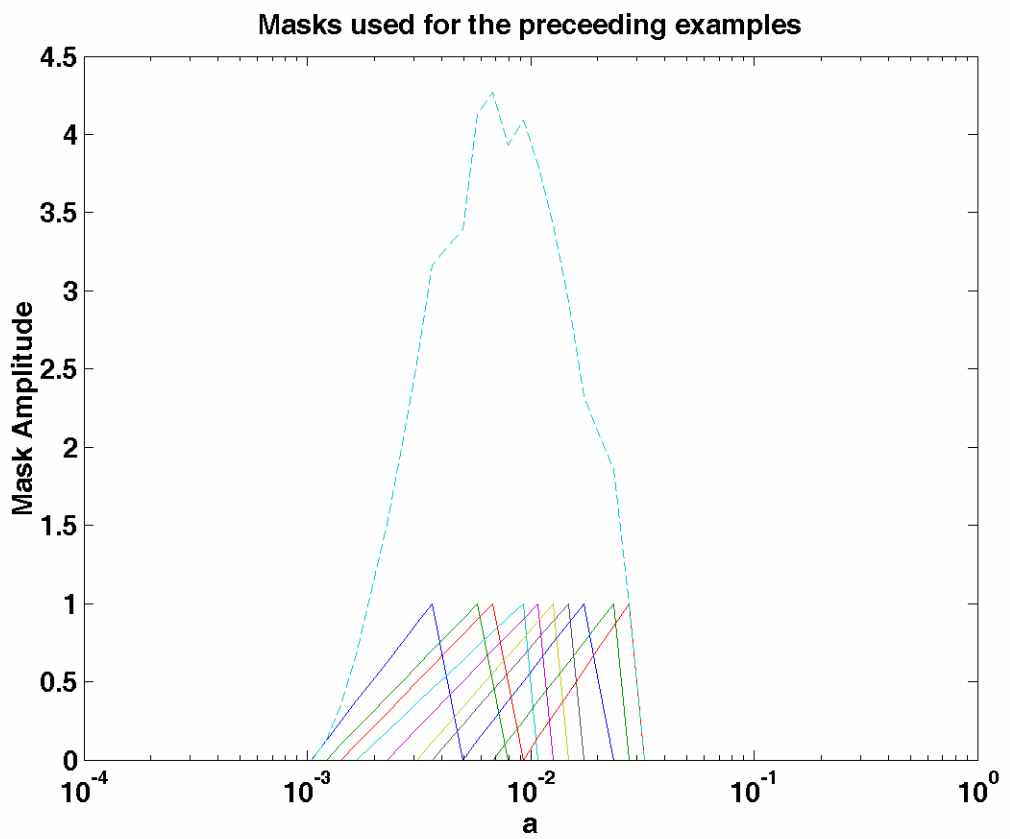


Figure 9: Mask ranges of spheres over a range of experimental parameters, summarized in Table 1. The dashed line shows the sum of all the masks, used for normalization.

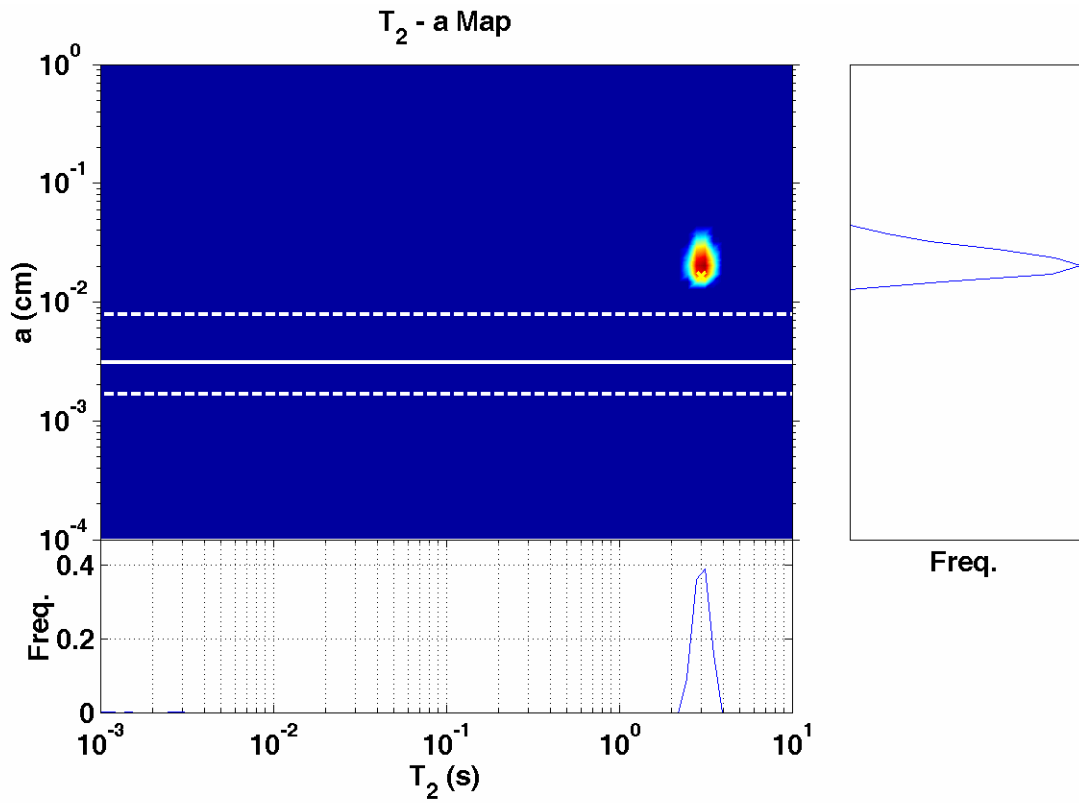


Figure 10: $a-T_2$ map for a simulated data set where the true pore size is larger than the maximum of the sensitive range of the map. The map is developed at a maximum sphere size of .008 cm, and the radius of the simulated sphere is .01 cm.

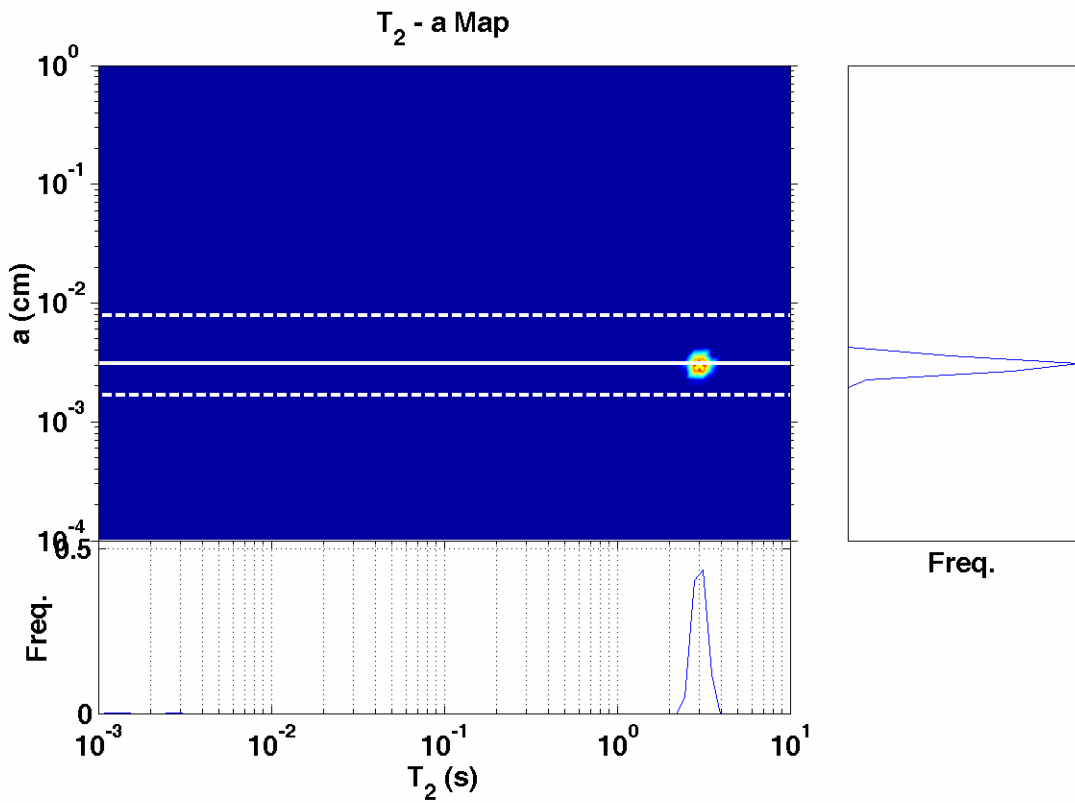


Figure 11: a - T_2 map for a simulated data set where the true pore size is within the sensitive range of the map. The map is developed maximum sphere size of .003 cm, and the radius of the simulated sphere is .003 cm.

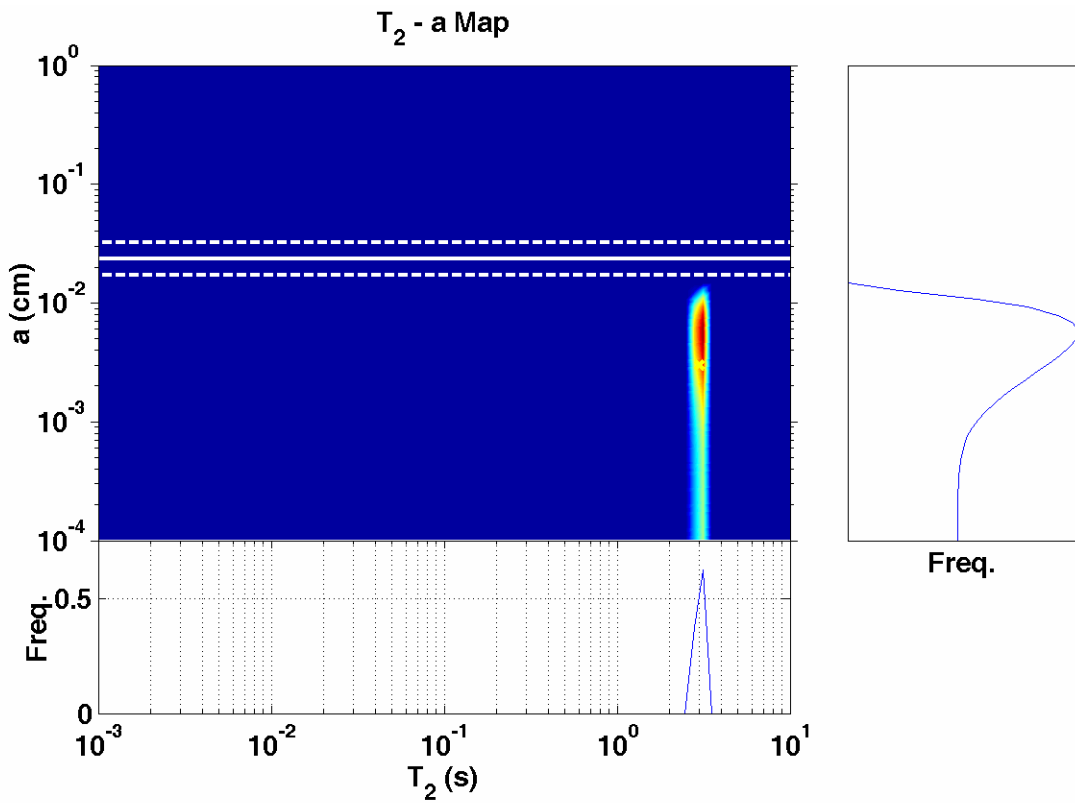


Figure 12: $a-T_2$ map for a simulated data set where the true pore size is smaller than the minimum of the sensitive range of the map. The map is developed at a minimum sphere size of 0.025 cm, and the radius of the simulated sphere is .003 cm.

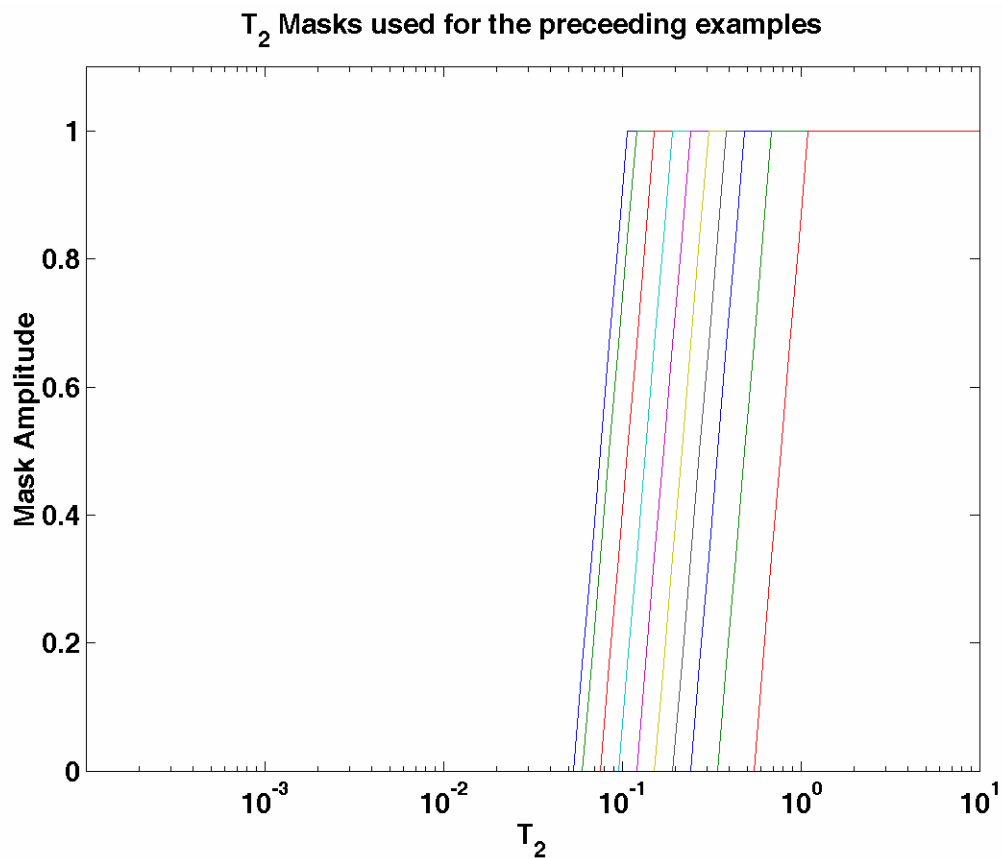


Figure 13: T_2 Masks for the data set described in Table 1.

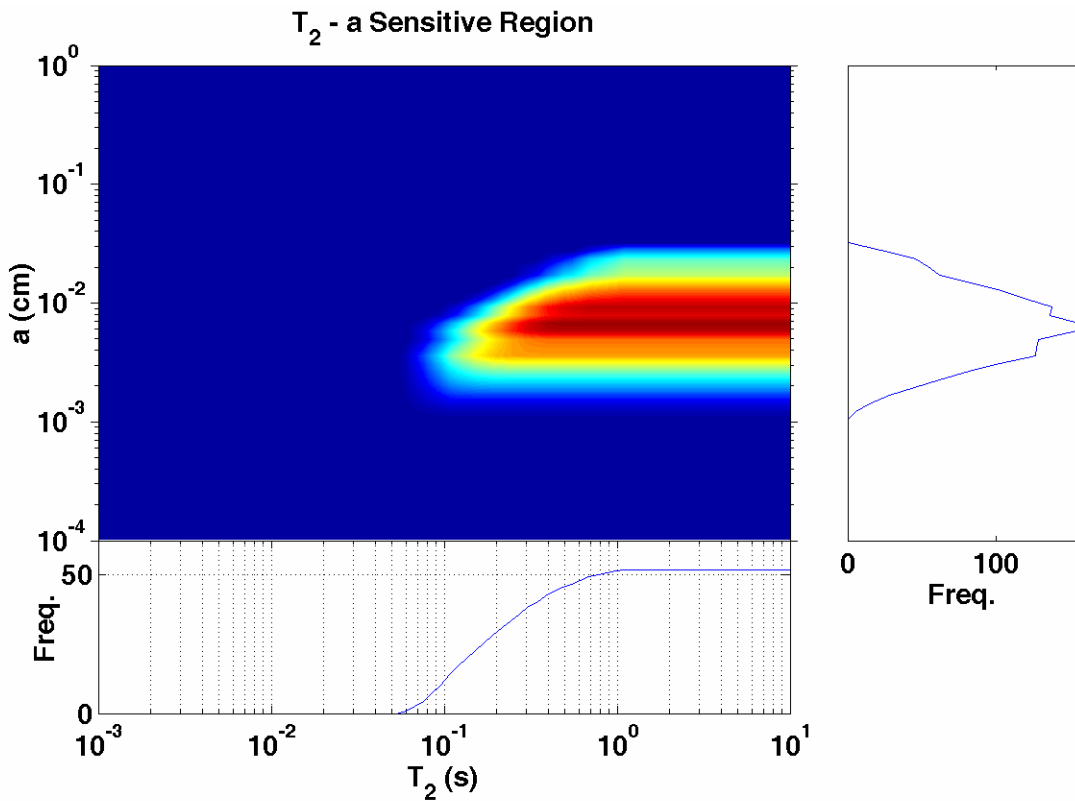


Figure 14: Sensitive range of spheres over a range of experimental parameters, summarized in Table 1.

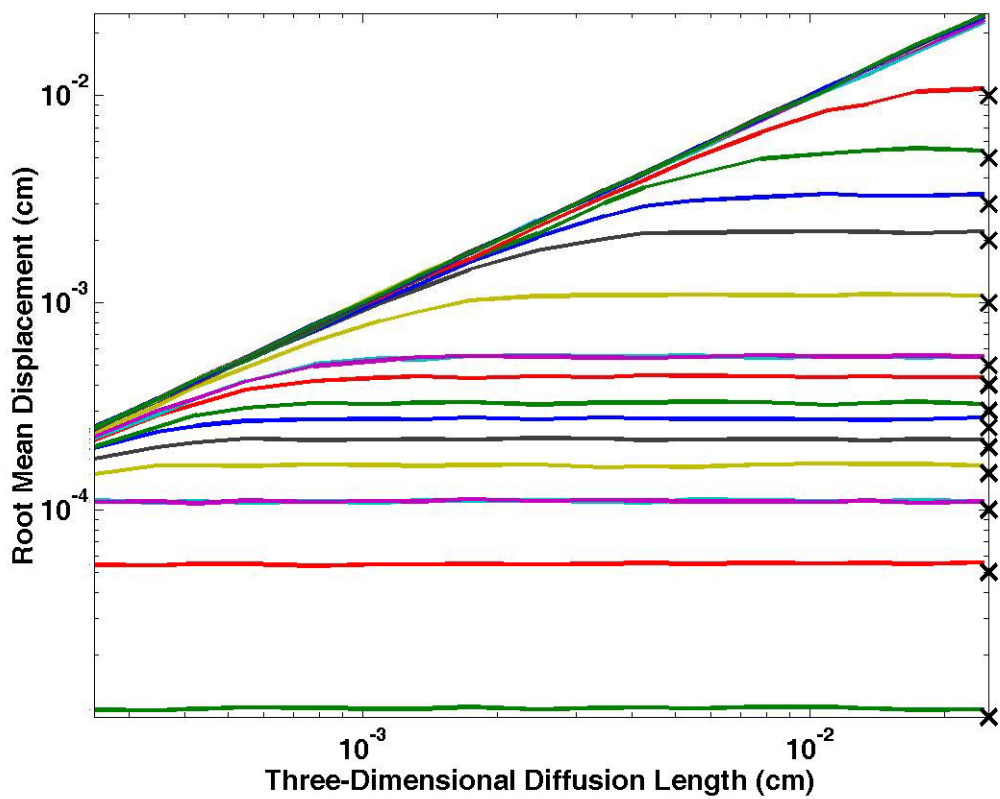


Figure 15: Simulation results for diffusion inside spheres. X indicates sphere radius in arbitrary units of length.

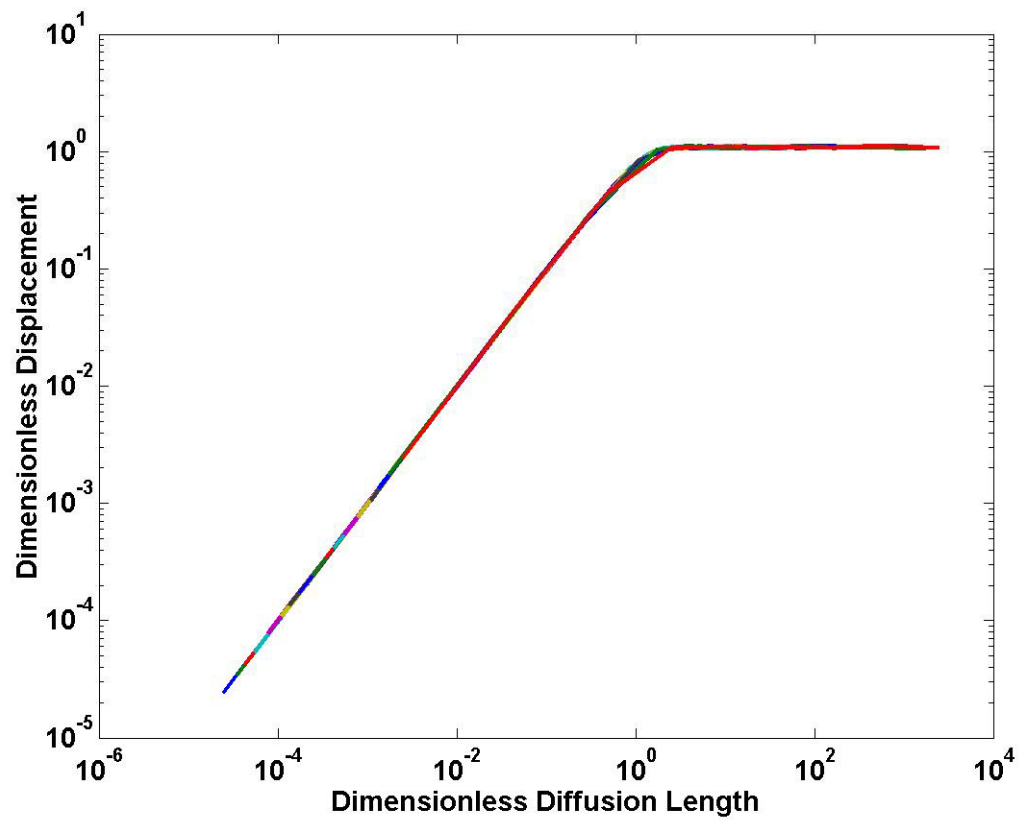


Figure 16: Dimensionless simulation results. Both dimensionless displacement and dimensionless diffusion length were made dimensionless by the sphere radius.

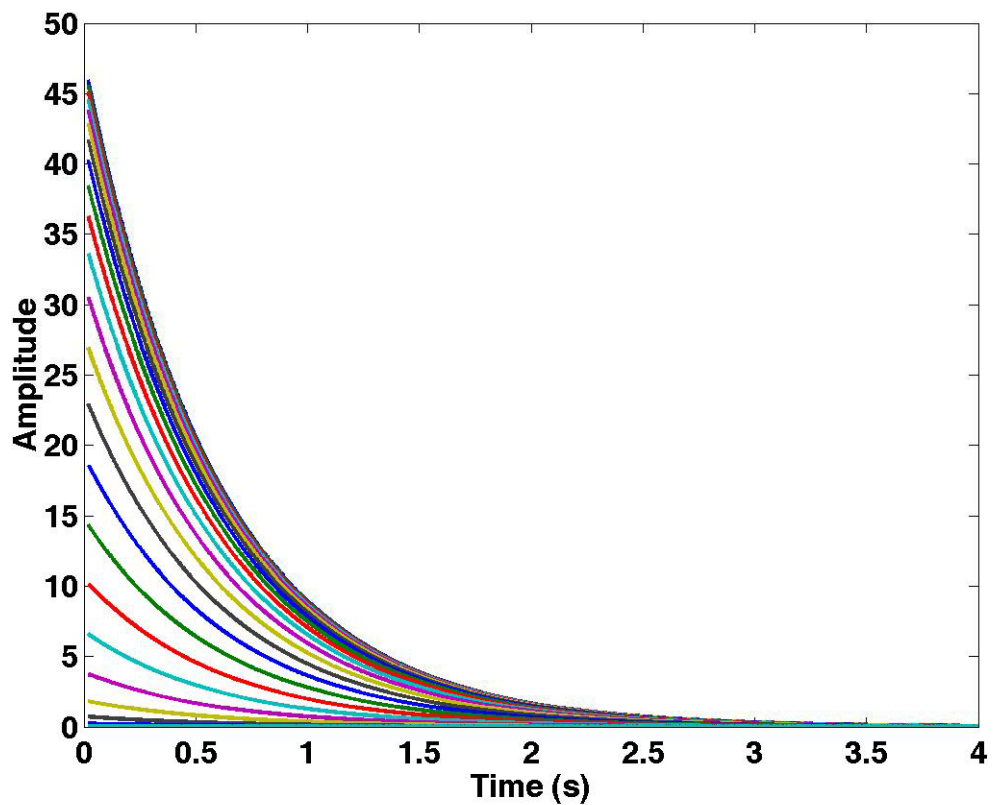


Figure 17: Raw data from a suite of PFG-SE DE measurements. Δ is 5.6 ms, δ is 1.5 ms, and the diffusivity is 6.8×10^{-4} cm²/s. The gradient strengths range from 1.6 g/cm for the top curve to 35.4 g/cm for the bottom curve. There are 4000 echoes with an echo spacing of 1 ms.

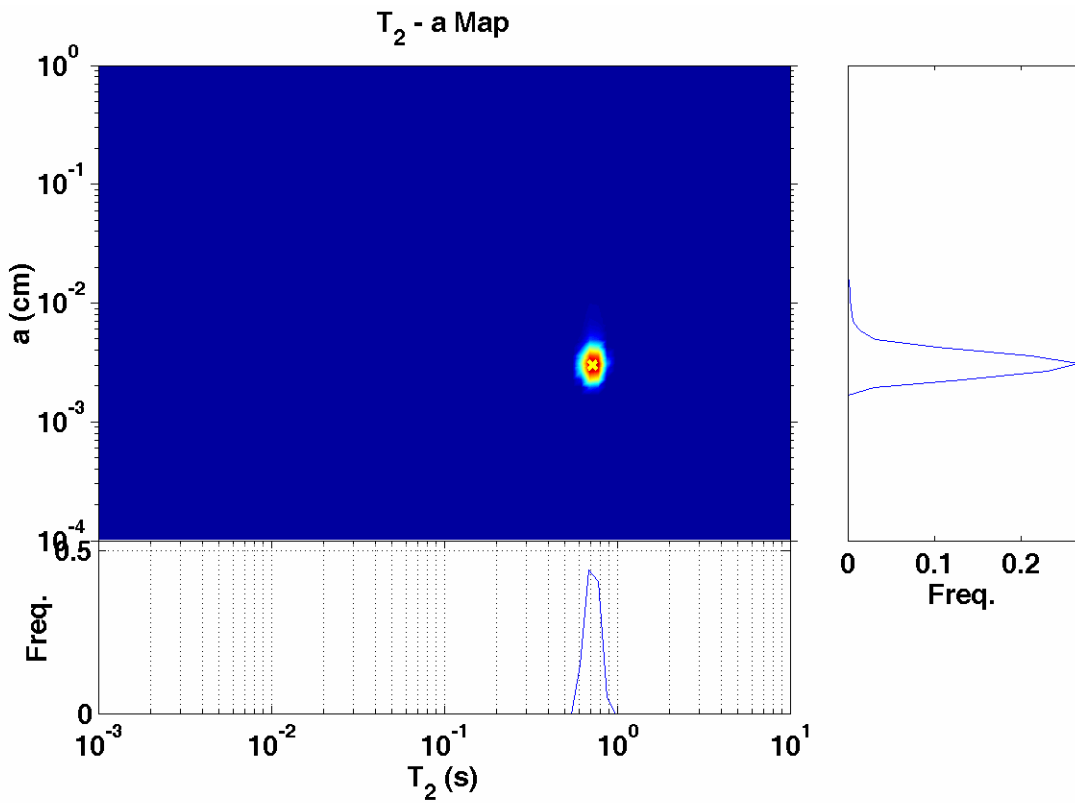


Figure 18: Summary map of pore size and relaxation information for simulated NMR data in a system of one sphere size. The x indicates the sphere size and relaxation time associated with the sphere. NMR parameters for this simulation are summarized in Table 1. The radius of the sphere in this simulation was 0.003 cm, with an associated T_2 of 720 ms.

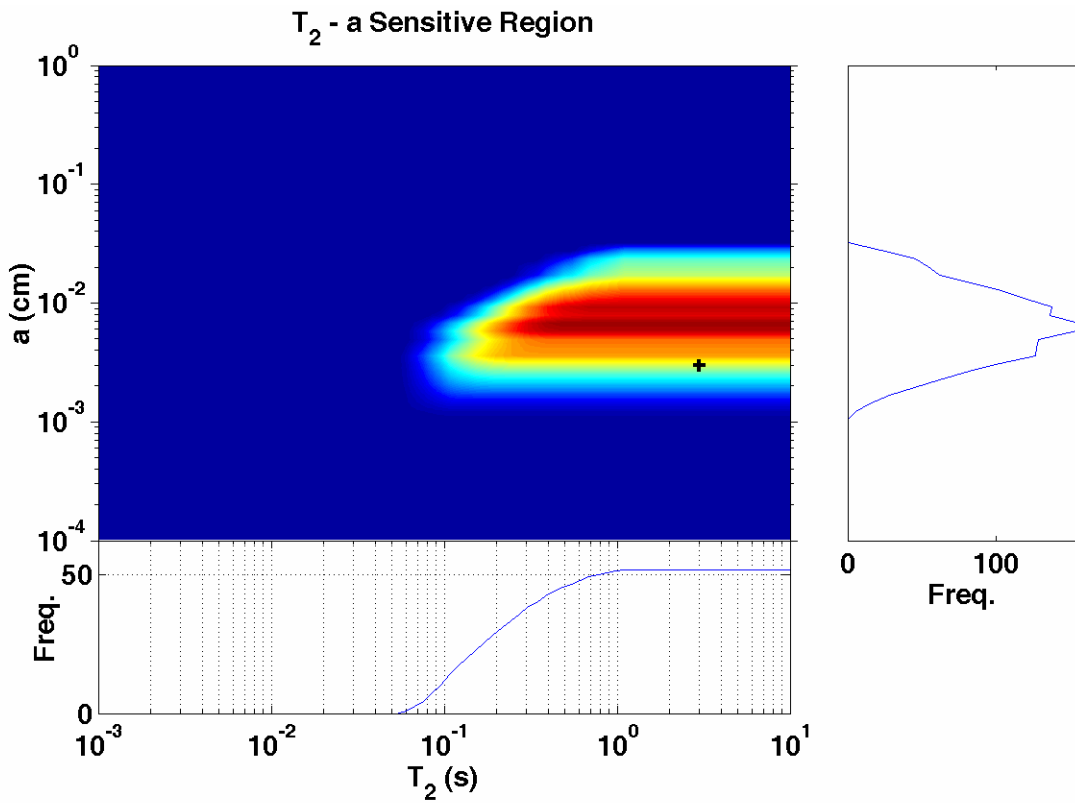


Figure 19: Sensitive range of spheres over a range of experimental parameters, summarized in Table 1. The black cross indicates the sphere size and relaxation time associated with the sphere simulated in Figure 17.

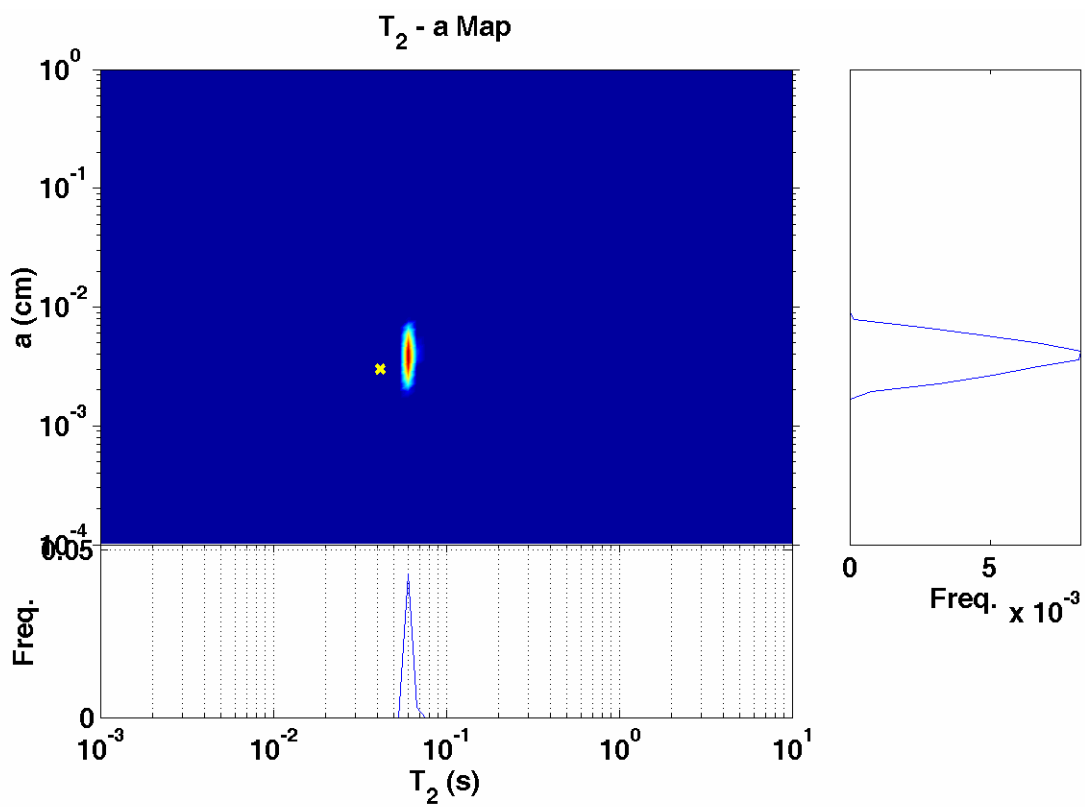


Figure 20: Summary map of pore size and relaxation information for simulated NMR data in a system of one sphere size. The x indicates the sphere size and relaxation time associated with the sphere. NMR parameters for this simulation are summarized in Table 1. The radius of the sphere in this simulation was .003 cm, with an associated T_2 of 42 ms.

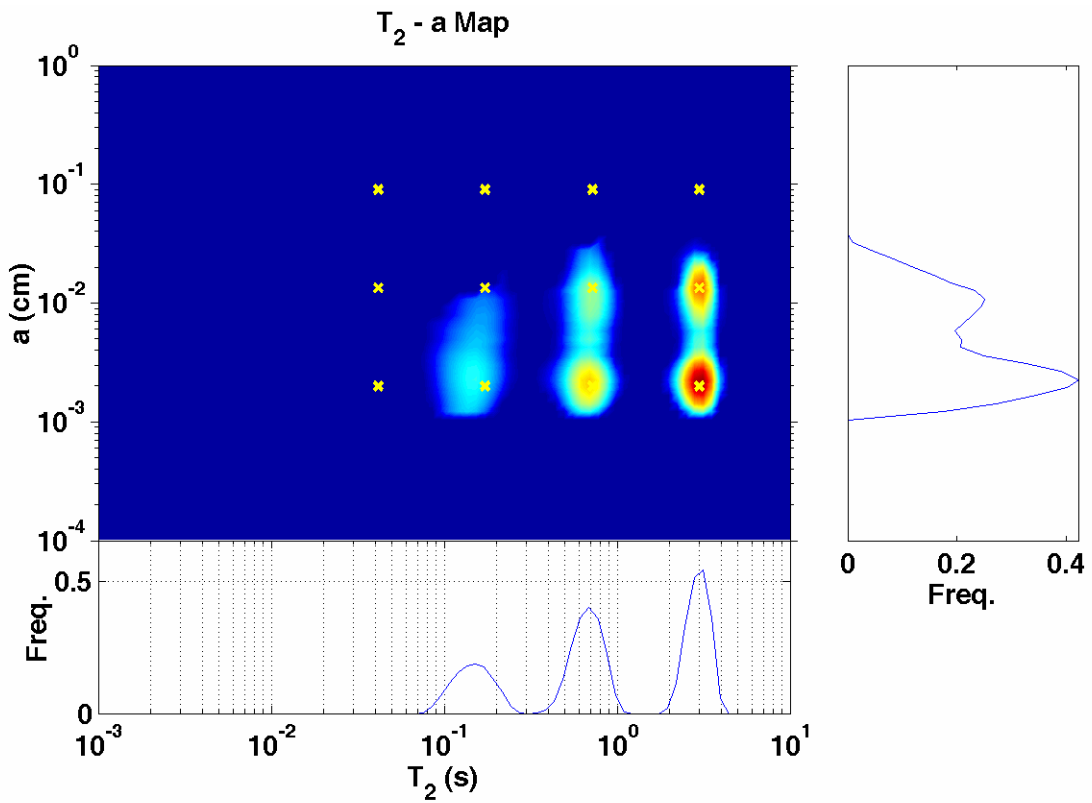


Figure 21: Summary map of pore size and relaxation information for simulated NMR data in a system of spheres. The x indicates the sphere sizes and relaxation times associated with the spheres. NMR parameters for this simulation are summarized in Table 1.

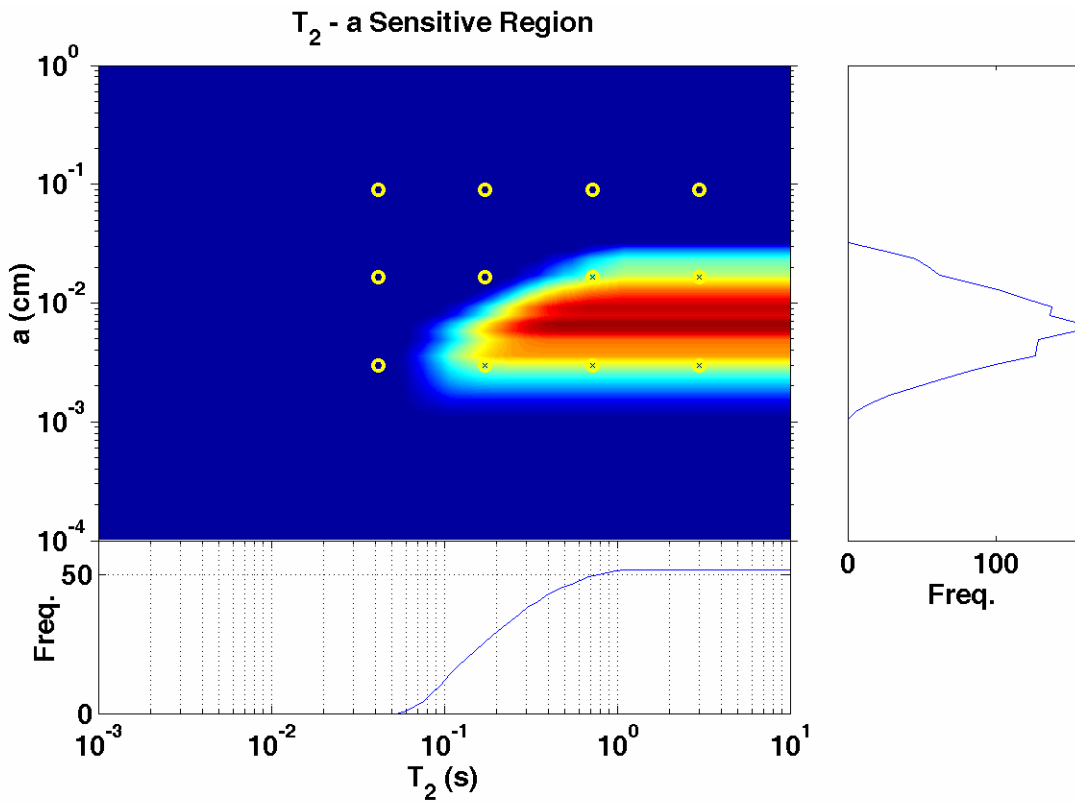


Figure 22: Summary map of pore size and relaxation information for simulated NMR data in a system of spheres. The circles indicate the sphere sizes and relaxation times associated with the spheres. NMR parameters for this simulation are summarized in Table 1.

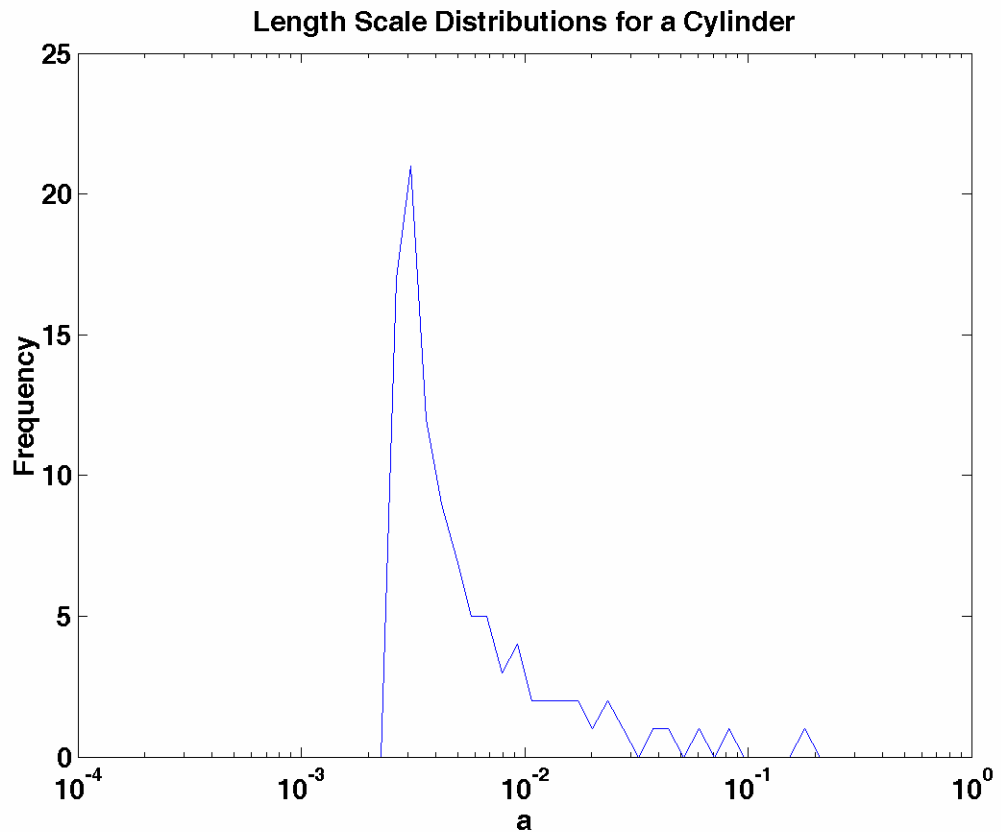


Figure 23: Distribution of observed length scales in a cylinder of radius 0.003 cm and 100 orientations between 0 and 2π radians.

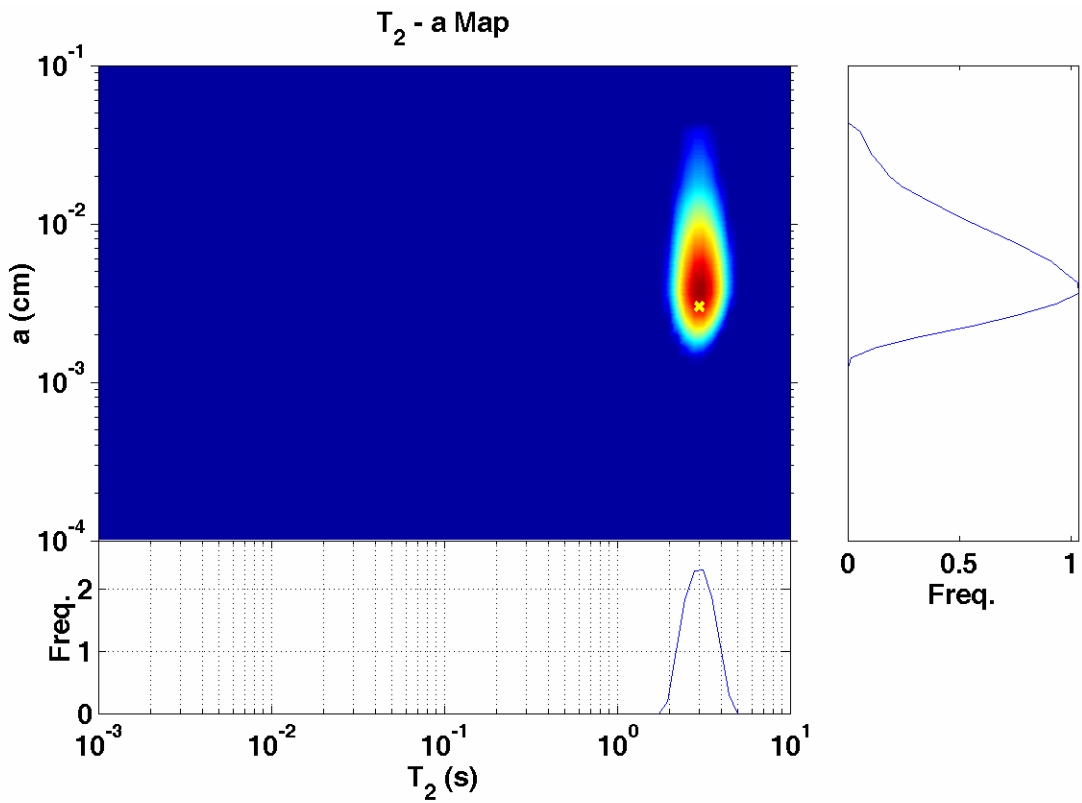


Figure 24: Summary map of pore size and relaxation information for simulated NMR data in a system of one cylinder size. The x indicates the sphere size and relaxation time associated with the sphere. NMR parameters for this simulation are summarized in Table 1. The radius of the cylinder in this simulation was 0.003 cm, with an associated T_2 of 3 s.

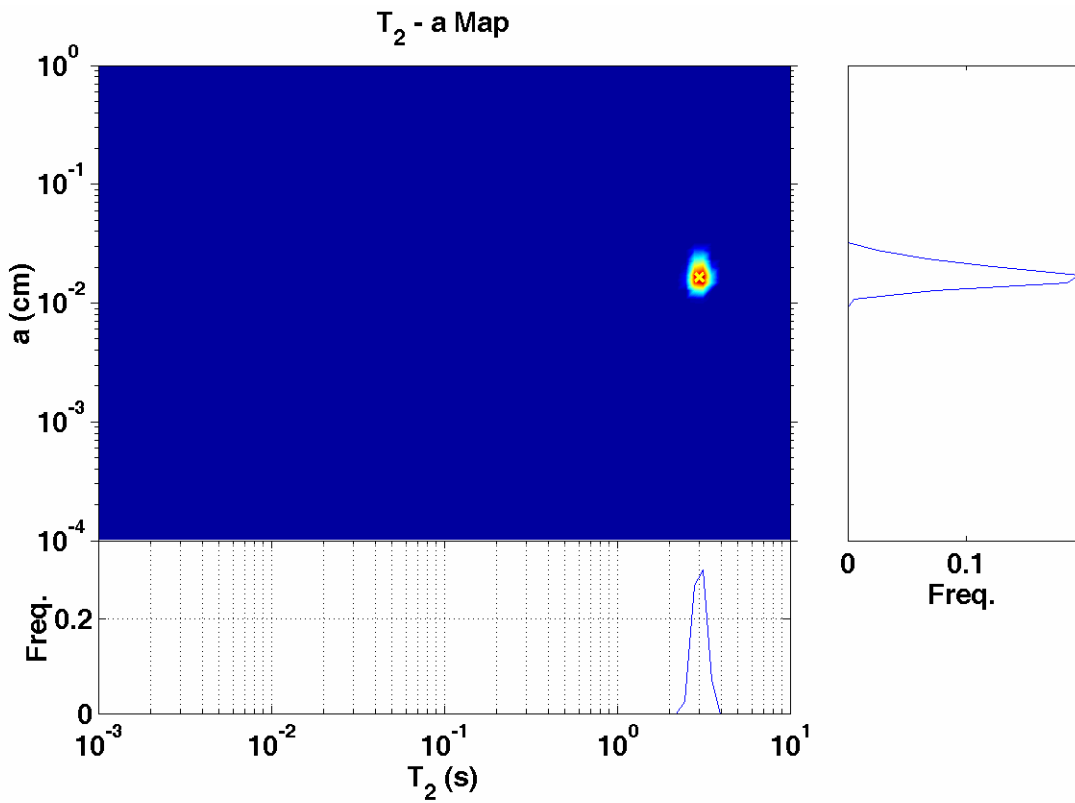


Figure 25: Summary map of pore size and relaxation information for simulated NMR data in a system of one sphere size from which the amplitude was only 67% recovered. This set was collected with mast cut-off of 45% of peak square difference in sphere amplitudes. The x indicates the sphere size and relaxation time associated with the sphere. NMR parameters for this simulation are summarized in Table 1. The radius of the sphere in this simulation was 0.016 cm, with an associated T_2 of 3.0 s.

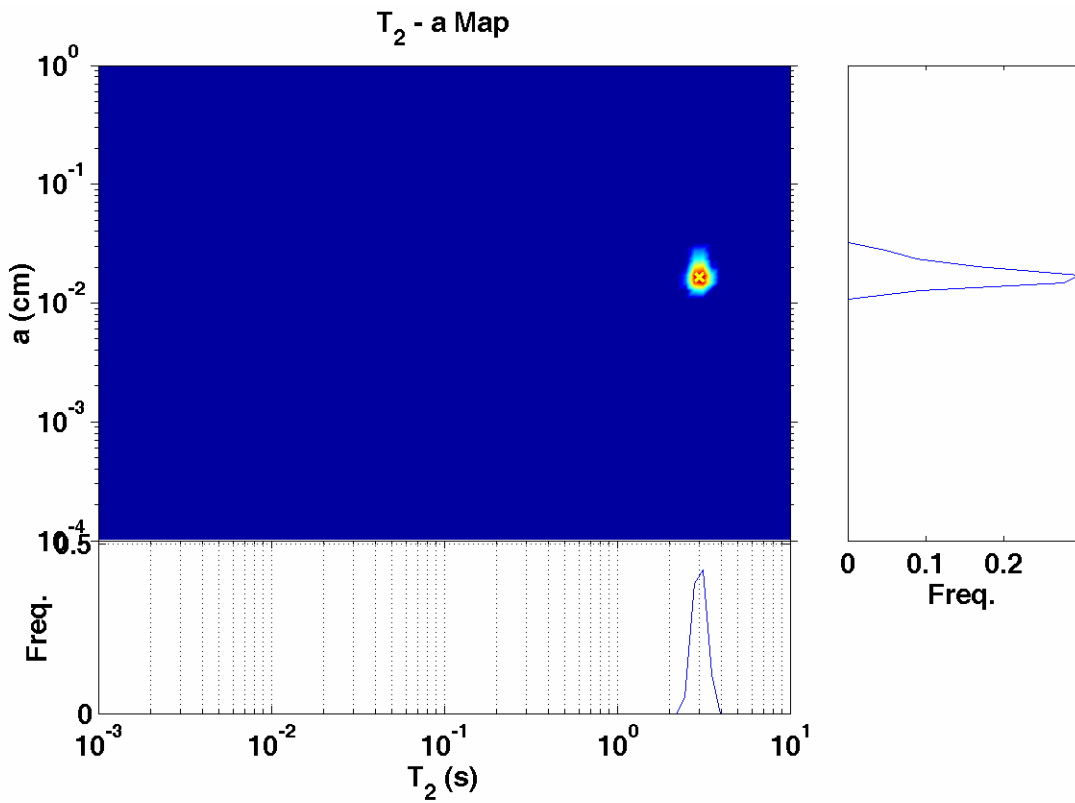


Figure 26: Summary map of pore size and relaxation information for simulated NMR data in a system of one sphere size from which the amplitude was 95% recovered. This set was collected with mast cut-off of 98% of peak square difference in sphere amplitudes. The x indicates the sphere size and relaxation time associated with the sphere. NMR parameters for this simulation are summarized in Table 1. The radius of the sphere in this simulation was 0.016 cm, with an associated T_2 of 3.0 s.

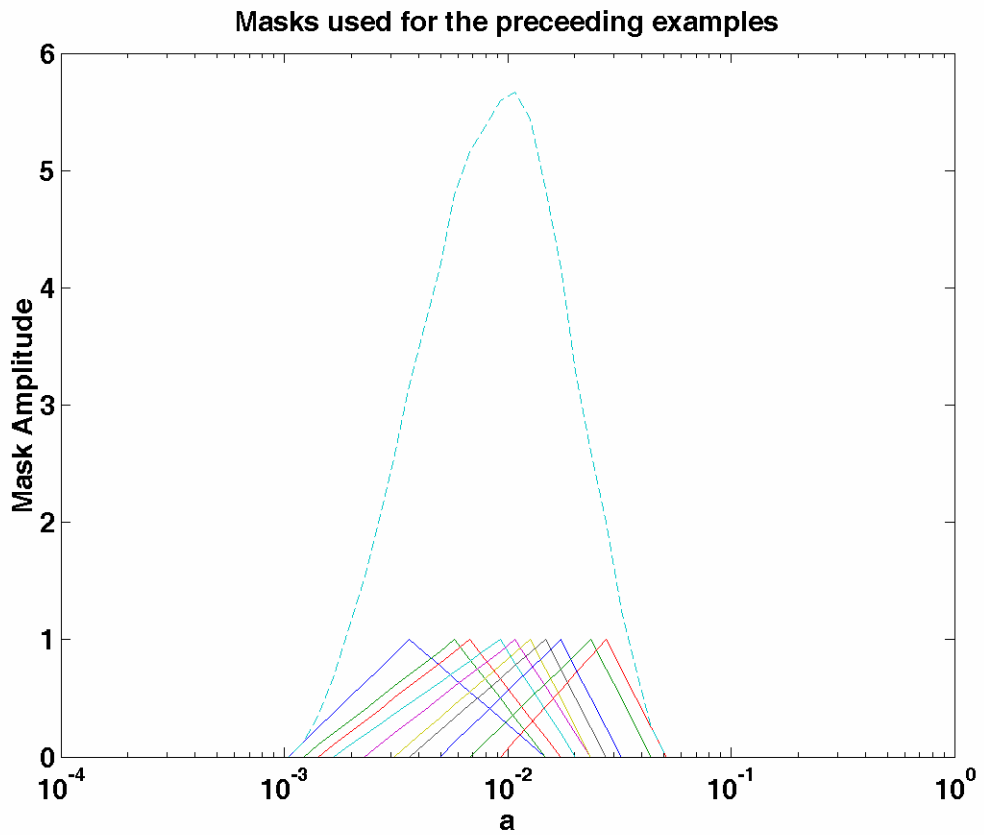


Figure 27: Mask ranges of spheres over a range of experimental parameters, summarized in Table 1. These masks were generated with a cut-off of 45% of peak square difference in sphere amplitudes.

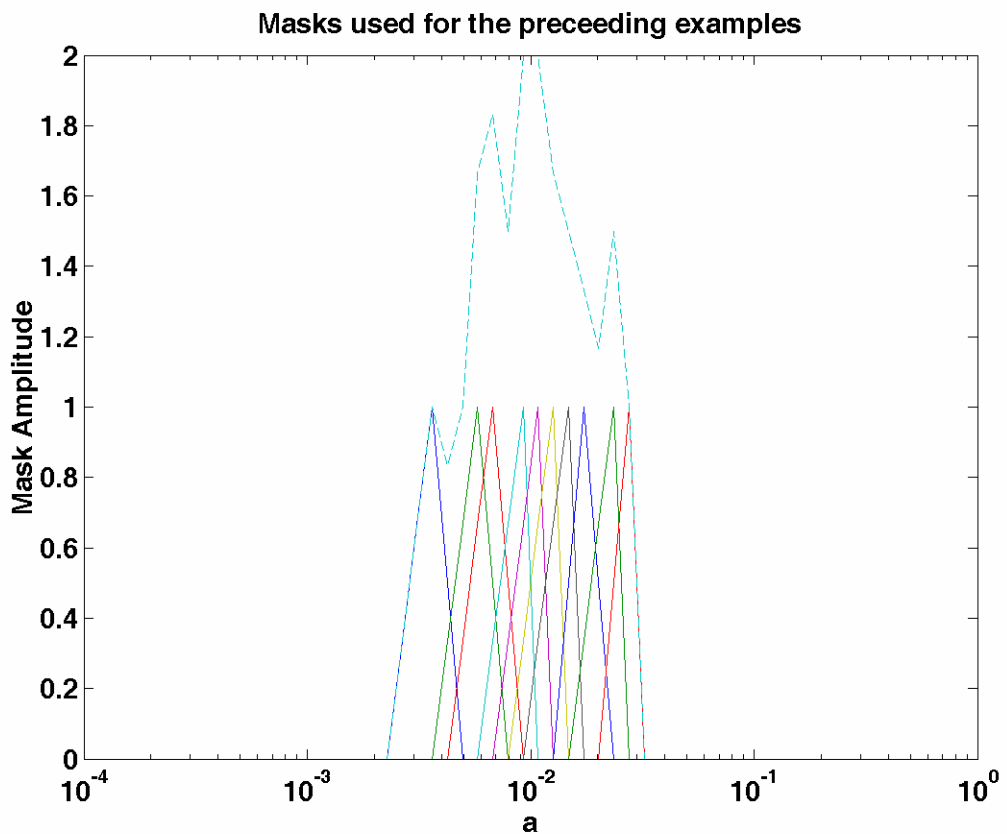


Figure 28: Mask ranges of spheres over a range of experimental parameters, summarized in Table 1. These masks were generated with a cut-off of 95% of peak square difference in sphere amplitudes.

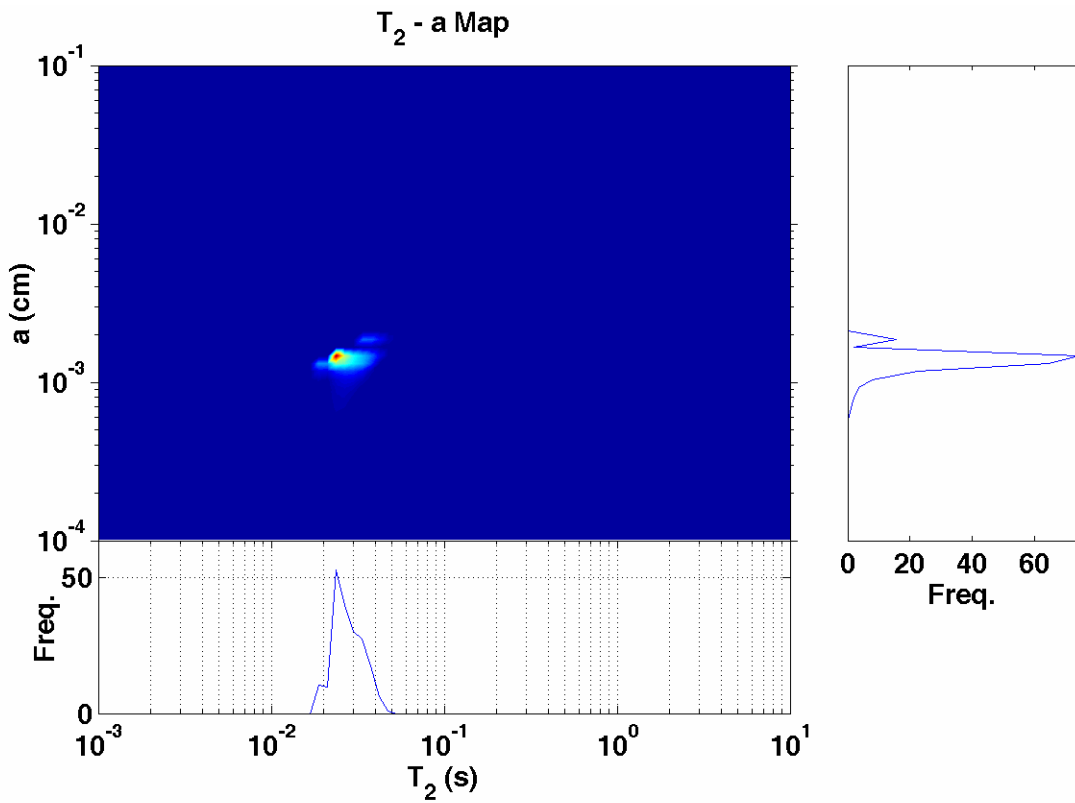


Figure 29: Summary map for dolomite grain pack saturated with water. The grain sizes are 100 to 150 microns.

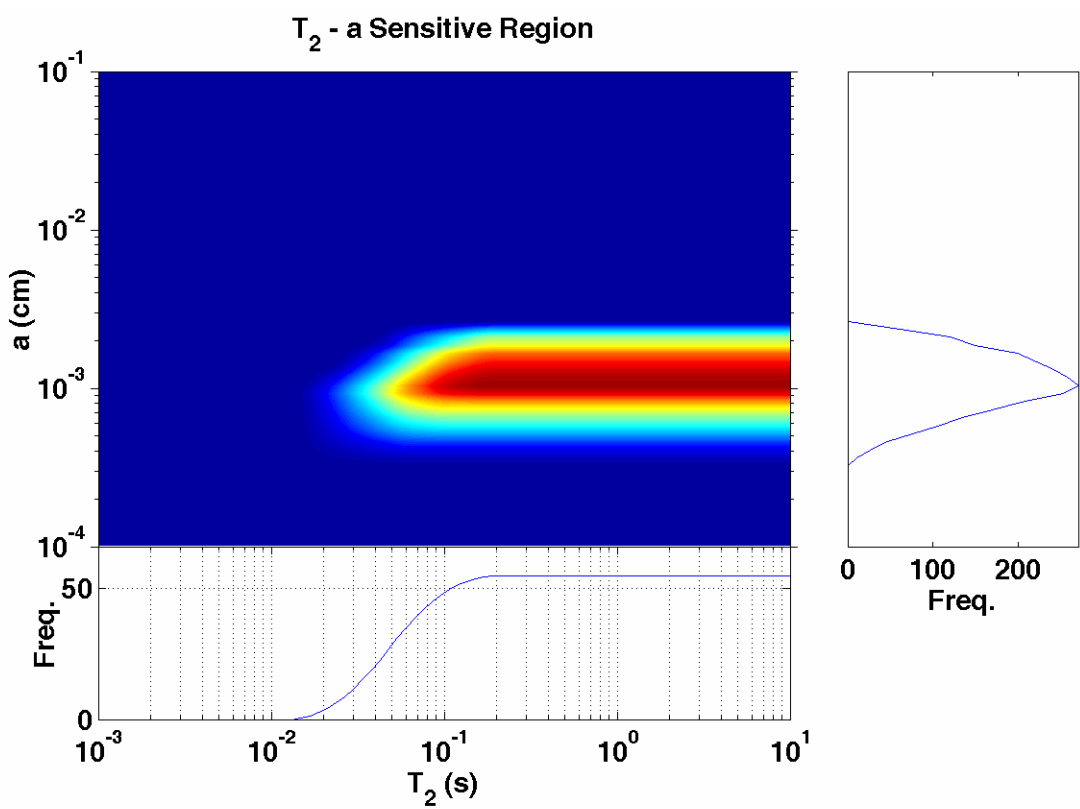


Figure 30: Sensitive range for water saturating dolomite grains.

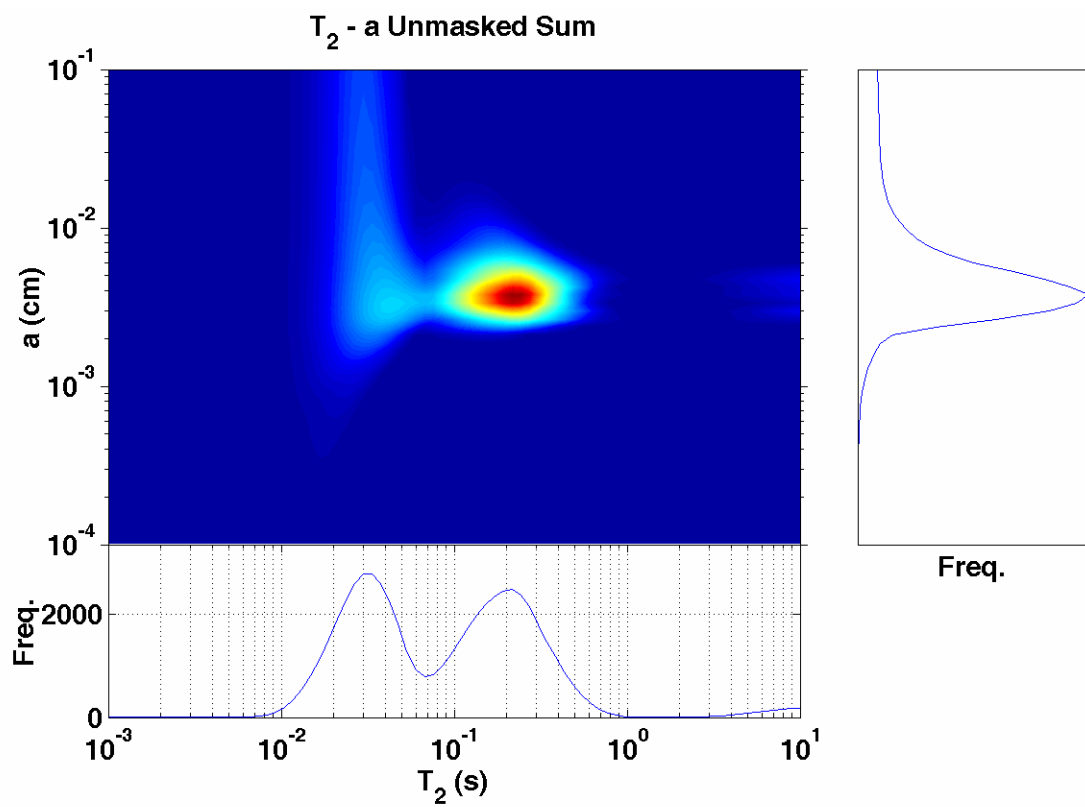


Figure 31: Unmasked sum for dolomite grain pack saturated with water. The grain sizes are 100 to 150 microns

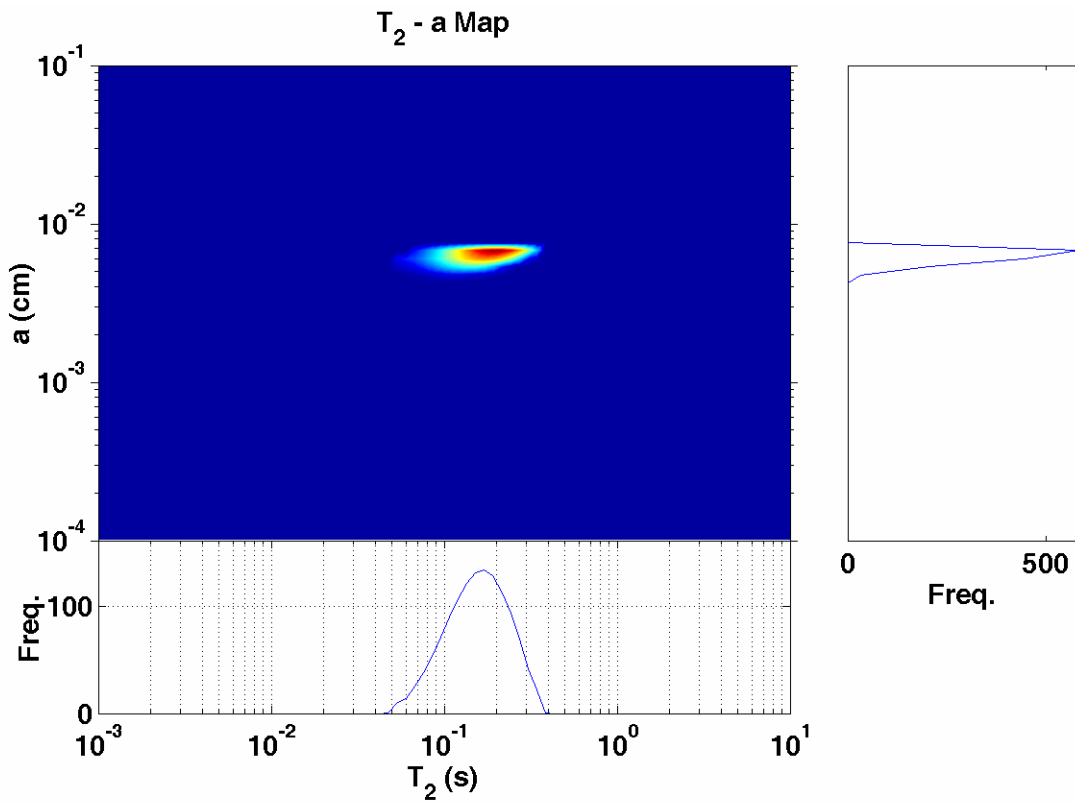


Figure 32: Summary map for dolomite grain pack saturated with pentane. The grain sizes are 100 to 150 microns.

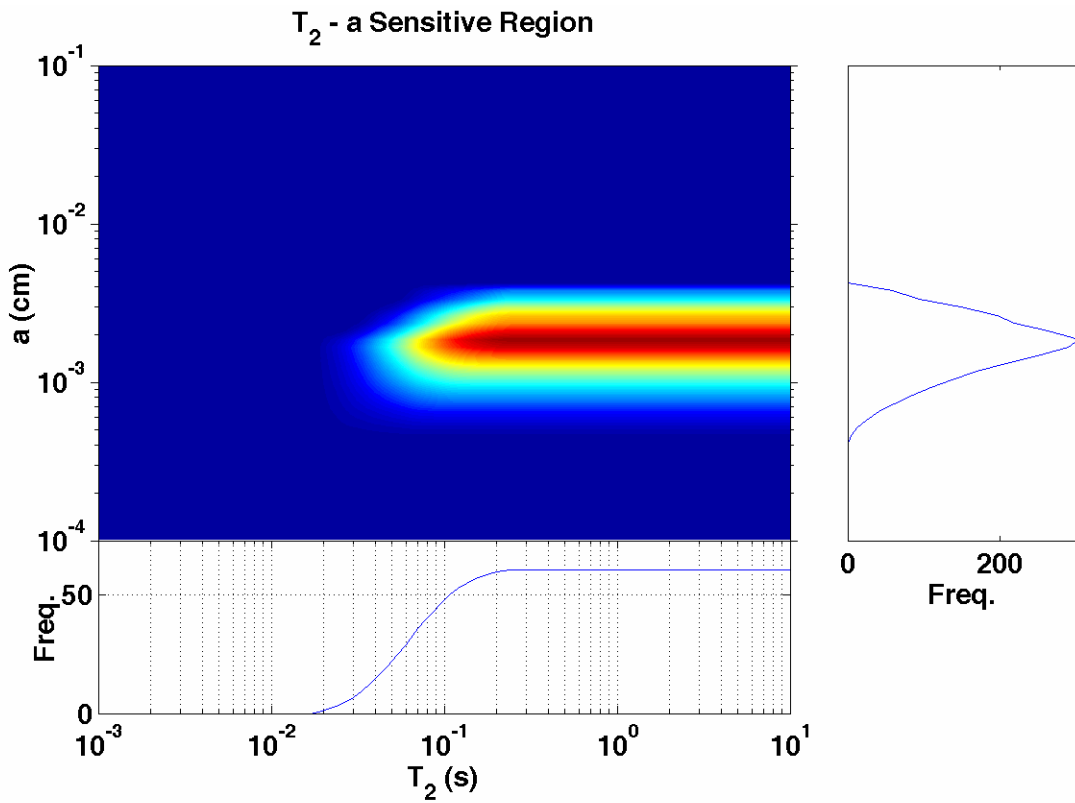


Figure 33: Sensitive range for pentane saturating dolomite grains.

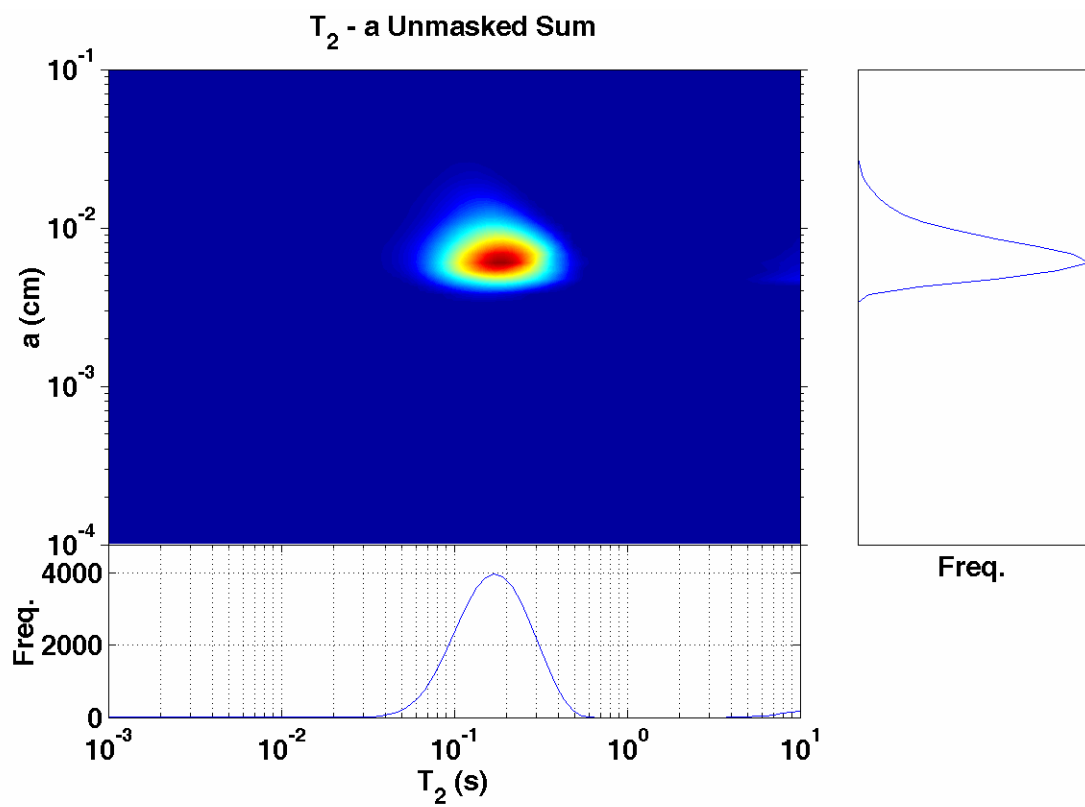


Figure 34: Unmasked sum for dolomite grain pack saturated with pentane. The grain sizes are 100 to 150 microns

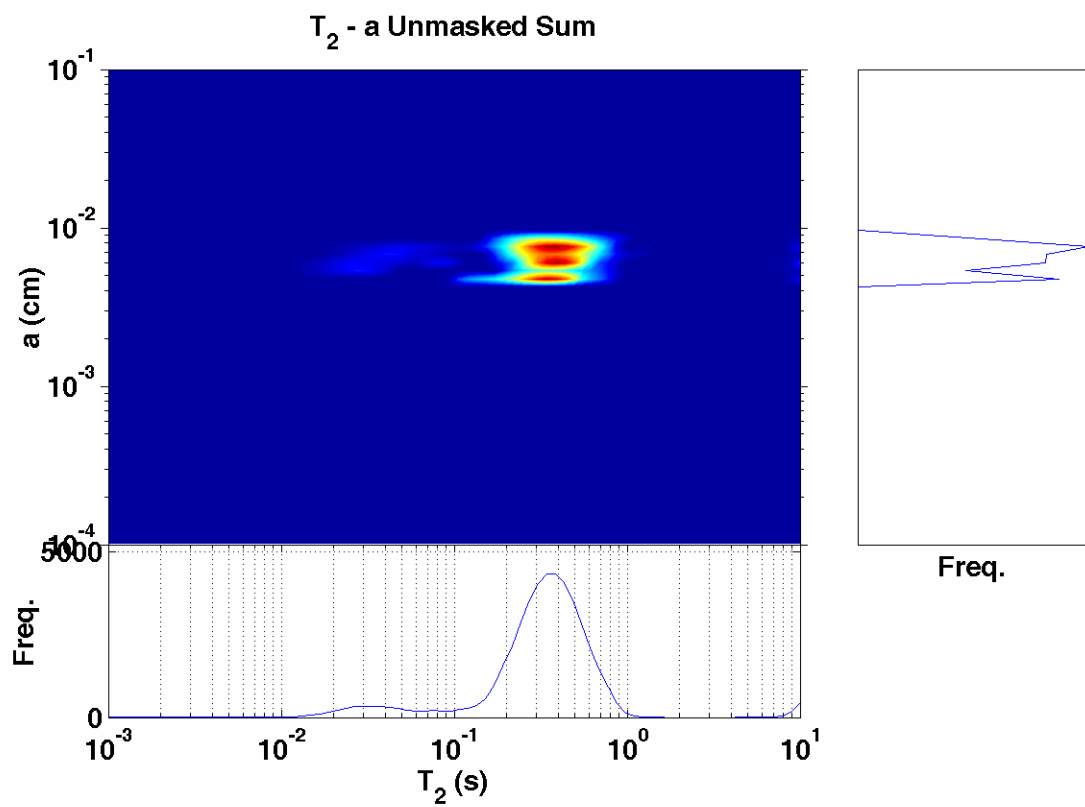


Figure 35: Unmasked sum for dolomite grain pack saturated with water. The grain sizes are 150 to 300 microns.

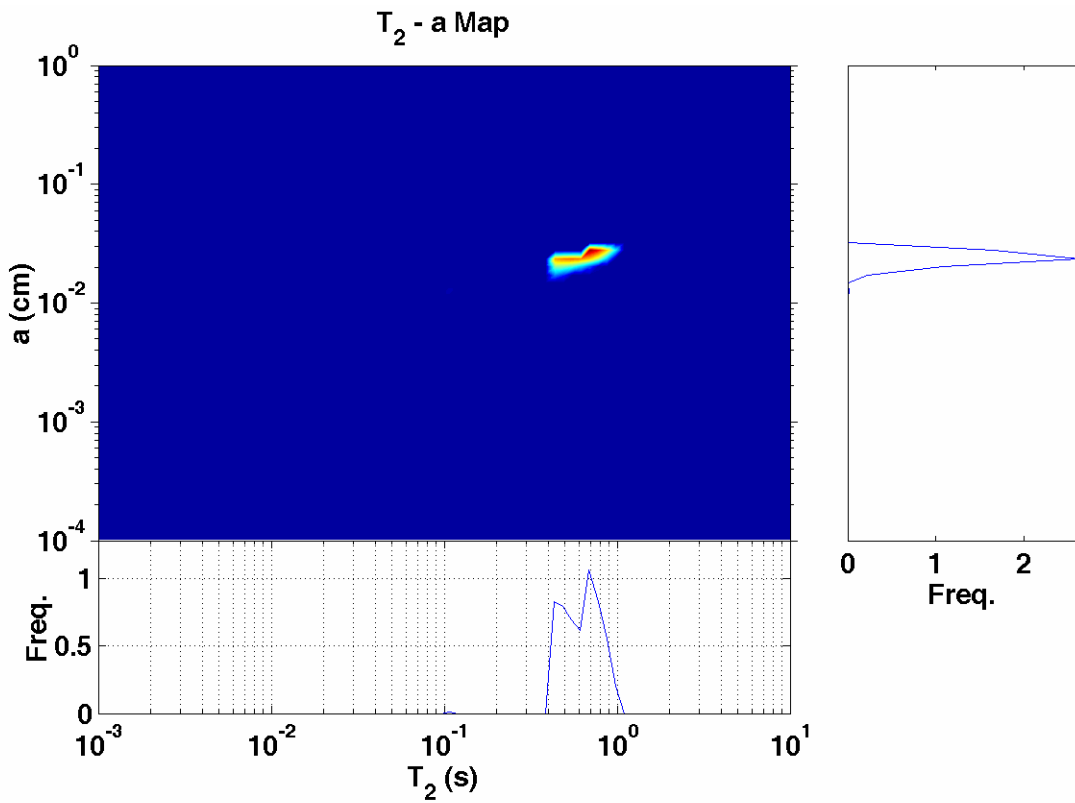


Figure 36: Summary map for carbonate sample 7b saturated with water and methane (4000 psi).

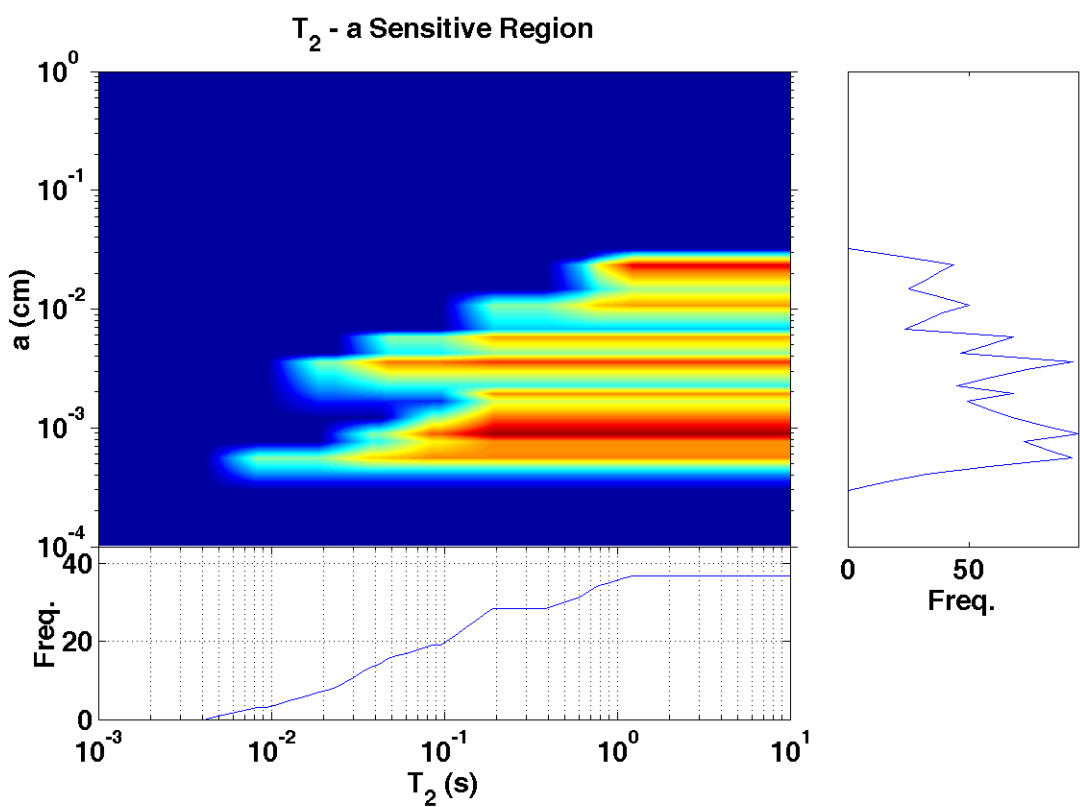


Figure 37: Sensitive region for carbonate sample 7b saturated with water and methane (4000 psi).

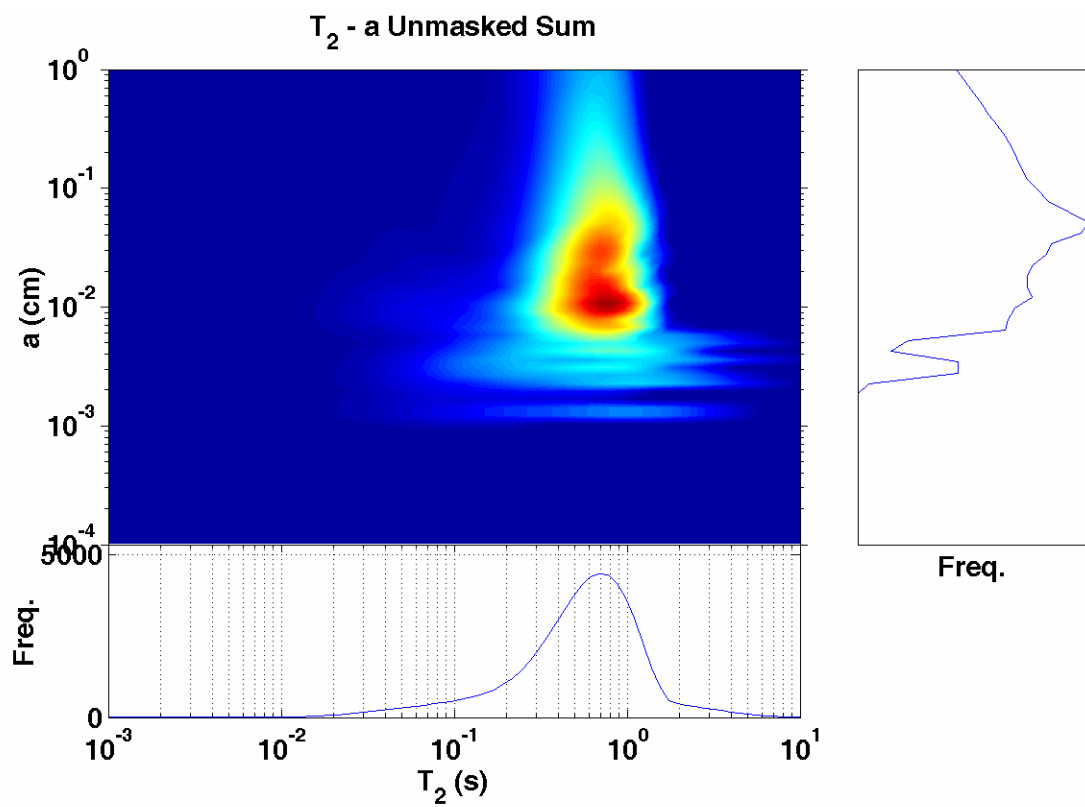


Figure 38: Unmasked sum for carbonate sample 7b saturated with water and methane (4000 psi).

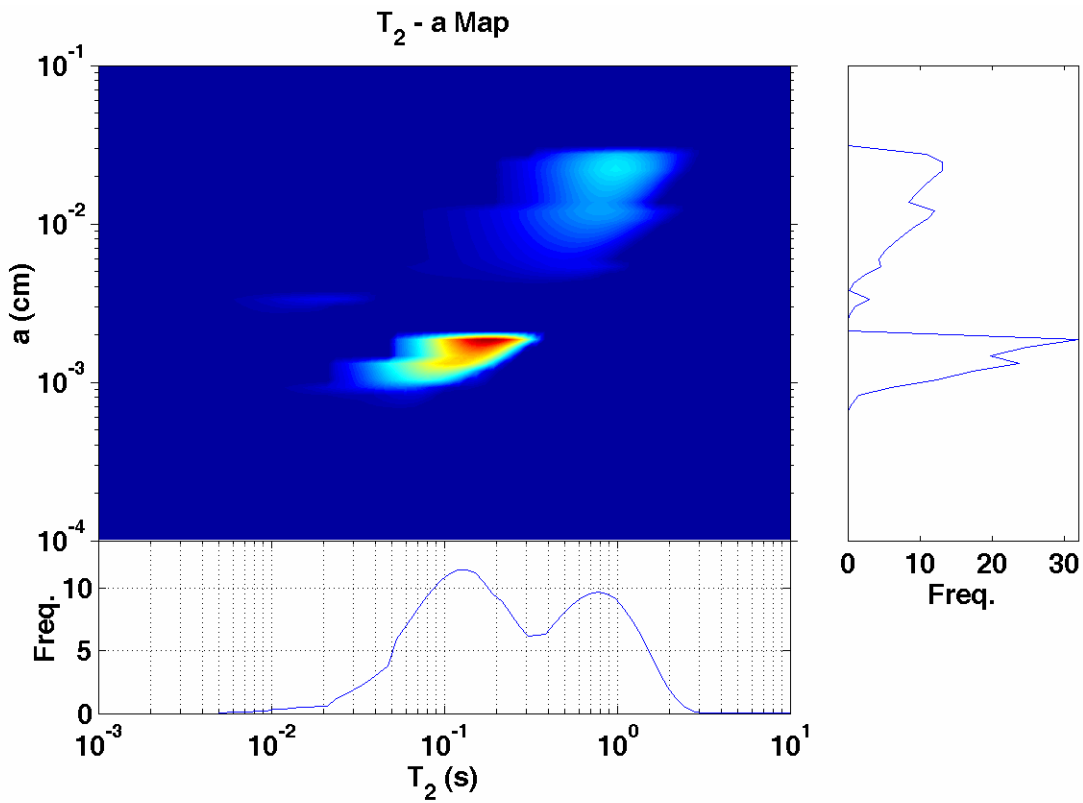


Figure 39: Summary map for carbonate sample 8a saturated with water, methane (4000 psi), and ethane (600 psi).

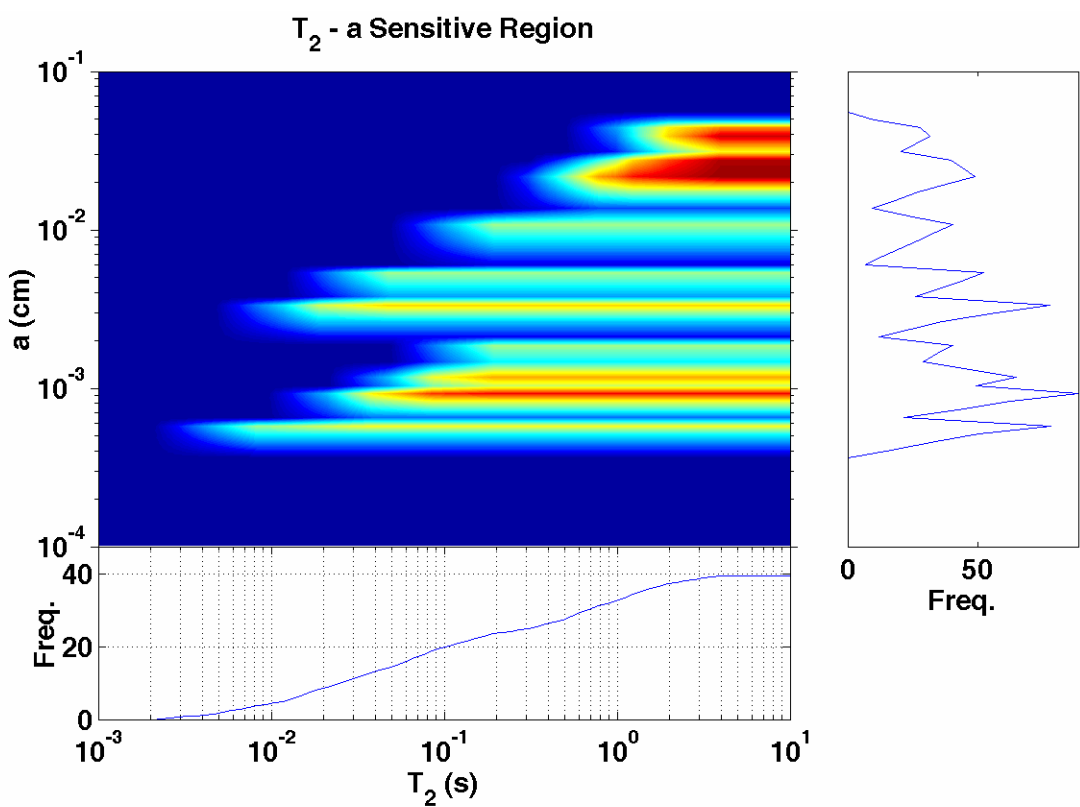


Figure 40: Sensitive region for carbonate sample 8a saturated with water, methane (4000 psi), and ethane (600 psi).

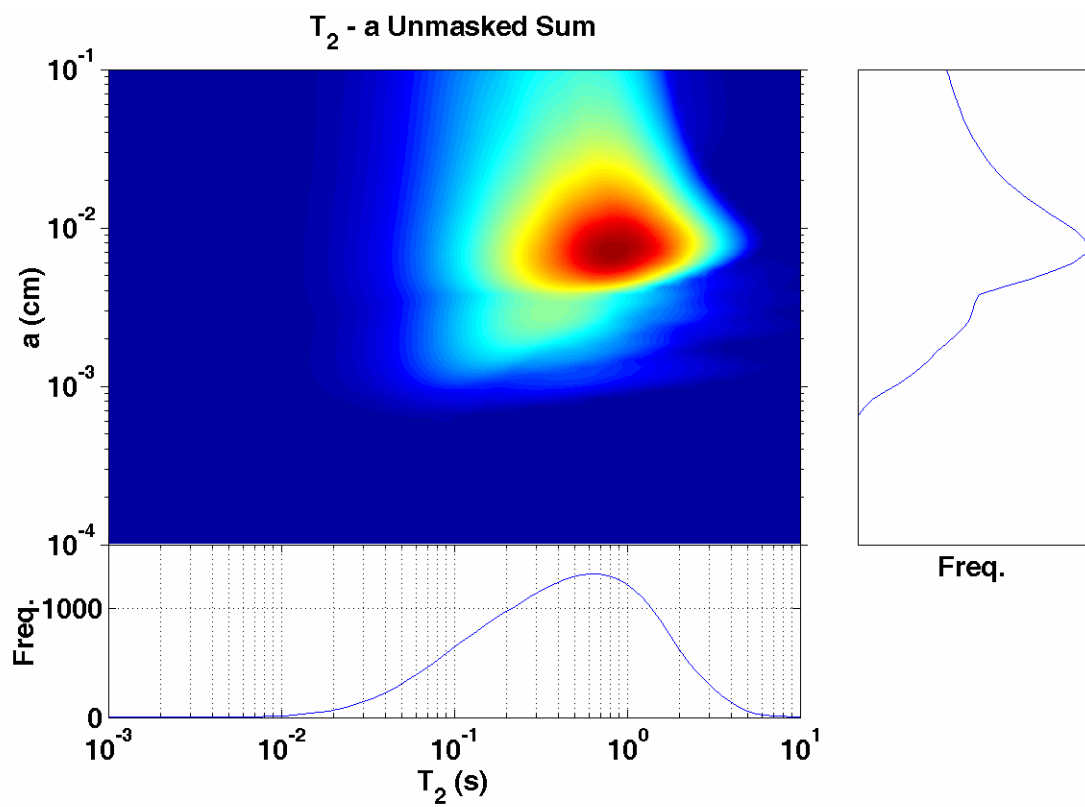


Figure 41: Unmasked sum for carbonate sample 8a saturated with water, methane (4000 psi), and ethane (600 psi).

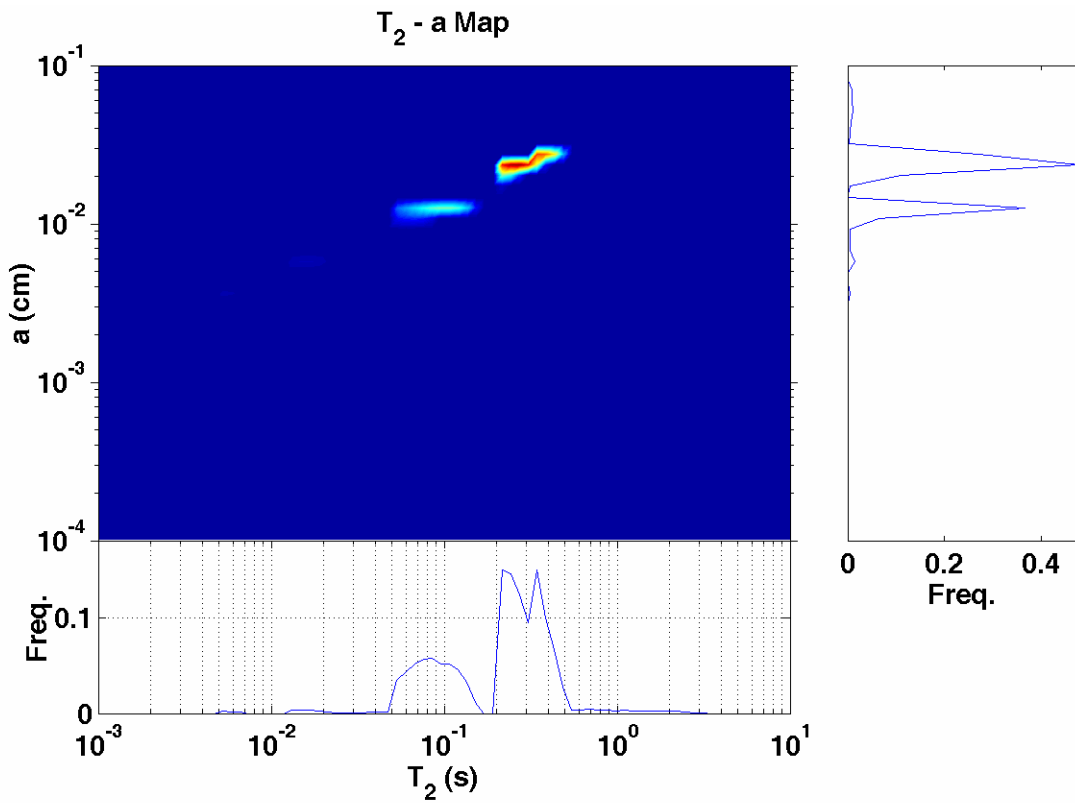


Figure 42: Summary map for carbonate sample 2433 saturated with water, methane (4000 psi), and ethane (600 psi).

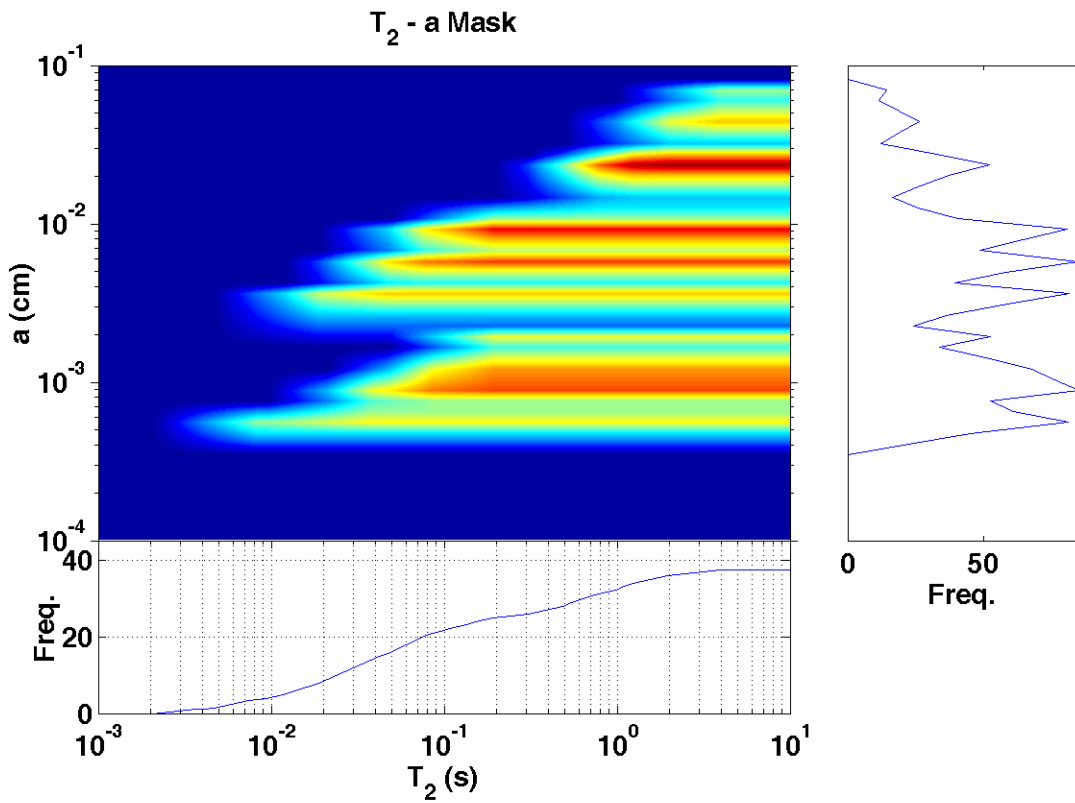


Figure 43: Sensitive range for carbonate sample 2433 saturated with water, methane (4000 psi), and ethane (600 psi).

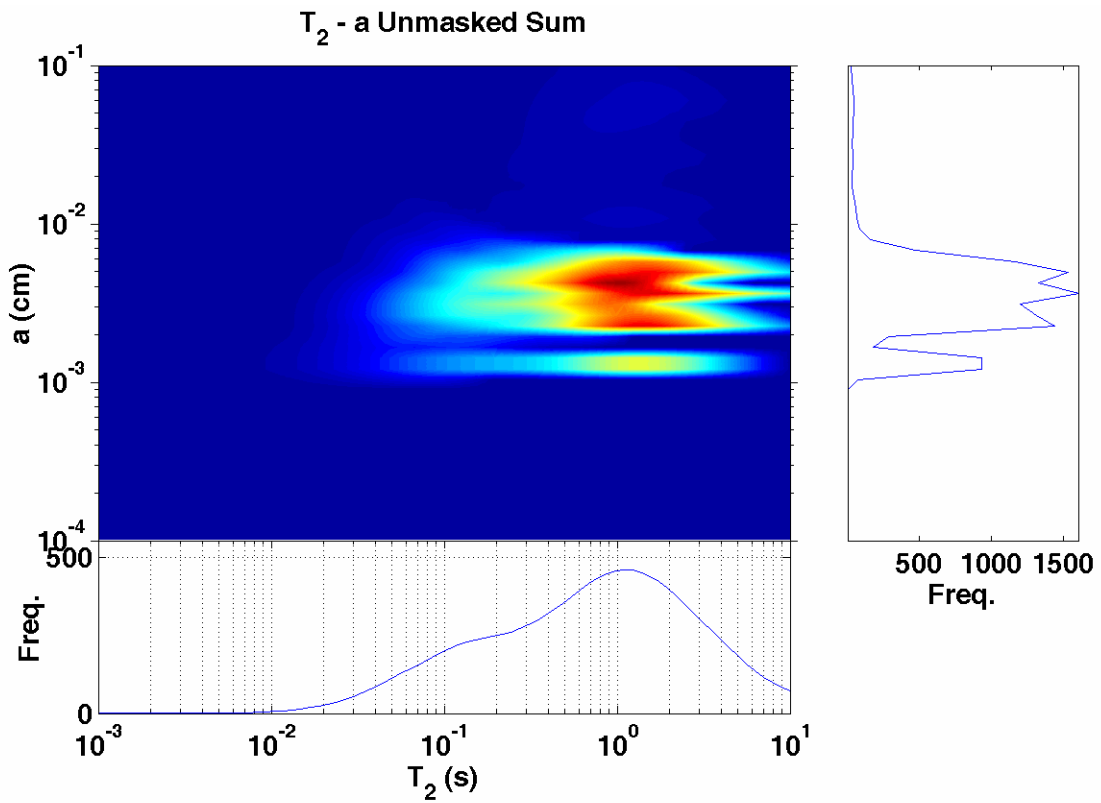


Figure 44: Unmasked sum for carbonate sample 2433 saturated with water, methane (4000 psi), and ethane (600 psi).

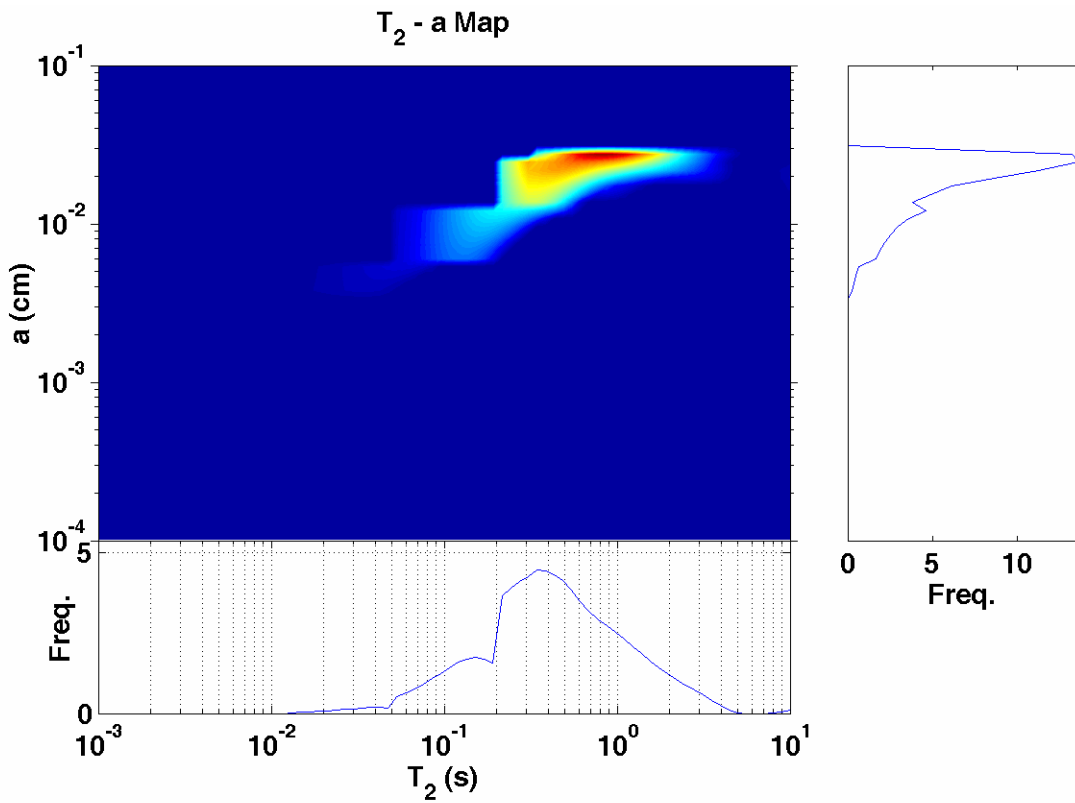


Figure 45: Summary map for carbonate sample 1315 saturated with water and methane (4000 psi).

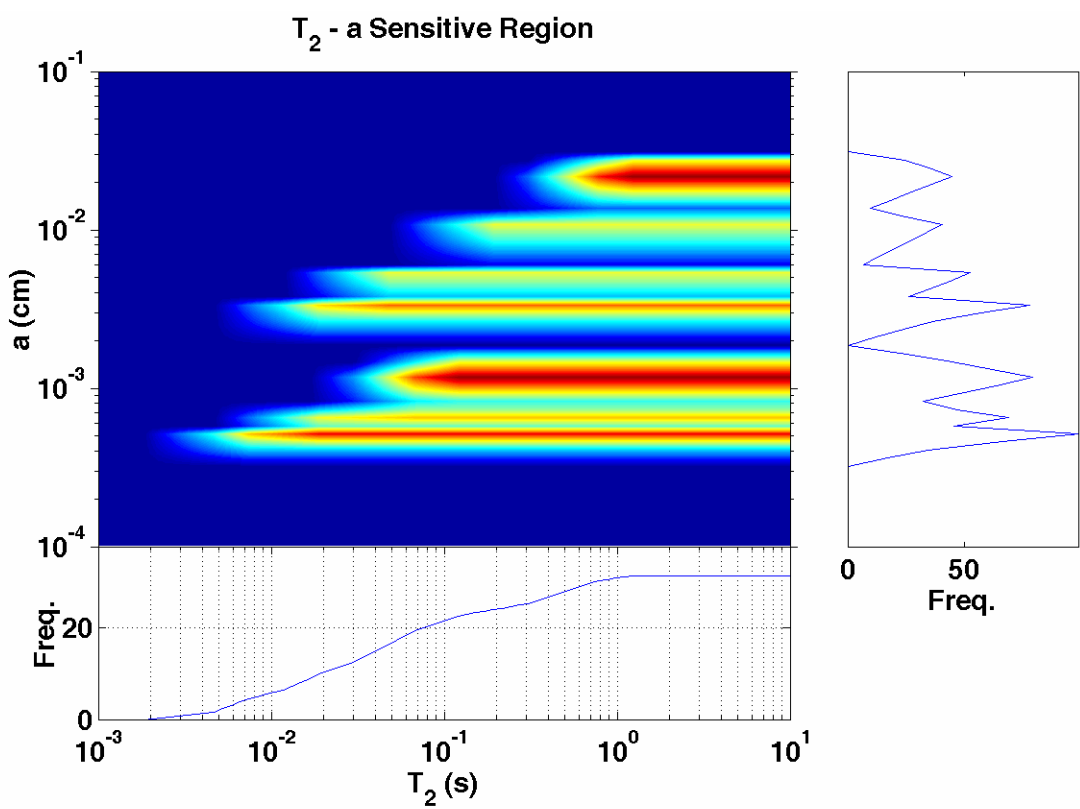


Figure 46: Sensitive range for carbonate sample 1315 saturated with water and methane (4000 psi).

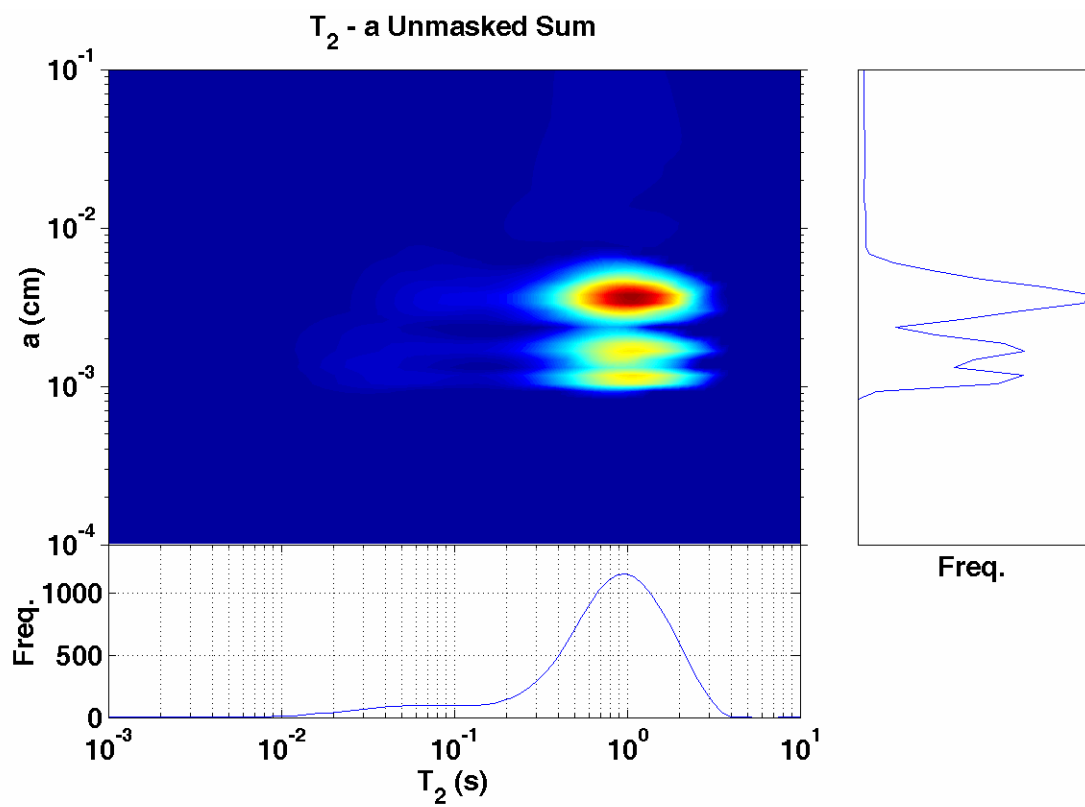


Figure 47: Unmasked sum for carbonate sample 1315 saturated with water and methane (4000 psi).

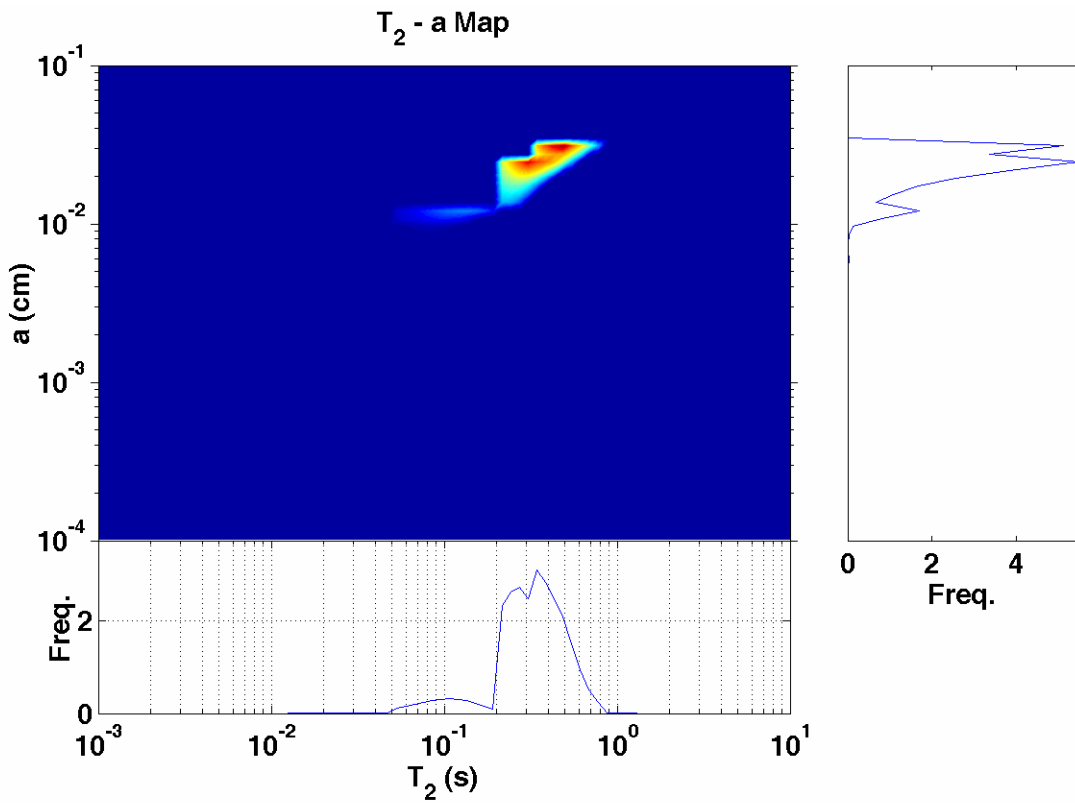


Figure 48: Summary map for carbonate sample 1603 saturated with water, methane (4000 psi), and ethane (600 psi).

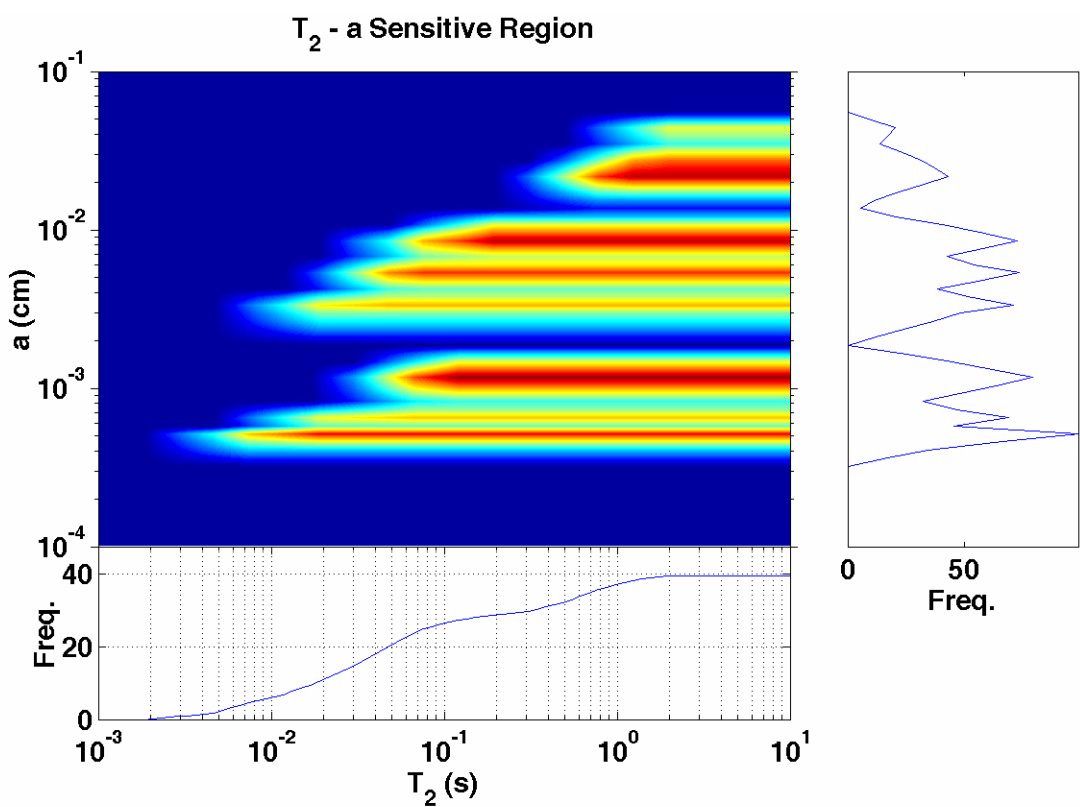


Figure 49: Sensitive range for carbonate sample 1603 saturated with water, methane (4000 psi), and ethane (600 psi).

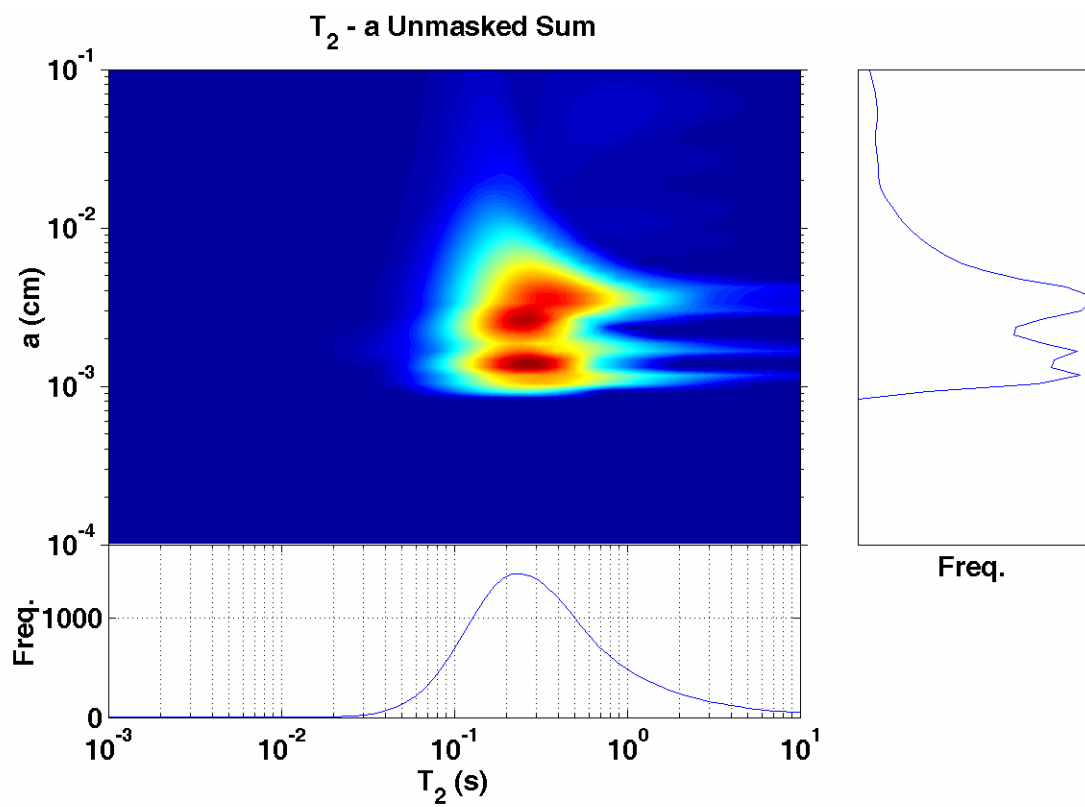


Figure 50: Unmasked sum for carbonate sample 1603 saturated with water, methane (4000 psi), and ethane (600 psi).

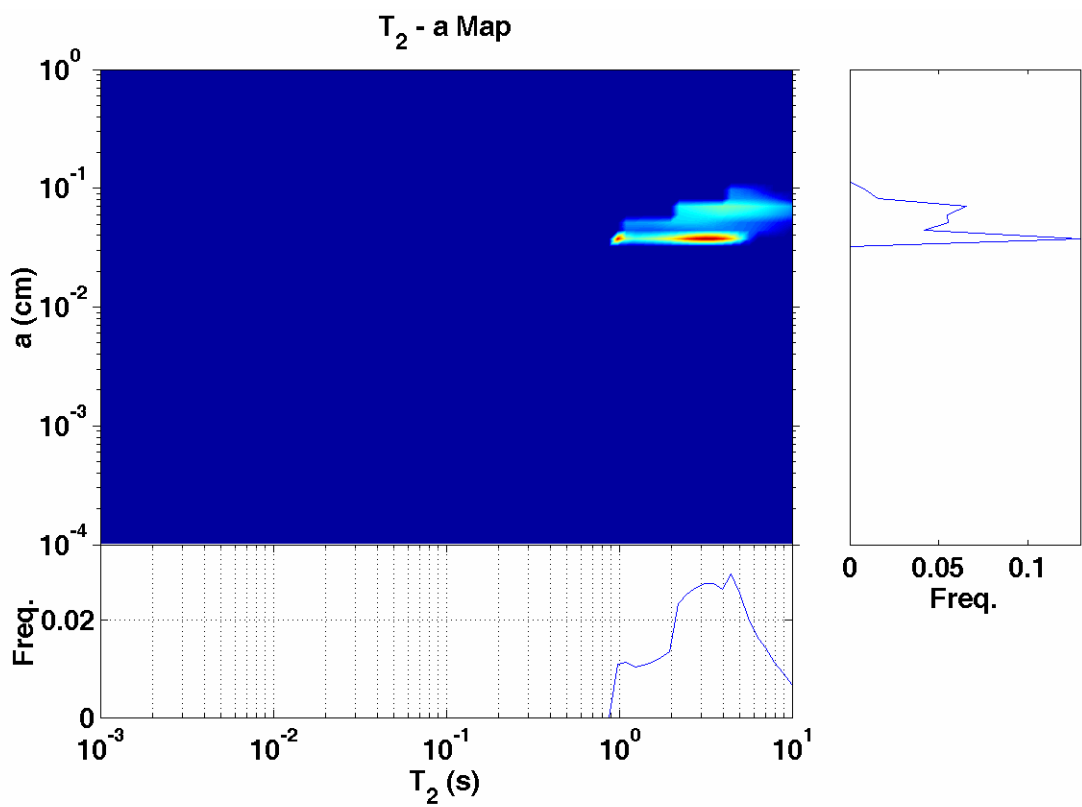


Figure 51: Summary map for carbonate sample cordova saturated with water, methane (4000 psi), and ethane (600 psi).

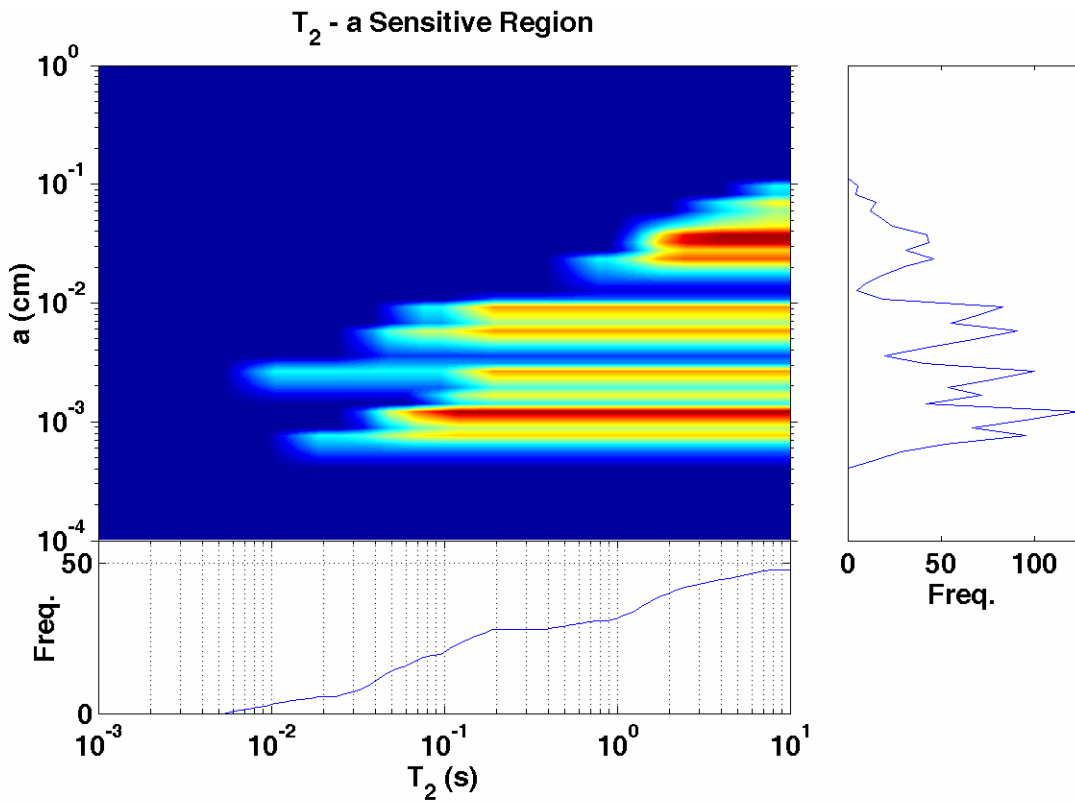


Figure 52: Sensitive range for carbonate sample cordova saturated with water, methane (4000 psi), and ethane (600 psi).

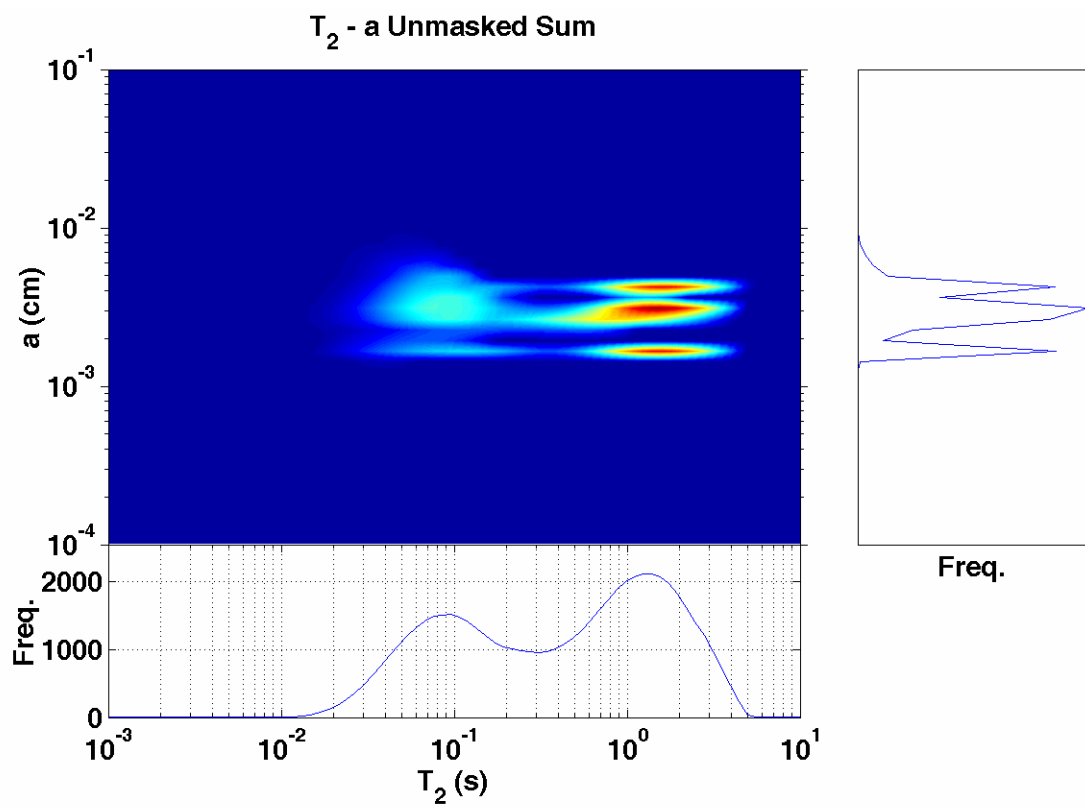


Figure 53: Unmasked sum for carbonate sample cordova saturated with water, methane (4000 psi), and ethane (600 psi).

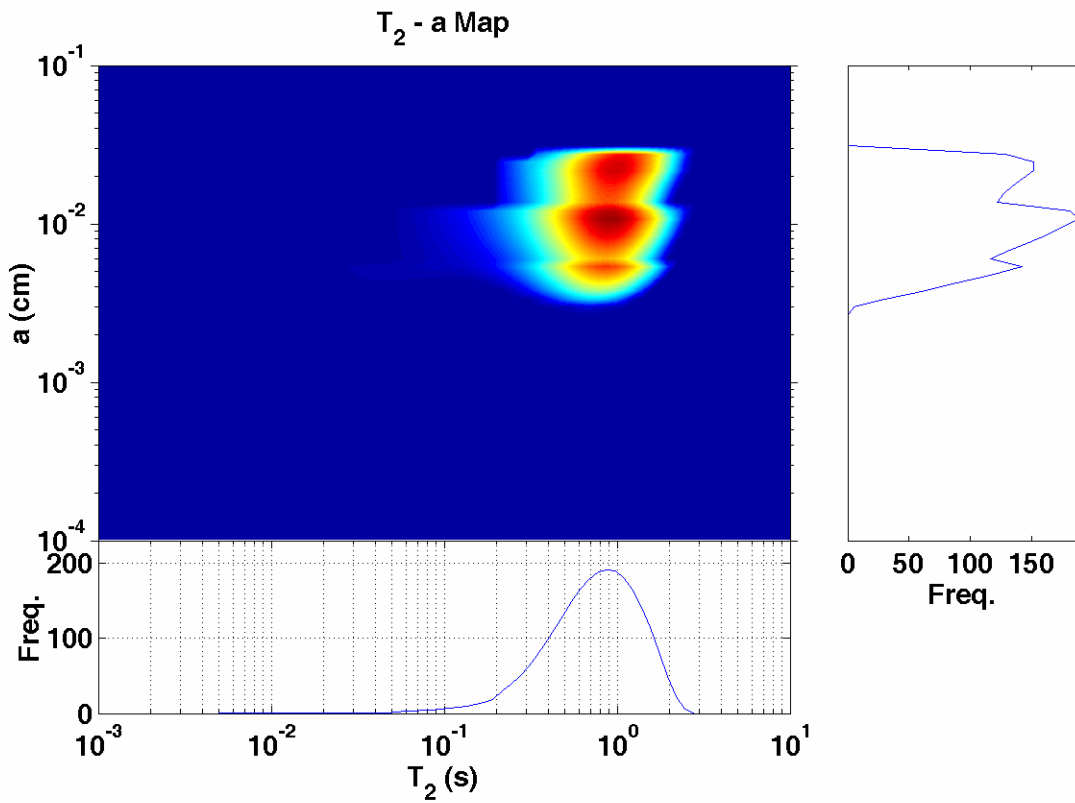


Figure 54: Summary map for carbonate sample iis saturated with methane (4000 psi).

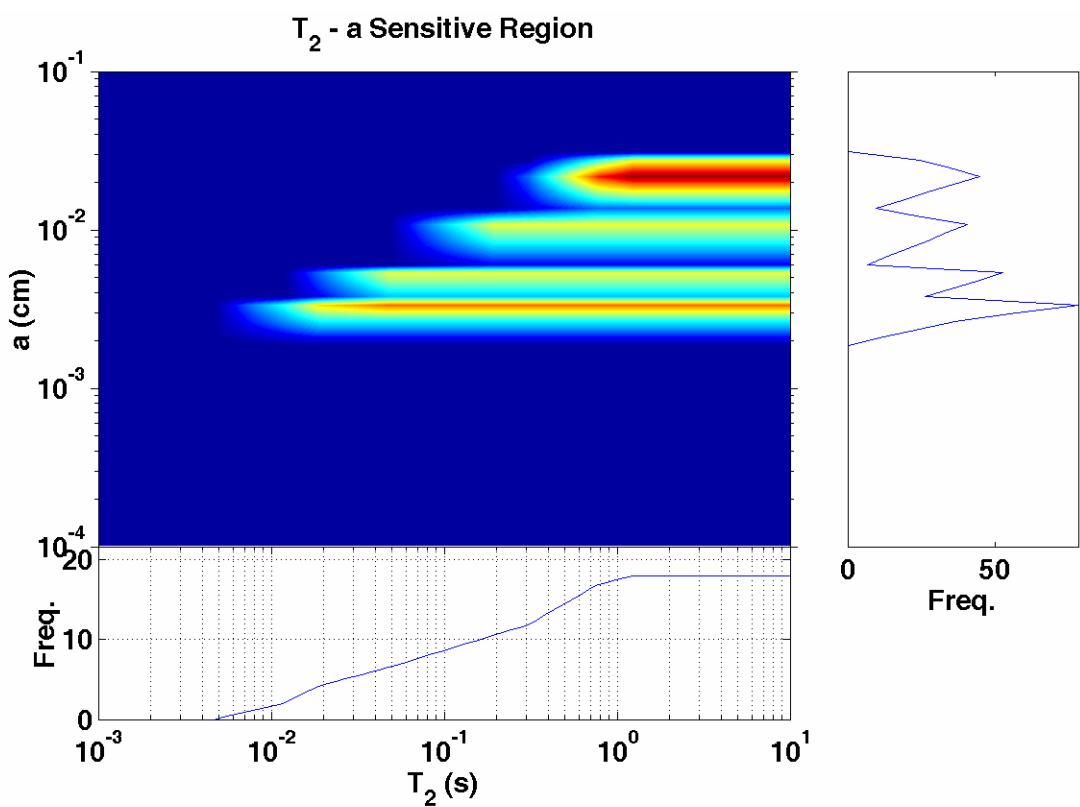


Figure 55: Sensitive range for carbonate sample ils saturated with methane (4000 psi).

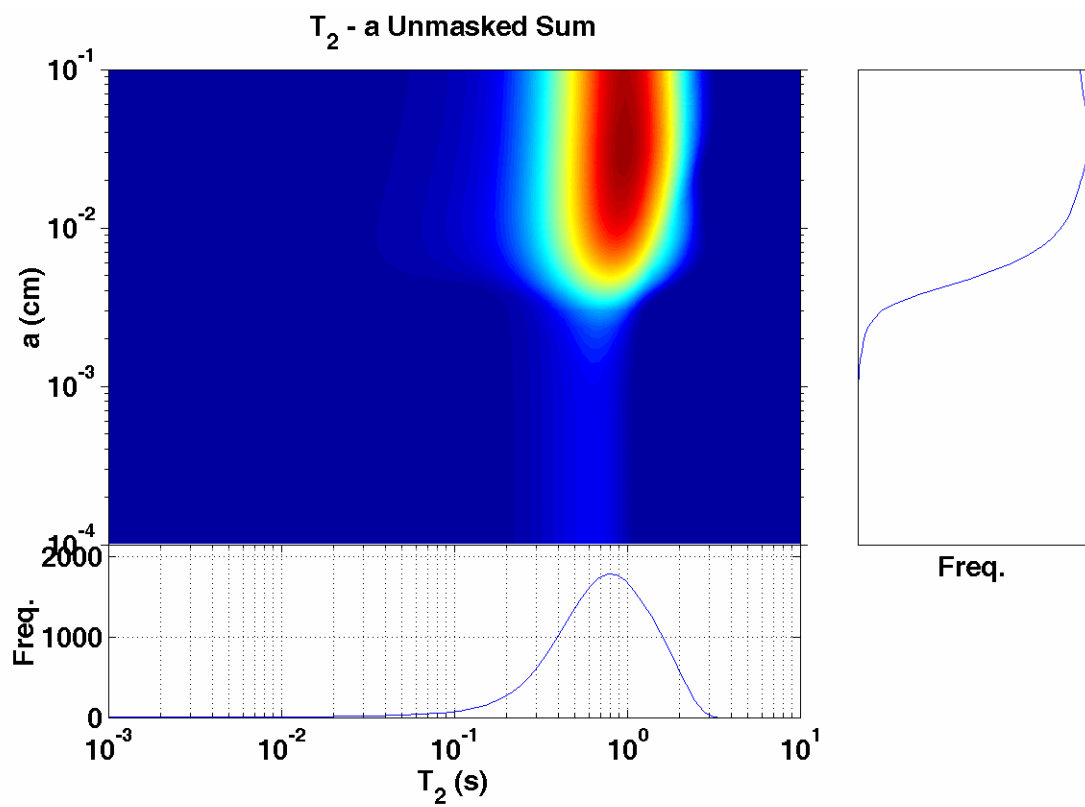


Figure 56: Unmasked sum for carbonate sample ils saturated with methane (4000 psi).

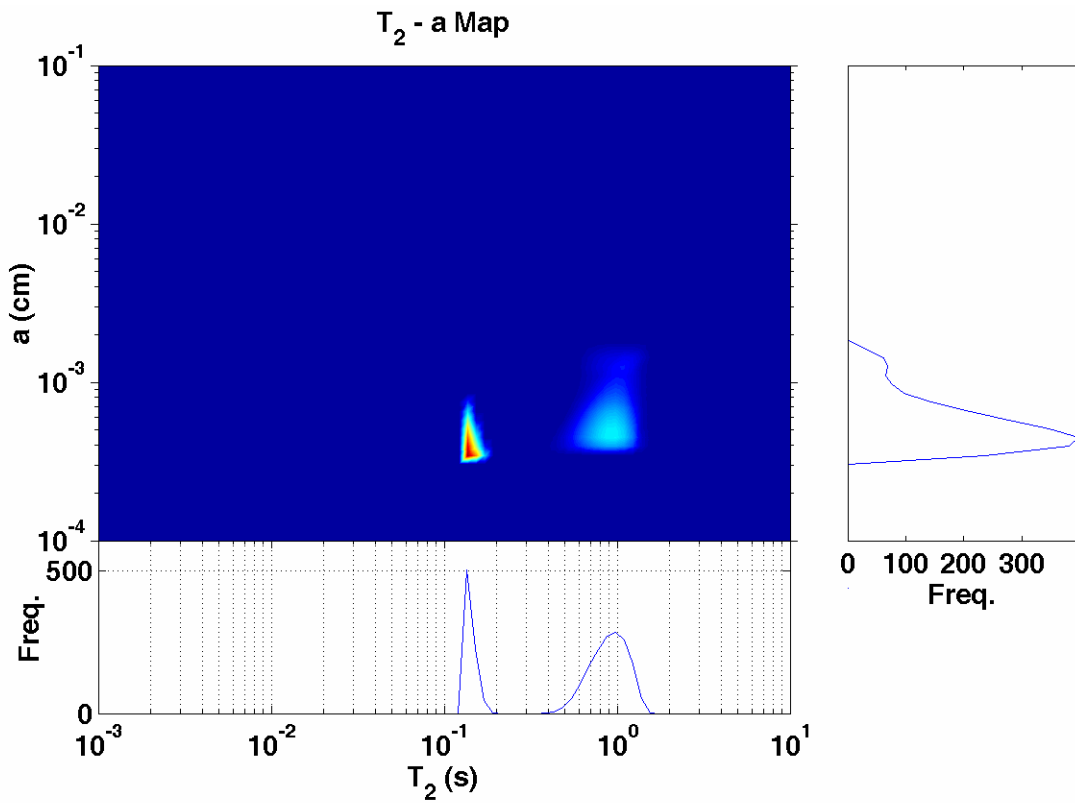


Figure 57: Summary map for emulsion sample.

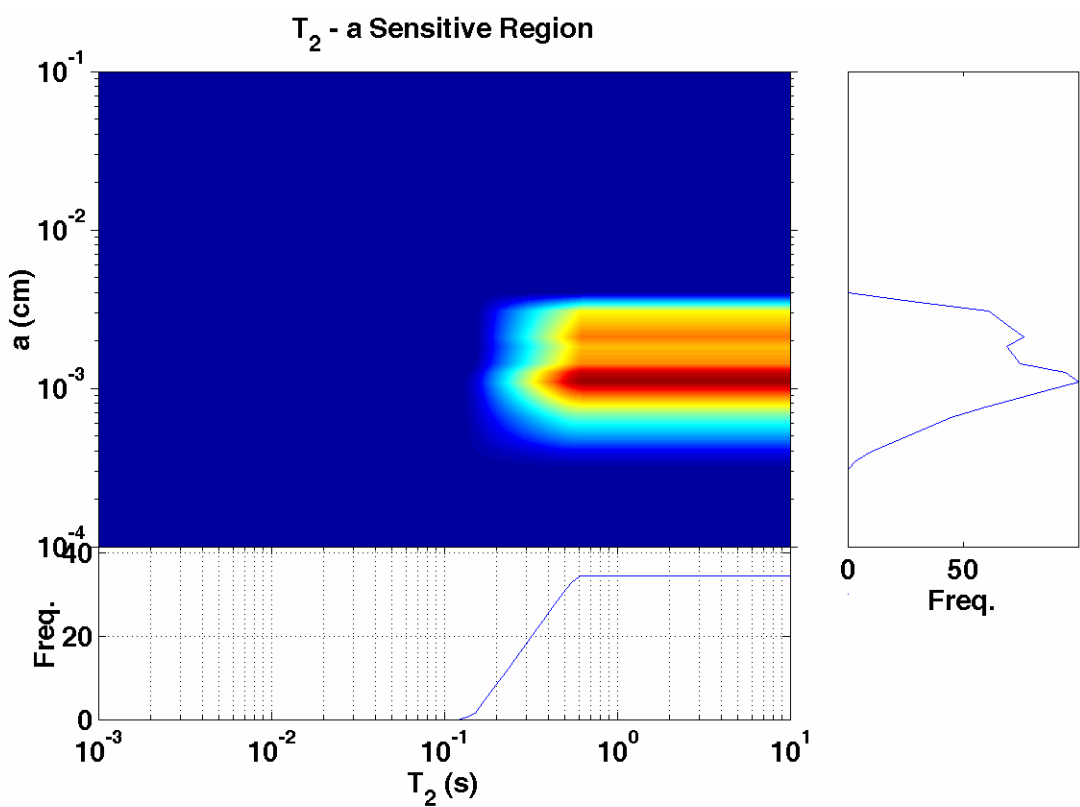


Figure 58: Sensitive range for emulsion sample.

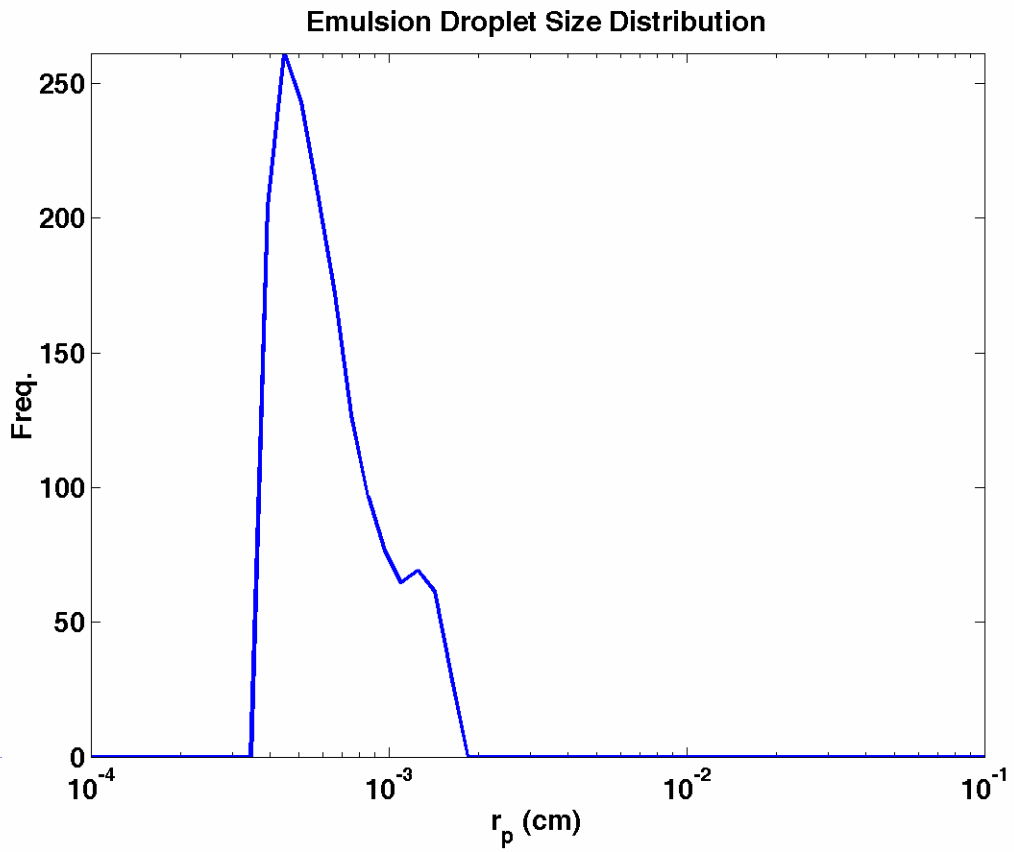


Figure 59: Droplet size obtained by projected water peak of Fig. 57 to the Y axis.

Subtask 2.4: Interpretation of systems with diffusional coupling between pores.

DIFFUSIONAL COUPLING BETWEEN MICRO AND MACROPOROSITY FOR NMR RELAXATION IN SANDSTONES AND GRAINSTONES

Introduction

NMR T_2 measurements are often used to estimate the pore structure and formation properties such as porosity, permeability and irreducible water saturation. NMR pore analysis assumes that in the fast diffusion limit, the T_2 of a fluid in a single pore is given as

$$\frac{1}{T_2} = \frac{1}{T_{2B}} + \rho_2 \left(\frac{S}{V} \right)_{\text{pore}} \quad (1)$$

where T_{2B} is the bulk relaxation time, ρ_2 is the T_2 surface relaxivity and $(S/V)_{\text{pore}}$ is the pore surface-to-volume ratio.

For a rock sample having a pore size distribution, each pore size is assumed to be associated with a T_2 component and the net magnetization relaxes as a multi-exponential decay.

$$M(t) = \sum_j f_j \exp\left(-\frac{t}{T_{2,j}}\right) \quad (2)$$

where f_j is the amplitude of each $T_{2,j}$. Such interpretation of NMR measurements assumes that pores of different sizes relax independent of each other. However, it is observed that this assumption often fails for shaly sandstones and carbonates especially in grainstones and packstones. Ramakrishnan et al. (1999) explained that the failure could be understood by considering the diffusion of fluid molecules between intra (micro) and intergranular (macro) pores. The resulting T_2 distribution is influenced by surface-to-volume ratio of both the micro and macropores and thus, the correspondence between the T_2 and pore size distribution is lost. In such cases, traditional method of employing a sharp $T_{2,\text{cutoff}}$ for estimating bound fluid fractions and permeability would not be applicable. Techniques like “spectral” BVI and tapered $T_{2,\text{cutoff}}$ (Coates et al., 1998, Kleinberg et al., 1997) have been proposed as better estimators of irreducible saturations. However, a theoretical basis for the application of these techniques needs to be established.

The paper is organized as follows. In the first section, we provide the mathematical understanding of NMR relaxation in diffusional coupled systems by numerically solving the Bloch-Torrey equation. In the second and third sections, the theory is extended to explain pore coupling in sandstones and grainstones respectively. Experimental results are provided for both the cases to

substantiate the theoretical models. In the last section, a new technique, based on the analysis of the first section, is introduced for estimation of irreducible water saturation for the coupled systems.

Diffusional Coupling Between Micro And Macropores

Mathematical Modeling - We begin by mathematically modeling the decay of magnetization in pore geometry with a macropore in physical proximity to a micropore (Figure 1). The coupled pore is defined by three geometrical parameters: half-length of the pore (L_2), half-width of the pore (L_1) and microporosity fraction (β). The fluid molecules relax at the surface of the micropore and simultaneously diffuse between the two pore types. As a result, the T_2 distribution of the pore is determined by several parameters such as micropore surface relaxivity, diffusivity of the fluid and geometry of the pore system.

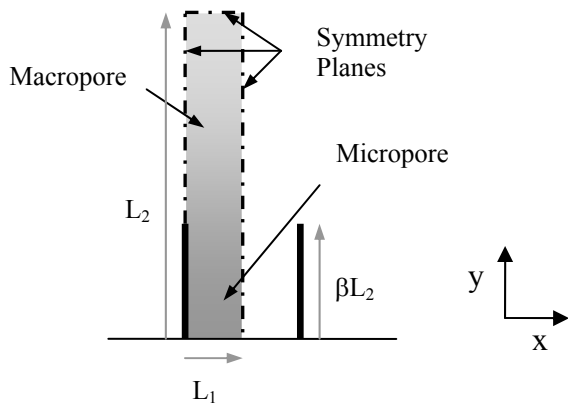


Fig. 1: Physical model of coupled pore geometry. Fluid molecules relax at the micropore surface while diffusing between micro and macropore

The decay of magnetization per unit volume (M) in the pore is given by the Bloch-Torrey equation

$$\frac{\partial M}{\partial t} = D \nabla^2 M - \frac{M}{T_{2B}} \quad (3)$$

The boundary conditions are

$$D \vec{n} \cdot \nabla M + \rho M = 0 \text{ at micropore surface} \quad (4)$$

$$\vec{n} \cdot \nabla M = 0 \text{ at symmetry planes} \quad (5)$$

where \vec{n} is the unit normal pointing outwards from the pore surface and ρ is the surface relaxivity. A uniform magnetization is assumed in the entire pore initially.

In addition, the bulk relaxation rate is assumed to be very small in comparison to surface relaxation and is neglected.

Equation (3) is expressed in dimensionless form by introducing characteristic parameters. The spatial variables are non-dimensionalized with respect to the half-length of the pore (L_2), magnetization with respect to initial magnetization and time with respect to characteristic relaxation time, $T_{2,c}$ defined as

$$T_{2,c} = \frac{V_{\text{total}}}{\rho S_{\text{active}}} = \frac{L_1 L_2}{\rho \beta L_2} = \frac{L_1}{\rho \beta} \quad (6)$$

In the above equation, S_{active} refers to the surface of the micropore at which relaxation is taking place and V_{total} refers to the total volume of the pore. $T_{2,c}$ can also be related to the relaxation time of the micropore $T_{2,\mu}$ defined as

$$T_{2,\mu} = \frac{1}{\rho} \left(\frac{V}{S} \right)_\mu = \frac{\beta L_2 L_1}{\rho \beta L_2} = \frac{L_1}{\rho} \quad (7)$$

$$\Rightarrow T_{2,c} = \frac{T_{2,\mu}}{\beta} \quad (8)$$

We also introduce three dimensionless groups: aspect ratio of the pore η , Brownstein number μ (Brownstein and Tarr, 1979) defined as

$$\eta = \frac{L_2}{L_1} \quad (9)$$

$$\mu = \frac{\rho L_2}{D} \quad (10)$$

The dimensionless groups can be combined into a single parameter called coupling parameter (α) defined as

$$\alpha = \frac{\rho \beta L_2^2}{D L_1} \quad (11)$$

The physical significance of α is detailed later in the Results section. The equations in dimensionless form are given in Appendix A.

Numerical solution- The non-dimensionalized equations (A1-A5) can be numerically integrated for the time evolution of magnetization in the pore. However, the direct numerical integration can lead to non-physical oscillations in the solution due to round off errors. Instead, the governing equations are

expressed in residual form by expressing the unknown as the change in magnetization from the previous iteration as shown

$$\delta M^{k+1} = M^{k+1} - M^k \quad (12)$$

Here, k refers to the iteration index. The equations are then solved for the change in magnetization at each iteration step and the solution added to magnetization at previous step to yield the magnetization at the current step. The iterations are continued till the residual falls below the error tolerance. An Alternating-Direction-Implicit finite difference technique (Peaceman and Rachford, 1955) is employed for the numerical integration. A sequence of five iteration parameters 0.75, 0.075, 0.0075, 0.00025 is found to be optimal in reducing the number of iterations per time step. The time truncation errors are controlled by using an automatic time step (Δt) selector algorithm (Todd et al., 1972). Δt at the next time step is scaled by the ratio of maximum change in M desired to maximum change in M over the entire domain at the previous time step. Thus, the time truncation errors are limited due to small Δt in the beginning of the simulation (when the rate of change of M is large) and large Δt towards the end.

The decay curve is obtained by summing the magnetization values over the entire domain at each time step. Simulated decay data are sampled at the times corresponding to 0.5% change in the average magnetization and fitted to a multi-exponential distribution to obtain the T_2 distribution.

$$\overline{M(t_j)} \approx \sum_i f_i \exp(-t_j/T_{2,i}) \quad (13)$$

where $\overline{M(t_j)}$ is the average magnetization in the entire domain at discrete times (t_j). The coefficients f_i are obtained by minimizing the objective function (Dunn et al., 1994).

$$\sum_j \left[\overline{M(t_j)} - \sum_i f_i \exp(-t_j/T_{2,i}) \right]^2 + \lambda \sum_i f_i^2 \quad (14)$$

In the above expression, λ is the regularizing parameter. The numerical scheme is validated by comparing the numerical solution with the analytical solution obtained by Brownstein and Tarr (1979) for the case of $\beta = 1$ for different values of μ . In all cases, the two solutions match within an accuracy of 0.1% (maximum relative error) indicating the correctness of the numerical solution.

Results - The decay of magnetization in the coupled pore is characterized by three parameters: aspect ratio of the pore (η), microporosity fraction (β) and Brownstein number (μ). Depending on the value of μ , defined as the ratio of relaxation rate to diffusion rate (Equation 15), the decay can be classified into fast, intermediate and slow diffusion regimes.

$$\mu = \frac{\text{Relaxation rate}}{\text{Diffusion rate}} = \frac{\rho/L_2}{D/L_2^2} = \frac{\rho L_2}{D} \quad (15)$$

In the fast diffusion regime ($\mu \ll 1$), the lowest eigen value of the diffusion equation (Equation 3) completely dominates and the decay curve is mono-exponential whereas in the slow diffusion regime ($\mu \gg 10$), the higher modes also contribute to the relaxation and the decay curve is multi-exponential (Brownstein and Tarr, 1979). These diffusion regimes can be seen with the help of snapshots of magnetization in the pore at intermediate decay times. Figure 2 shows the contour plots of magnetization for $\beta = 0.5$ and $\eta = 10$ at dimensionless time $t = 1$ for various values of μ . For μ small compared to 1 ($\mu = 0.1$), fast diffusion leads to nearly homogenous magnetization in the entire pore. With the increase in the value of μ , gradients in the longitudinal direction become substantial. The gradients imply that the micropore is relaxing much faster than the macropore.

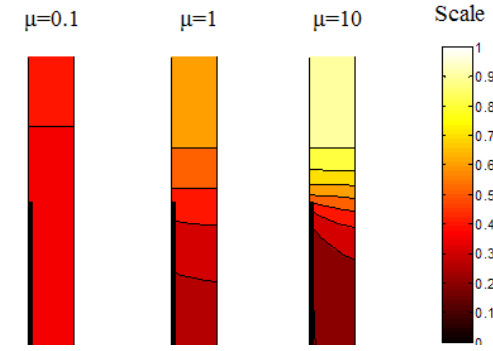


Fig. 2: Contour plots at $t = 1$ showing uniform magnetization for small μ and gradients for larger μ .

Note that μ is based on an analysis for a one-dimensional system as is evident from its functional dependence on the length scale (L_2) of macropore only. Hence, it cannot explain the results for a system with two intrinsic length scales i.e. L_1 and L_2 .

Coupling Parameter- Two processes characterize the decay of magnetization in the coupled geometry: relaxation of spins at the micropore surface and diffusion of spins between the micro- and macropore. If the relaxation of spins in the micropore is much faster than the inter-pore diffusion, coupling between the two pore types is small. On the other hand, if the diffusion rate is much greater than the relaxation rate, the two are significantly coupled with each other. The extent of coupling can, thus, be characterized with the help of a coupling parameter (α) which compares the characteristic relaxation rate of the pore to the rate of diffusional mixing of spins between micro and macropore i.e.

$$\alpha = \frac{1/T_{2,c}}{D/L_2^2} = \frac{\rho\beta/L_1}{D/L_2^2} = \frac{\rho\beta L_2^2}{DL_1} = \beta\eta\mu \quad (16)$$

The physical significance of α can be illustrated with the help of simulated T_2 distributions for the previously mentioned case of $\beta = 0.5$ and $\eta = 10$ (Figure 3). For $\alpha = 0.5$, the T_2 distribution shows a single peak since the entire pore is relaxing at a single relaxation rate due to fast diffusion. As the value of α

increases, some spins in the micropore are able to relax faster than they can diffuse into the macropore. This results in the appearance of a peak at short relaxation times (micropore peak). Moreover, the spins in the macropore diffuse to the micropore slowly and hence a shift of the macropore peak towards longer relaxation times. As we get into still slower diffusion regime, the inter-pore diffusion becomes negligible and the entire micropore relaxes independent of the macropore.

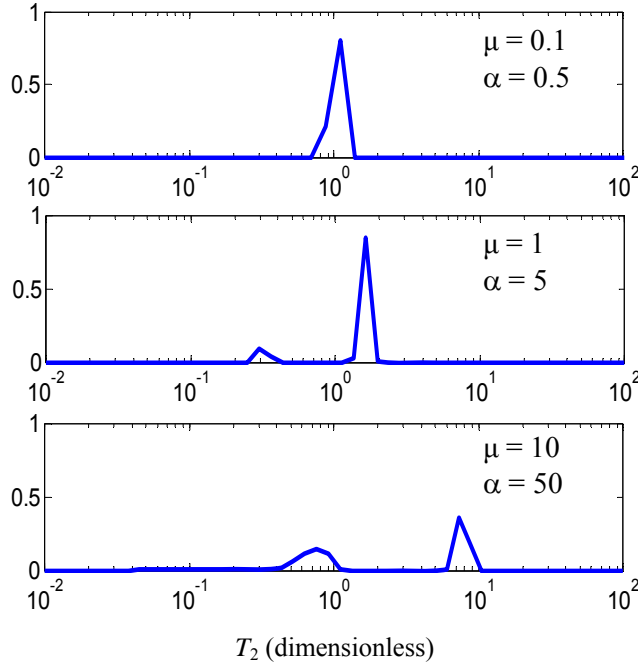


Fig. 3: The T_2 distributions as a function of α with the parameters chosen to correspond to those of Figure 2.

Micropore relaxation - The amplitude of the micropore peak (called φ) gives the magnitude of the fraction of the microporosity which is decoupled from the rest of the pore. φ , thus, serves as the criterion to quantify the extent of coupling between the micro and macropore. For totally coupled micro and macropore $\varphi = 0$ while for decoupled porosities $\varphi = \beta$. A value of φ between 0 and β indicates an intermediate state of diffusive coupling. Figure 4 shows the cross-plot between φ normalized by β (henceforth referred to as **independent microporosity fraction**) and α . The curves correspond to different β and span a range of η from 10 to 1000. The results show that depending on the value of α , the micro and macropore can be in one of the three states of

- Total coupling ($\alpha < 1$): For values of α less than 1, diffusion is much faster than the relaxation of the magnetization in the micropore. The micropore is totally coupled with macropore and the entire pore relaxes with a single relaxation time.

- Intermediate coupling ($1 < \alpha < 250$): In this case, diffusion is just fast enough to couple some of the micropore with macropore. The T_2 distribution consists of distinct peaks for the two pore types but the amplitudes of the peaks are not proportional to the porosity fractions.

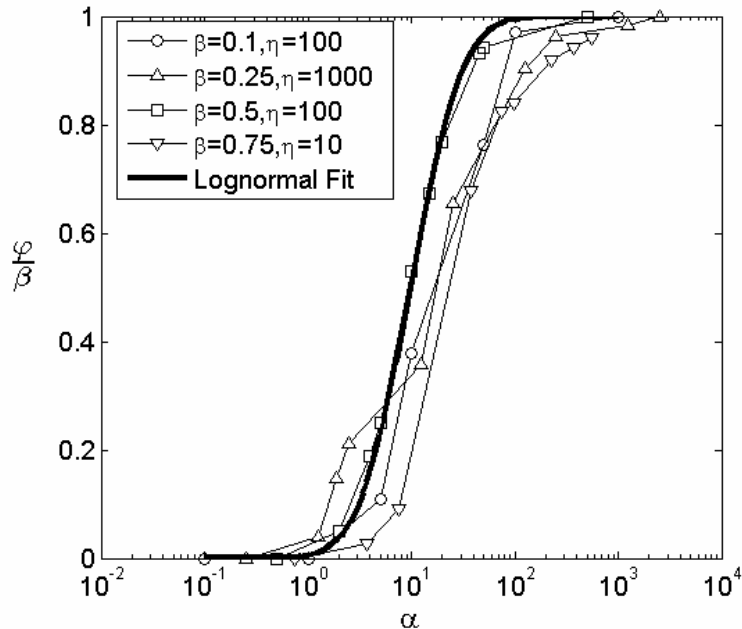


Fig 4: Independent microporosity fraction (ϕ/β) shows lognormal relationship with α . Three regimes of coupling (see text) can be identified using α .

- Decoupled ($\alpha < 250$): The two pore types become independent of each other and the T_2 spectrum consists of separate peaks with amplitudes representative of the porosity fractions (β and $1-\beta$ for micro and macroporosity respectively). Further, the dimensionless relaxation time of the micropore peak reaches a value β (Appendix B) indicating complete independence of the two pores. It was also found that the independent microporosity fraction correlates more strongly with α than with μ . This is because α has dependence on the length scale of both micro and macropore and thus, provides a better measure to quantify extent of coupling.

The sigmoidal character of the curves in Figure 4 suggests that we can establish a lognormal relationship between the independent microporosity fraction and α . Mathematically, the relationship can be expressed as

$$\frac{\phi}{\beta} = \frac{1}{2} \left[1 + \operatorname{erf} \left(\frac{\log \alpha - 2.29}{0.89\sqrt{2}} \right) \right] \quad (17)$$

The choice of mean and standard deviation of the lognormal relationship is governed by experimental results, as shown later.

Macropore relaxation— Since the relaxation of both micro and macropore is governed by the same Bloch equation, we expect the relaxation time of the macropore to also correlate with α . It was found that the macropore relaxation time correlates with the product of α and square of macroporosity fraction $(1-\beta)$. This is because the product $(1-\beta)^2 \alpha$ represents the normalized diffusion time (t_d) within the macropore as described below

$$(1-\beta)^2 \alpha = \frac{(1-\beta) L_2^2 / D}{L_1 / \rho \beta} = \frac{t_d}{T_{2,c}} \quad (18)$$

Figure 5 shows the plot of dimensionless relaxation time of the macropore with $v = (1-\beta)\sqrt{\alpha}$ for different parameter values. Here, the relaxation time is correlated with v instead of its square because v is proportional to the length scale, L_2 , of macropore (Equation 18).

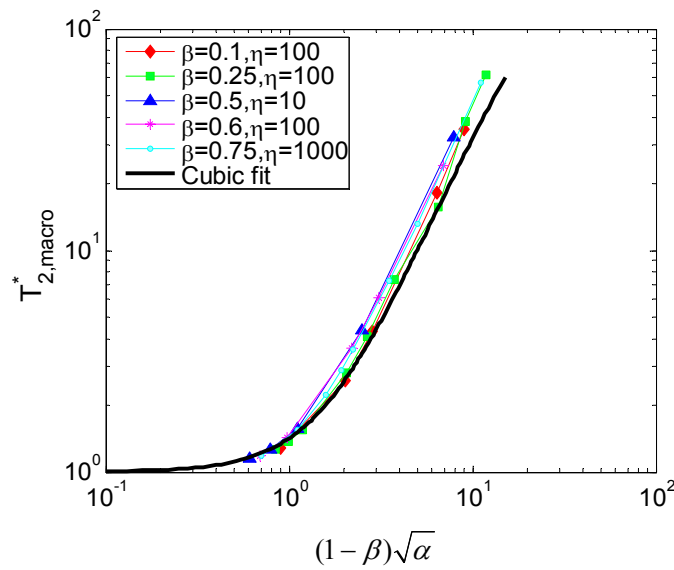


Fig. 5: Relaxation time of macropore shows cubic relationship with $(1-\beta)\sqrt{\alpha}$.

We can establish a cubic relationship between the dimensionless macropore relaxation time and v as shown in Equation 19. The functional relationship, although fitted to experimental results for grainstones and sandstones as shown later, closely match the simulation results.

$$T_{2,\text{macro}}^* = 1 + 0.025 * v + 0.4 * v^2 - 0.009 * v^3 \quad (19)$$

where $10^{-1} < v < 10^1$

SANDSTONES

In this section we will extend the ideas developed in the previous section to describe diffusional coupling in clay-lined pores in sandstones. Straley et al. (1995) modeled the clay flakes as forming microchannels perpendicular to the pore walls such that each micropore opens to a macropore (Figure 6). The two dimensional structure of the clay-lined pore can be modeled as a periodic array of rectangular flakes arranged along the wall of the macropore (Zhang et al., 2001, Zhang et al., 2003). Since the model is periodic, the relaxation process can be adequately modeled by considering only the symmetry element between two clay flakes. The model can be further simplified to the one in previous section by approximating the flakes to be needle shaped with negligible thickness.

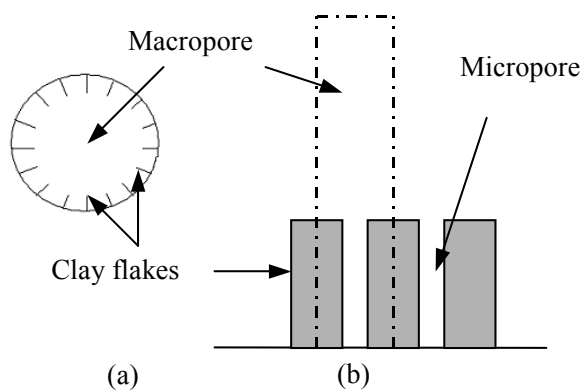


Fig. 6: a) *Model of a clay lined pore showing micropores opening to a macropore* b) *Simplified model with rectangular clays arranged along macropore wall.*

Pore size distribution- To experimentally validate the theoretical model, the NMR response of North-Burbank (NB) sandstone with pores lined with clay flakes is simulated (Trantham and Clampitt, 1977). Analysis of the sandstone cores yielded an average porosity of 0.21 and air/brine permeability of 220 md. The pore size distribution obtained by mercury porosimetry is shown in Figure 7. The bimodal structure of the pore size distribution arises due to the presence of pore-lining chlorite flakes. Mercury first invades the macropores giving rise to the peak at larger pore radii. The clay flakes, being closely spaced, are invaded by mercury at high capillary pressures which gives rise to the peak at smaller pore radii.

A lognormal pore size distribution with mean of $8 \mu\text{m}$ and standard deviation 0.135 is simulated to approximate the distribution of macropores (Figure 8). Since mercury porosimetry measures the distribution of pore throats, the distribution of pore bodies is obtained by assuming a fixed pore body to pore

throat ratio of 3 (Lindquist et al., 2000). Thus, the characteristic pore (corresponding to the mode of the distribution) has the pore radius of 24 μm . Each pore is then modeled to be lined with clay flakes which are assumed to be of constant length and equally spaced in all pores. As a result, clay flakes completely occupy the small pores and form a thin rim on the surface of larger pores. The distance between the flakes is given by the peak at smaller pore radius in the pore size distribution.

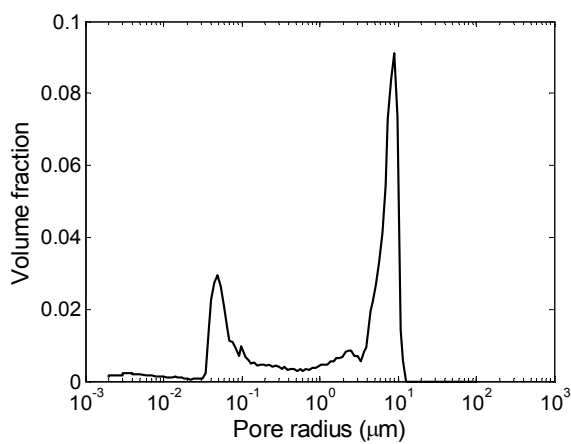


Fig. 7: The bimodal pore size distribution for NB sandstone arises due to pore-lining chlorite.

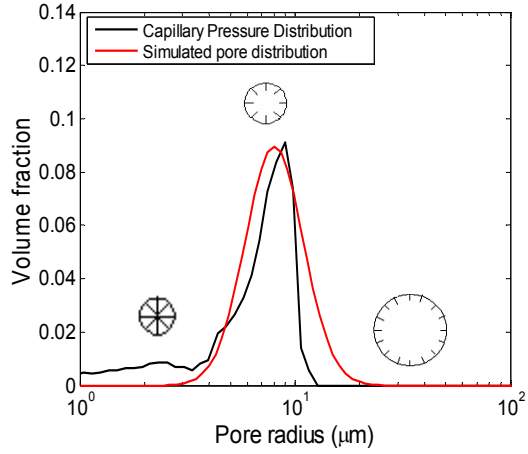


Fig. 8: A lognormal distribution is simulated to approximate the distribution of macropores. Also shown are the pores with changing proportion of pore volume occupied by the clay flakes.

Numerical solution- In order to solve the Bloch equation for the decay of magnetization in the i^{th} pore, we need three parameters for each pore:

- Microporosity fraction β_i
- Aspect ratio $\eta_i = L_{2,i}/L_{1,i}$
- Brownstein number $\mu_i = \rho L_{2,i}/D$

The parameters in different pores are, however, not totally independent of each other since they are constrained by the assumptions of constant length and equal spacing between clay flakes in all pores. Mathematically, the constraints imply

$$L_{1,i} = L_{2,i} = \text{const.} \quad (20)$$

$$\beta_i L_{2,i} = \beta_c L_{2,c} = \text{const.} \quad (21)$$

where the subscript “c” refers to the characteristic pore.

Hence, if we specify the parameters for the characteristic pore, the parameters for the rest of the pores can be calculated by making use of the constraints. Similar to the analysis of a single pore in the previous section, the governing equations (3-5) for each pore are non-dimensionalized with respect to common characteristic parameters. Hence, the spatial variables and time are respectively normalized by the radius and relaxation time of the characteristic pore (Equation 6). The normalized equations are then solved for the decay of magnetization in each pore individually. The magnetization in the entire pore structure is computed by interpolating the individual magnetization values at some common values of time and then summing them over the entire volume. The total magnetization (M_{tot}) in the pore structure is given as

$$M_{\text{tot}}(t) = \sum_i^{N_p} V_{p,i} M_i(t) \quad (22)$$

where N_p is the number of pores, $V_{p,i}$ is the volume fraction of the i^{th} pore and M_i is the magnetization in the i^{th} pore at dimensionless time t . The T_2 distribution for the pore structure is obtained by fitting a multi-exponential distribution to the total magnetization.

Results- Since each pore in the pore size distribution has a different value of α , a volume averaged $\bar{\alpha}$ for the pore structure is defined as

$$\bar{\alpha} = \sum_i \alpha_i V_{p,i} \quad (23)$$

The simulated T_2 distributions for the pore size distribution with typical values of β_c and η_c ($\beta_c = 0.3$ and $\eta_c = 100$) are shown in Figure 9 as a function of $\bar{\alpha}$.

We can see that the T_2 distribution changes from unimodal to bimodal with the increase in the values of $\bar{\alpha}$. This is because when $\bar{\alpha} < 1$, the pores are in total coupling regime and each pore relaxes single exponentially with the dimensionless relaxation time, $T_{2,i}$, given as

$$T_{2,i} = \frac{(V/\rho S)_i}{T_{2,c}} = \frac{\beta_c}{\beta_i} = \frac{L_{2,i}}{L_{2,c}} \quad (24)$$

Thus, for $\bar{\alpha} < 1$, the T_2 distribution exactly replicates the unimodal lognormal distribution of the pore radii. As the pores enter the intermediate coupling regime ($\bar{\alpha} > 1$), a fraction of microporosity starts relaxing independently of the macroporosity giving the T_2 distributions a bimodal shape.

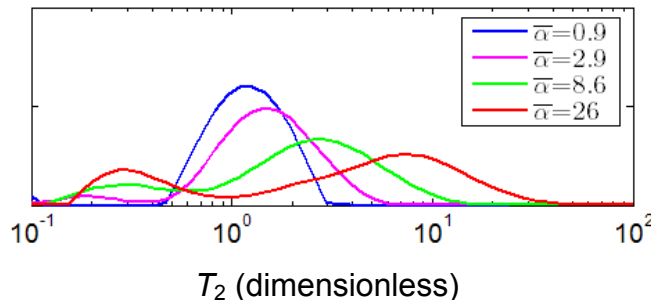


Fig. 9: Simulated T_2 distributions for $\beta_c = 0.3$ and $\eta_c = 100$ showing transition from unimodal to bimodal distribution with increase in $\bar{\alpha}$.

To compare the simulations with experimental results for NB, the characteristic parameters are chosen such that they are representative of the core properties. Hence, the value of β_c is calculated such that the microporosity fraction of the simulated pore size distribution corresponds to the irreducible water saturation, i.e

$$\sum_i^{N_p} \beta_i V_{p,i} = S_{w,\text{irr}} \quad (25)$$

$$\Rightarrow \beta_c = \frac{S_{w,\text{irr}}}{L_{2,c} \sum_i^{N_p} \frac{V_{p,i}}{L_{2,i}}} \quad (26)$$

The aspect ratio η_c is calculated from the ratio of macropore and micropore radii obtained from mercury porosimetry. The third parameter μ_c is specified such that the simulations best match with the experimental results.

Figure 10 shows the comparison of T_1 distributions of three water-saturated NB cores with the corresponding simulated distributions. Here, the comparison is made with the T_1 (instead of the T_2) distributions since the T_2 relaxation is influenced by the internal gradients induced by chlorite flakes (Zhang et al., 2001, Zhang et al., 2003). The characteristic parameters for the simulations are shown in Table 1. The dimensionless simulated distributions are dimensionalized by choosing $T_{2,c} = 50, 44$ and 40ms respectively which gives the best overlay of the simulated and experimental distributions. We can see that the simulated distributions very well estimate the location as well as the amplitudes of the micro and macropore peaks. The values of $\bar{\alpha}(=12.2, 15$ and $16.6)$ indicate that the two pore types are in intermediate coupling regime. This is also demonstrated in Figure 11 (a) where we plot the amplitude of the micropore peak at 100% water saturation normalized with the total microporosity fraction vs.

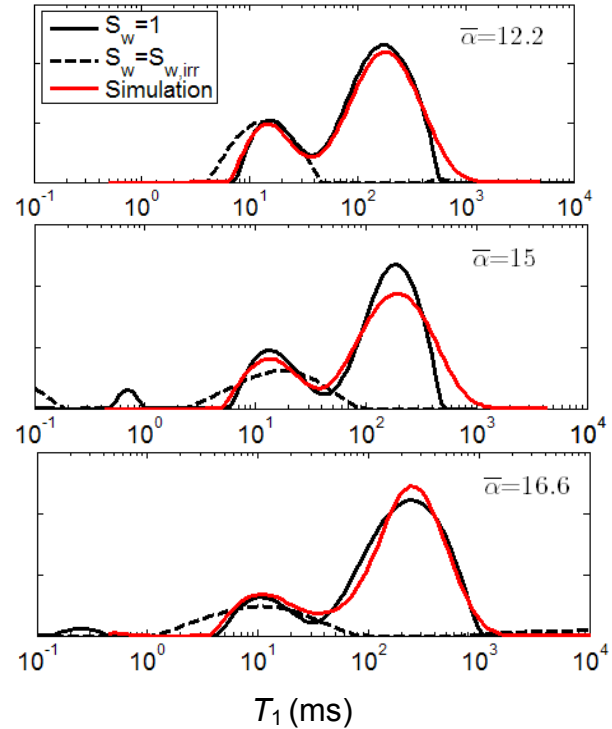


Fig. 10: Comparison of simulated and experimental T_1 distributions for three water saturated NB cores

α for the three cores. The measurements fall on the intermediate coupling regime of the lognormal relationship (Equation 17). Figure 11 (b) shows that the cubic relationship (Equation 19) for the normalized macropore relaxation time also holds for the three cores. In the figure, the relaxation time of the macropore is normalized by the characteristic relaxation time defined by Equation 8.

Table 1: Characteristic parameters for the simulations for three NB cores.

Core	β_c	η_c	μ_c	$\bar{\alpha}$
NB1	0.3	800	0.048	12.2
NB2	0.28	800	0.065	15
NB3	0.21	800	0.094	16.6

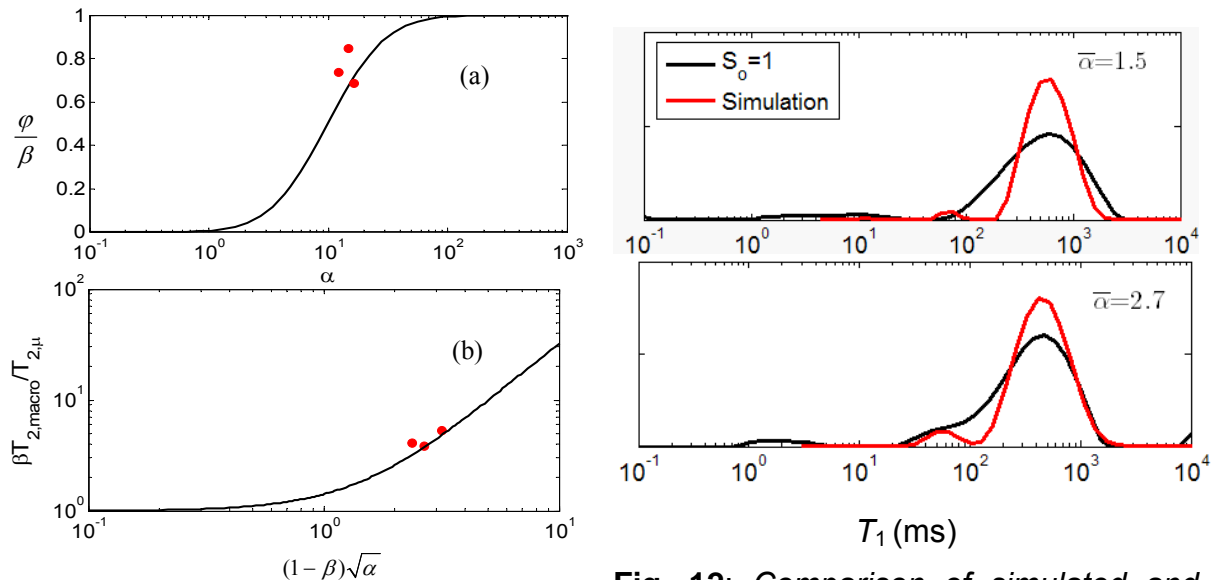


Fig. 11: a) Independent microporosity fraction agrees with lognormal relationship b) Normalized relaxation time agrees with cubic relationship.

Fig. 12: Comparison of simulated and experimental distributions for two hexane saturated NB cores.

To explore other coupling regimes, measurements were done with cores saturated with hexane. Higher extent of coupling is expected with hexane than with water due to higher diffusivity and lower surface relaxivity for hexane. Figure 12 shows the T_1 distributions of cores NB1 and NB2 saturated with hexane and the corresponding simulated distributions. The dimensionless distributions are

dimensionalized by choosing $T_{2,c} = 500$ and 360 ms respectively. Now the T_1 distributions show unimodal distributions implying the merger of the micro and macropore peak. The smaller values of $\bar{\alpha}$ also suggest stronger coupling for hexane than for water.

Estimation of surface relaxivity - We can calculate the values of the surface relaxivity for the cores from the corresponding values of $\bar{\alpha}$. For the values of parameters $L_{2,c} = 24 \mu\text{m}$, $L_1 = 0.03 \mu\text{m}$, diffusivity for water and hexane $D_W = 2.5 (\mu\text{m})^2/\text{ms}$ and $D_H = 4.2 (\mu\text{m})^2/\text{ms}$ (Reid et al, 1987), the average value of relaxivity is found to be $7.1 \mu\text{m/sec}$ for water and $1.6 \mu\text{m/sec}$ for hexane. Another estimate of relaxivity can be obtained by comparing the cumulative pore size distributions obtained from T_1 relaxation and mercury porosimetry. However, the estimates from the latter method are about three times ($20 \mu\text{m/sec}$) as high as those calculated from simulations. This is because mercury porosimetry does not take into account the large surface area provided by the clay flakes in the estimation of relaxivity.

GRAINSTONES

The analysis of the first section (on diffusional coupling) can also be applied to describe pore coupling in grainstone carbonates. Ramakrishnan et al. (1999) modeled the grainstones as microporous spherical grains surrounded by intergranular pores. This three dimensional model can be mapped into a two-dimensional model of periodic array of slab-like grains separated by intergranular macropores as shown in Figure 13. We can transform this model to the model discussed in the first section by neglecting the thickness of grain between the micropores and assuming the pores to be linear in shape. Note that in this model relaxation at the outer surface of the grains is neglected. We are justified in making this assumption if the surface-to-volume ratio of the micropore is much larger than the external surface-to-volume ratio of the spherical grains.

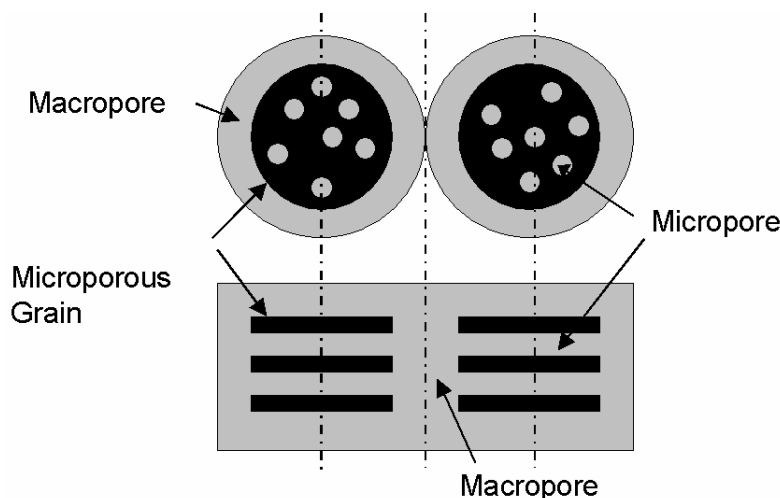


Fig. 13: Reduction of a three dimensional grainstone model to a two-dimensional one.

Coupling parameter for grainstones- The transformation of the spherical grain model to the 2-D model enables us to define a coupling parameter for grainstones through a mapping of characteristic parameters. In the original model, L_1 was defined to be the half-width of the micropore. Hence for microporous grains, L_1 corresponds to the radius of the micropore (R_μ) i.e.

$$L_1 = R_\mu \quad (27)$$

Also, as a first approximation, L_2 can be taken to be equal to the grain radius (R_g)

$$L_2 = R_g \quad (28)$$

Substituting Equations (27) and (28) in Equation (11), we get the definition of α for grainstones as

$$\alpha_{\text{grain}} = \frac{\rho \beta R_g^2}{D R_\mu} \quad (29)$$

α_{grain} , thus, shows a quadratic dependence on the grain radius and inverse dependence on the micropore radius. This suggests that grainstones with large grain radius or small micropore radius are expected to show less effect of diffusional coupling.

The above definition of coupling parameter also helps us to understand the analysis of grainstone model developed by Ramakrishnan et al. (1999). suggested that in the case when the decay of magnetization in macropore occurs on a time scale much larger than the decay of magnetization in micropore, relaxation in the coupled geometry can be expressed as a bi-exponential decay

$$M(t) = f_m \exp\left(-\frac{\rho_a t}{V_{sm}}\right) + (\phi - f_m) \exp\left(-\frac{t}{T_{2,\mu}}\right) \quad (30)$$

In the above equation, V_{sm} is the macropore volume-to-surface ratio, ϕ and f_m are the total porosity and macroporosity respectively and ρ_a is the apparent relaxivity for the macropore. The bi-exponential model is valid when the diffusion length of magnetization within the microporous grain is much smaller than the grain radius i.e.

$$\sqrt{\frac{DT_{2,\mu}}{\phi_\mu F_\mu}} \ll R_g \quad (31)$$

where F_μ is the formation factor. We can understand the above condition by substituting the expressions for the parameters from our model as described below. Thus, the relaxation rate of the micropore is related to the micropore radius as

$$\frac{1}{T_{2,\mu}} = \rho \left(\frac{S}{V} \right)_\mu = \frac{2\rho}{R_\mu} \quad (32)$$

The microporosity fraction β is related to the porosity of grains ϕ_μ and total porosity ϕ as

$$\beta = \frac{\phi_\mu(1-f_m)}{\phi} \quad (33)$$

Substituting the expressions for $1/T_{2,\mu}$ and ϕ_μ from Equations (32) and (33) in (31), we get

$$\sqrt{\frac{DR_\mu(1-f_m)}{\rho\beta\phi F_\mu}} \ll R_g \quad (34)$$

$$\Rightarrow \alpha_{\text{grain}} \equiv \frac{\rho\beta R_g^2}{DR_\mu} \gg \frac{(1-f_m)}{\phi F_\mu} \quad (35)$$

The above condition implies that the micropore relaxes independently of the macropore for large values of α , which is the same condition for the decoupled regime obtained for our model. However, for typical values of grainstone parameters, the value of apparent relaxivity can be an order of magnitude larger than the intrinsic relaxivity and the decay of macropore would occur on a time scale comparable to that of micropore. For such cases, the pores are in intermediate coupling regime and the amplitudes of the bi-exponential fit are not representative of the actual micro and macroporosity fractions.

Experimental validation- In order to experimentally validate the grainstone model, NMR response of microporous chalk, silica gels and alumino-silicate molecular sieves is studied as a function of grain radius. These systems with varying physical properties help us to systematically analyze the effect of different governing parameters on pore coupling. The physical properties of the systems are listed in Table 2.

Table 2: Physical properties of the grainstone systems

	Chalk	Silica Gels	Molecular Sieves
Surface Area (m ² /g)	4.1	300	20
Micropore Diamter (Å)	185	150	4
Relaxivity (μm/sec)	0.27	0.06	0.04

1. Chalk- Crushed chalk was sieved into five fractions with average grain diameters of 630 μm , 360 μm , 223 μm , 112 μm and 22 μm . The T_2 distributions of the five fractions at 100% water saturation and the corresponding distributions at irreducible saturation are shown in Figure 14.

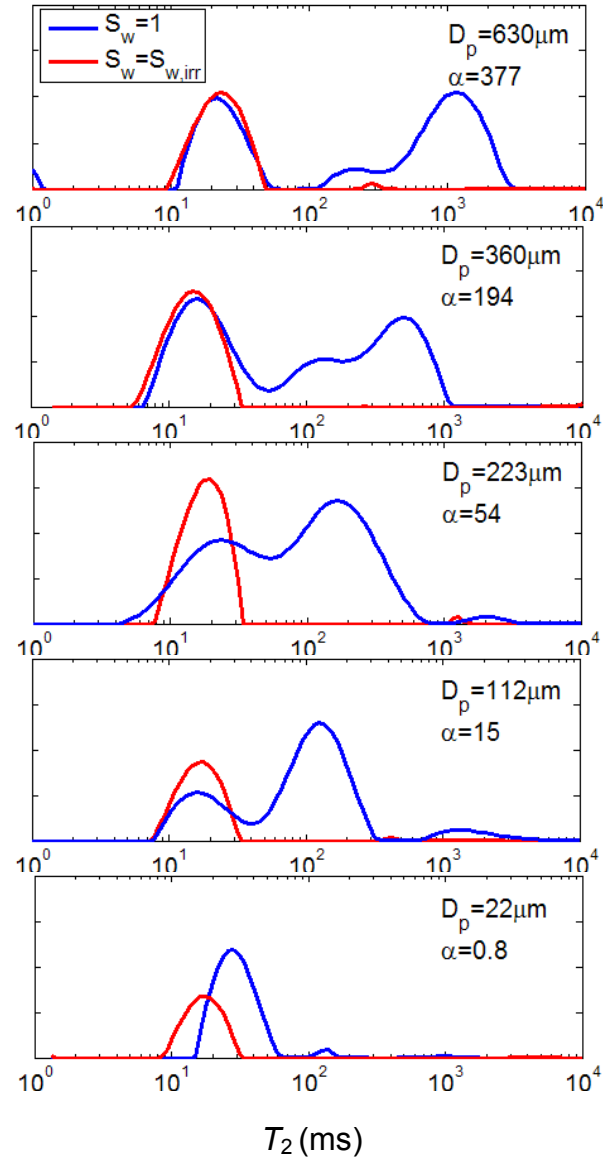


Fig. 14: T_2 distributions of microporous chalk as a function of grain diameter

We can see that for the two coarsest fractions, the T_2 distributions show distinct peaks for micro and macropores and the area under the micropore peak is the same as that at irreducible conditions. This implies that the systems are in the decoupled regime which is verified by large values of α_{grain} . The effect of coupling becomes more pronounced for medium coarse grains ($D_p=223\mu\text{m}$ and $112\mu\text{m}$), which show a build up of micropore peak amplitude at irreducible saturation. The values of α_{grain} now correspond to the intermediate coupling

regime. The total coupling regime is visible for finest fraction for which the T_2 distribution shows a unimodal behavior.

2. Silica Gels – A homologous series of silica gels with grain diameters of 335 μm , 110 μm and 55 μm constituted the second system. Figure 15 shows the T_2 distributions at 100% water saturation and at irreducible saturations for the three fractions. Similar to the response of chalk, the distributions change from being bimodal to unimodal with the decrease in particle diameter indicating increased coupling. The values of α_{grain} suggest intermediate coupling regime for the two coarsest fractions and total coupling regime for the finest fraction.

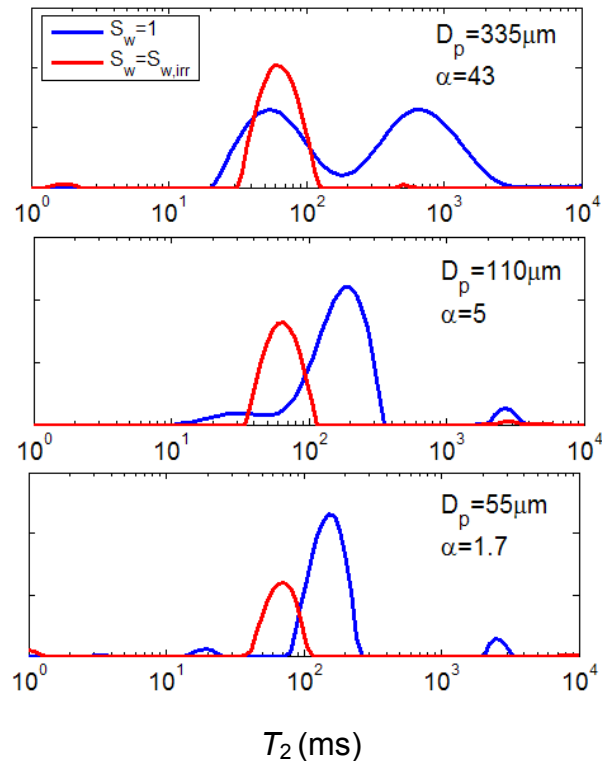


Fig. 15: T_2 distributions of silica gels as a function of grain diameter

3. Molecular sieves - The response of molecular sieves shows similar trend of narrowing T_2 distributions with decrease in grain diameter. The values of α_{grain} for the respective fractions predict the transition of the coupling regimes.

The lognormal and cubic relationships of Equations 17 and 19 also hold for the three systems (Figure 16) establishing the validity of the grainstone model.

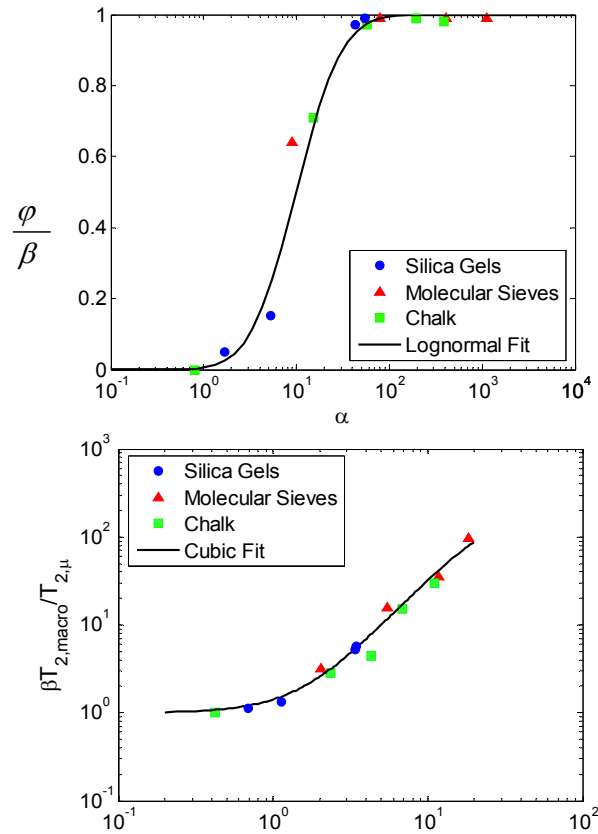


Fig. 16: The lognormal and cubic relationships hold for the grainstone systems.

ESTIMATION OF IRREDUCIBLE WATER SATURATION

The traditional method of estimating $S_{w,\text{irr}}$ employs a lithology-specific sharp $T_{2,\text{cutoff}}$ to partition the T_2 spectrum into free fluid and bound fluid saturations. For formations with diffusively coupled micro and macropores, the use of a sharp cutoff may give incorrect estimates since in such cases the direct relationship between pore size and T_2 distribution no longer holds.

In the case of pore coupling, the estimation of $S_{w,\text{irr}}$ amounts to the calculation of microporosity fraction β for a given T_1 or T_2 distribution at 100% water saturation. The solution of this inverse problem is obtainable by making use of the correlations for independent microporosity fraction and normalized macropore relaxation time (Equations 17 and 19). Three parameters are required for the solution: micropore peak amplitude (φ), relaxation time of micropore ($T_{2,\mu}$) and relaxation time of macropore ($T_{2,\text{macro}}$). It is assumed that $T_{2,\mu}$ is known from laboratory core analysis and is same for the formation. This assumption is justified if the formation has similar relaxivity and micropore structure as the cores. From the T_2 spectrum at 100% water saturation, the

values of φ and $T_{2,\text{macro}}$ can be calculated from the area under the micropore peak and the relaxation time of the mode of the macropore peak. Hence, for the given parameter values, the correlations can be simultaneously solved for the values of α and β . Graphically, the solution involves determining the intersection point of contours of φ and $T_{2,\text{macro}}/T_{2,\mu}$ on the α and β parameter space as shown in Figure 17. The values of contour lines for $T_{2,\text{macro}}/T_{2,\mu}$ differ by a factor of 2 and those for φ differ by 0.1. The coordinates of the intersection point of the contours for experimentally determined values of φ and $T_{2,\text{macro}}/T_{2,\mu}$ estimates the value of α and β for the formation. For a unimodal distribution with a zero value of φ (total coupling regime), the microporosity fraction can be calculated from the ratio of the relaxation times of micro and macropore, i.e.

$$\beta = \left(\frac{T_{2,\mu}}{T_{2,\text{macro}}} \right)_{\varphi=0} \quad (36)$$

In this case, the value of α is indeterminate and can be anything less than 1. This is because as φ approaches 0, the contours for $T_{2,\text{macro}}/T_{2,\mu}$ asymptote to the reciprocal β value independent of α .

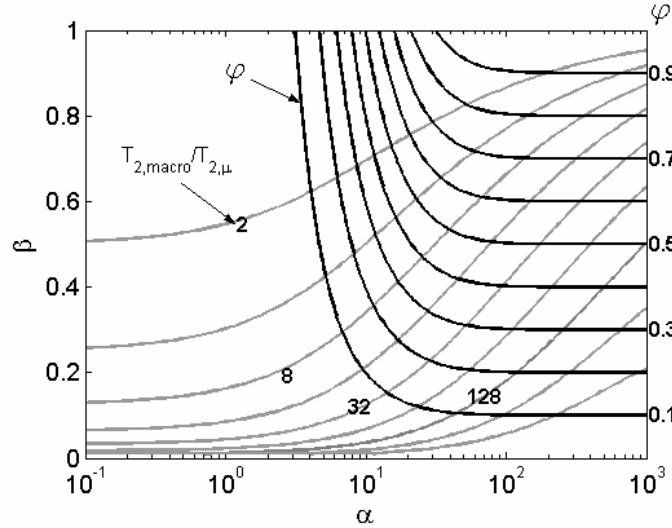


Fig. 17: Intersection of contours for correlations for φ and $T_{2,\text{macro}}/T_{2,\mu}$ estimates β for the formation.

Figure 18 shows the comparison of the calculated values of β and α with the values determined experimentally. An average value of $T_{2,\mu}$ obtained from the individual values for different sieve fractions or cores is used for calculations. The estimates lie within an average absolute deviation of 4% and 11% for β and α , respectively. This indicates that the technique is applicable to all the systems studied irrespective of the properties and coupling regimes.

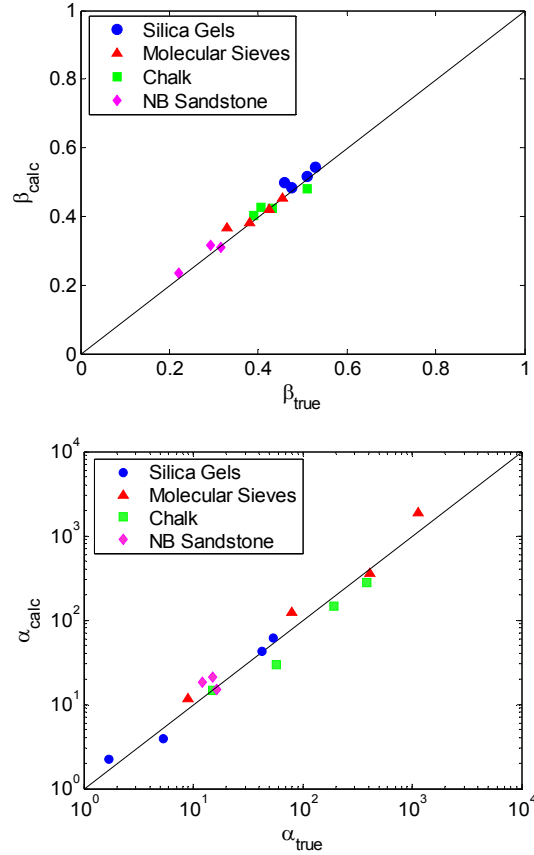


Fig. 18: β is estimated within 4% and α within 11% error for the systems studied.

Unification of spectral and sharp cutoff theory- The estimation of $S_{w,\text{irr}}$ using spectral or tapered $T_{2,\text{cutoff}}$ is based on the premise that each pore size has its own inherent irreducible water saturation. The fraction of bound water associated with each pore size is defined by a weighting function $W(T_{2,i})$ where $0 \leq W(T_{2,i}) \leq 1$. The $S_{w,\text{irr}}$ is then given as

$$S_{w,\text{irr}} = \sum_i^n W_i P_i \quad (37)$$

where n is the number of bins and P_i is the amplitude of each bin. The weighting factors are determined using empirical permeability models or cylindrical pore models (Coates et al., 1998, Kleinberg et al., 1997).

An implicit assumption of the above mentioned technique is that the producible and irreducible fractions of each pore have same relaxation time at 100% water saturation. However, the analysis of a single pore (see section on diffusional coupling) shows that the micro and macropore can communicate through decoupled and intermediate coupling regimes as well. Thus, in a general coupling scenario, the response of the pore shows distinct peaks for micro and macropore with amplitudes φ and $(1-\varphi)$ respectively. The amplitude φ can vary from 0 to β depending on the coupling regime. Therefore, the microporosity fraction coupled with the macropore amplitude is given as

$$\Phi\left(\frac{T_{2,\text{macro}}}{T_{2,\mu}}, \alpha\right) = \frac{\beta - \varphi}{1 - \varphi} \quad (38)$$

Φ is a function of the ratio of macro to micropore relaxation times and α which determines the microporosity fraction coupled with the macropore response. As α increases, the extent of pore coupling decreases and thus, the microporosity fraction coupled with the macropore response also decreases.

This is illustrated in Figure 19 where we plot Φ vs. the ratio of relaxation time of macro and micropore for different values of α . The curves show that a spectral or tapered cutoff is required for the estimation of irreducible saturation in total or intermediate coupling regime. The increase in the steepness of the curves with α indicates that lesser correction for diffusional coupling is required for large α . Once the pores are decoupled, a sharp cutoff is suitable for estimating irreducible fraction as illustrated by sharp fall of Φ curve to zero for $\alpha = 200$. This could also probably explain the suitability of a single lithology-specific $T_{2,\text{cutoff}}$ for estimating irreducible saturations when the formation is in decoupled regime irrespective of the properties. More experiments are, however, needed to prove this postulate.

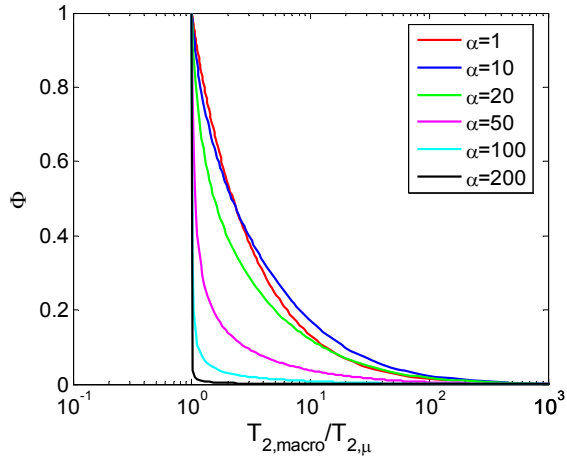


Fig. 19: Plot of Φ vs. $T_{2,\text{macro}}/T_{2,\mu}$ for different α . A spectral or tapered cutoff is required for the estimation of irreducible saturation in intermediate coupling regime. A sharp cutoff is applicable for decoupled regime.

CONCLUSIONS

The concept of diffusional coupling between micro and macropores for NMR relaxation has been numerically analyzed as a function of physical and geometrical parameters. The analysis, applicable to both microporous grainstones and clay-coated pores in sandstones, is shown to encompass previously described models. A coupling parameter α has been introduced

which helps to identify different regimes of pore coupling. Experiments with representative sandstone and grainstone systems prove the applicability of α to quantify the extent of coupling.

A new technique for the estimation of microporosity fraction and coupling parameter for the reservoir formation is also introduced. The parameters for the technique are easily obtainable from laboratory core analysis and the T_2 (or T_1) spectrum at 100% water saturation. Estimates of microporosity fraction for the sandstone and grainstone systems match within 4% deviation of the experimental values. It is also shown that α provides a quantitative basis for the application of spectral or sharp cutoffs.

ACKNOWLEDGMENTS

The authors would like to acknowledge the Consortium on Processes in Porous Media and US DOE DE-PS26-04NT15515 for financial support. We thank Jim Howard from Conoco Philips for providing North Burbank samples and Chuck Devier from PTS for making mercury porosimetry and permeability measurements.

References Cited:

- Brownstein, K.R. and Tarr, C.E., 1979, "Importance of Classical Diffusion in NMR Studies of Water in Biological Cells", Physical review A, Vol 19 (6), pp 2446-2453.
- Coates, G.R., Marschall, D., Mardon, D. and Galford, J., 1998, "A New Characterization of Bulk-Volume Irreducible using Magnetic Resonance", The Log Analyst, January-February, pp 51-63.
- Dunn, K.J., LaTorraca, G.A., Warner, J.L. and Bergman, D.J., 1994, "On the Calculation and Interpretation of NMR Relaxation Time Distributions", SPE 28367, paper presented at SPE ACTE, New Orleans, LA (25-28 September).
- Kleinberg, R.L. and Boyd A., 1997, "Tapered Cutoffs for Magnetic Resonance Bound Water Volume", SPE 38737, paper presented at the SPE ACTE, San Antonio, TX (5-8 October).
- Lindquist, W.B., Venkatarangan, A., Dundmuir, J. and Wong, T., 2000, "Pore and throat size distributions measured from synchrotron X-ray tomographic images of Fontainebleau sandstones", Journal of Geophysical research, Vol 105 (B9), pp 21509-21527.
- Peaceman, D.W. and Rachford, H.H., 1955, "The Numerical Solution of parabolic and elliptic Differential Equations", J. Soc. Indust. Appl. Math., Vol 3 (1), pp 28-41.
- Ramakrishnan, T.S., Schwatz, L.M., Fordham, E.J., Kenyon, W.E., and Wilkinson, D.J., 1999, "Forward Models for Nuclear Magnetic Resonance in Carbonate Rocks", The Log Analyst, Vol 40 (4), pp 260-270.

- Reid, R.C., Prausnitz, J.M. and Poling B.E., 1987, "The Properties of Gases and Liquids", McGraw Hill.
- Straley, C., Morriss, C.E., Kenyon, W.E., and Howard J.J., 1995, "NMR in Partially Saturated Rocks: Laboratory Insights on Free fluid Index and Comparison with Borehole Logs", The log analyst, January- February, pp 40-56.
- Todd, M.R., O'Dell, P.M. and Hirasaki, G.J., 1972, "Methods of Increased Accuracy in Numerical Reservoir Simulators", SPEJ December, pp 515-530.
- Trantham, J.C. and Clampitt, R.L., 1977, "Determination of Oil Saturation after Waterflooding in Oil-Wet Reservoir- The North Burbank Unit, Tract 97 Project", Journal of Petroleum Technology, Vol 29(1), pp 491-500.
- Zhang, G.Q., Hirasaki G.J. and House, W.V., 2001, "Effect of Internal Field Gradients on NMR Measurements", Petrophysics, Vol 42(1), pp 37-47.
- Zhang, G.Q., Hirasaki G.J. and House, W.V., 2003, "Internal Field Gradients in Porous Media", Petrophysics, Vol 44 (6), pp 422-434.

APPENDIX A

The dimensionless variables are given as

$$x^* = \frac{x}{L_2}, \quad y^* = \frac{y}{L_2}, \quad M^* = \frac{M}{M_o}, \quad t^* = \frac{t}{T_{2,c}} = \frac{t}{(L_1/\rho\beta)}$$

where M_o is the initial magnetization and $T_{2,c}$ is the characteristic relaxation time (Equation 6). The governing equations (3-5) in terms of the dimensionless variables are

$$\frac{\partial^2 M^*}{\partial x^{*2}} + \frac{\partial^2 M^*}{\partial y^{*2}} = \alpha \frac{\partial M^*}{\partial t^*} \quad (\text{A1})$$

$$\frac{\partial M^*}{\partial x^*} - \mu S(y^*) M^* = 0 \quad \text{at } x^* = 0, 0 \leq y^* \leq 1 \quad (\text{A2})$$

$$\frac{\partial M^*}{\partial x^*} = 0 \quad \text{at } x^* = \eta^{-1}, 0 \leq y^* \leq 1 \quad (\text{A3})$$

$$\frac{\partial M^*}{\partial y^*} = 0 \quad \text{at } y^* = 0 \text{ and } 1, 0 \leq x^* \leq \eta^{-1} \quad (\text{A4})$$

In the above system, the discontinuous boundary condition along the y -axis is combined into a single equation by using the step function $S(y^*)$ defined as

$$\begin{aligned} S(y^*) &= 1 && \text{for } 0 \leq y^* \leq \beta \\ &= 0 && \text{for } \beta < y^* \leq 1 \end{aligned} \quad (\text{A5})$$

APPENDIX B

Here, we resolve the issue of faster relaxation of micropore in the coupled case than in the decoupled case, observed in our simulations. For the case of no diffusional coupling, the dimensionless relaxation time of the micropore is inversely proportional to its surface-to-volume ratio i.e.

$$\lim_{\alpha \rightarrow \infty} T_{2,\mu}^* = \lim_{\alpha \rightarrow \infty} \frac{T_{2,\mu}}{T_{2,c}} = \frac{L_1/\rho}{L_1/\rho\beta} = \beta \quad (\text{B1})$$

Hence, when coupling between micro and macropore is allowed, the micropore is expected to relax slower than β . Figure 20 shows the relaxation time of micropore peak (normalized by β) as a function of α for different simulation parameters. We see that for the decoupled regime, the normalized micropore relaxation time tends to 1 as expected. But for the intermediate coupling regime, it appears that the micropore is relaxing faster than the decoupled rate. This artifact of faster relaxation of micropore in the coupled case was also observed in Ramakrishnan's analysis (1999). No explanation for the artifact was, however, offered in their paper.

The apparent contradiction can be resolved by studying the early relaxation data of the coupled pore. Analysis of the initial slope of the decay curve reveals that the micropore is indeed relaxing no faster than the expected rate. However, the decay curve has contribution from slow decaying component of the macropore and fitting the curve to multi-exponential fit has an apparent effect of reducing the relaxation time of the micropore.

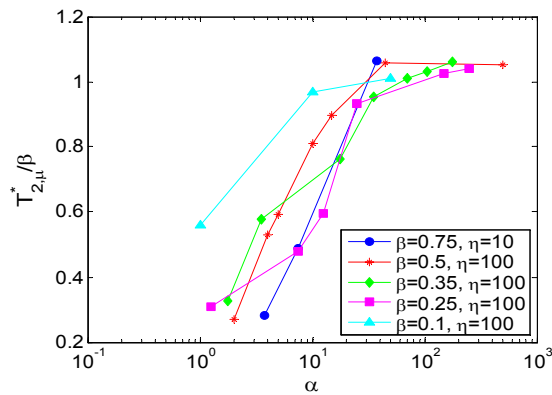


Fig. 20: Micropore appears to relax faster when coupled with macropore

Task 3: Characterization of pore structure and wettability.

The goal of this research is to relate NMR measurement to pore structure and wettability and thus to permeability and relative permeability. In Task 3, 2D pore structures will be extracted from thin-sections. The oil/brine/rock compositions will be related to wettability as determined by contact angle goniometry and atomic force microscopy. Amott wettability will be measured to define core scale wettability. Brine and oil NMR response of the cores will be measured. NMR response of surfactant solution imbibed carbonate cores will also be measured. NMR response will be simulated from pore images and wettability. Mechanistic correlations will be developed between NMR response, wettability and pore structure. Such correlation will help NMR logging define the variation of pore structure and wettability through all logged wells. Ten cores (five vuggy carbonate cores and five sandstone cores) and two reservoir oils will be used.

In Task 4, NMR response will be related to permeability and relative permeabilities. Such a correlation can estimate the reservoir heterogeneity and multiphase flow in logged but non-cored wells. The relative permeability functions determine the time for water breakthrough and the rate of oil recovery. Water-oil imbibition relative permeability will be measured for each core plug. Electrical conductivity will be measured at end-point saturations. Pore network models developed in Task 3 will be used to estimate the relative permeabilities and electrical conductivity. Correlations will be made among the NMR response and transport properties. Simple, but mechanistic correlations will be developed for NMR response, permeability and relative permeability.

The project started in the last quarter of last year. We have worked on three subtasks: pore structure, wettability and relative permeability/electrical conductivity of 5 carbonate cores. The activities are described in the next section.

II. Experimental

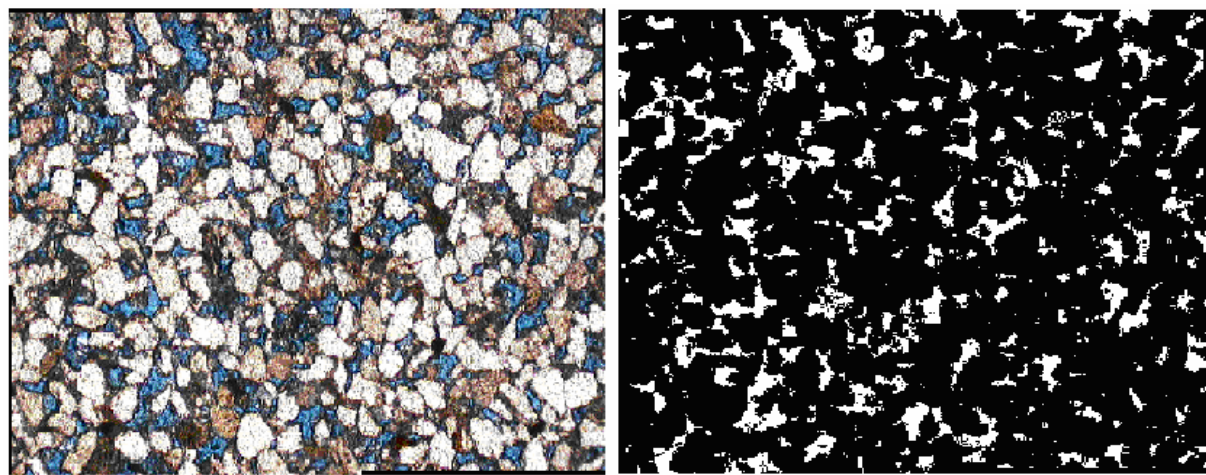
Six carbonate rock samples from a west Texas field were obtained. Thin sections were obtained from these samples. The thin sections were viewed by using an optical microscope at magnifications of 4X, 10X and 40X. The digital images were captured by using a CCD camera, and the video output signal was sent to a PC computer by using a frame-grabber PCI card. A computer controlled microscope stage was installed for automated image capture (Fig 1). Using this stage, 600 images (at 4X), each of 640 X 480 pixels, were taken to cover the entire thin section of about 1.5 cm X 1.0 cm at a high resolution. These images were then stitched using the Fourier Phase Correlation Method applied to the overlap region between images adjacent to each other. This resulted in images of about 10000 X 10000 pixels for each of the 6 carbonate thin sections at 4X magnifications. Similarly 3500 images at 10X magnification can be stitched together to produce images of 25000x25000 pixels.

Optical Magnification	Microns/Pixel
4X	3 $\mu\text{m}/\text{pixel}$
10X	1 $\mu\text{m}/\text{pixel}$
40X	0.3 $\mu\text{m}/\text{pixel}$

Figure 1: Imaging apparatus



Figure 2: Color image to B/W image conversion



These pictures were then segmented into pore space and solid by using the Color Cube selection Method (Fig 2). From 2D images of the rocks, we obtain the following statistical functions: porosity, 2- point autocorrelation function, chord length distribution, and lineal path length distribution (Fig 3). We have also calculated the power spectrum of the images using Fourier Transform (Fig 4). Image analysis using erosion-dilation algorithm results in the direct measurement of pore size distribution. The centroid of each pore has been used to estimate the diameter of the smallest sphere that can be fitted inside the pore to give the minimum pore diameter. The perimeter and area of pore from 2D image has been used as an indicator of surface area per unit volume of the pore space. Other pore-space properties like the minimum ferret diameter, maximum pore space diameter etc. have been estimated. Using these functions and applying heuristic methods such as simulated annealing, we reconstruct a 3D image having similar statistical functions of that of 2D image.

At present we are doing core flood studies on the 5 carbonate cores. The cores have been saturated in brine and the water permeability is being estimated using differential pressure measurement. A new core flood apparatus has been acquired with the capability of real time electrical conductivity measurement using 2 ring-electrodes connected with an LCZ meter. The whole set-up is interfaced with a PC computer using AD card for connecting pressure transducer and GPIB card for LCZ meter. Labview 6.1 is being used for automated data acquisition and online control (Fig 5). The pressure drop measurements are being used to estimate the permeability of cores while the electrical

conductivity measurements give the estimate of tortuosity. NMR measurements are also underway for the measurement of NMR response of the brine-saturated cores.

Figure 3: Statistical descriptor – Chord Length Distribution for sample 1.

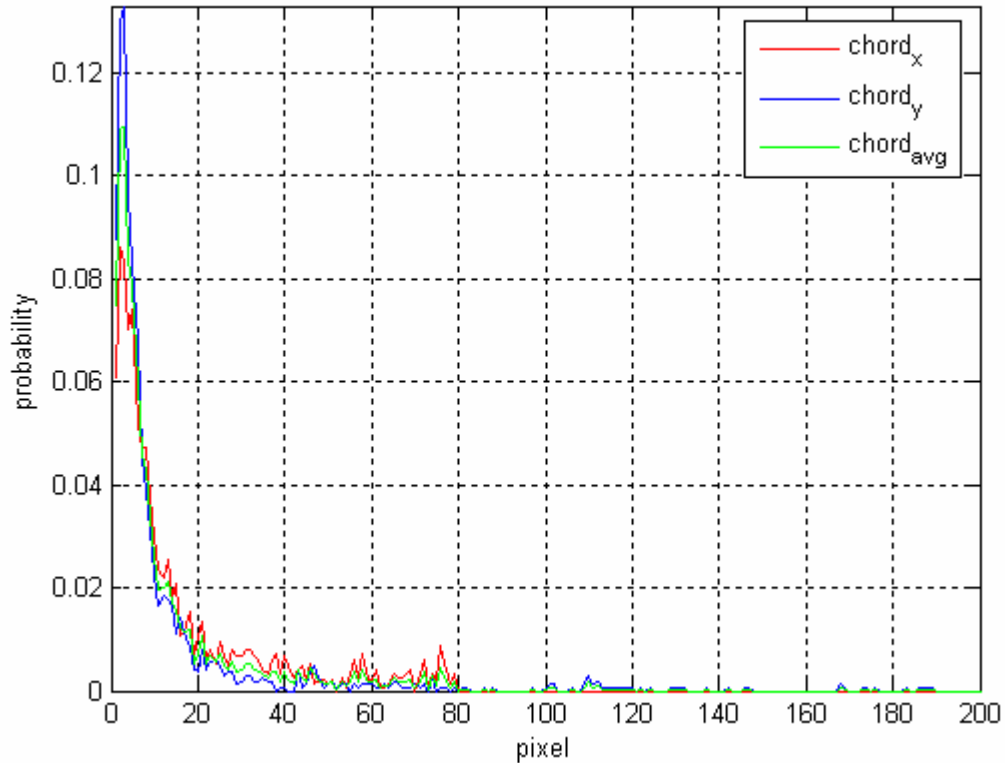


Figure 4: Fourier Power spectrum for sample image

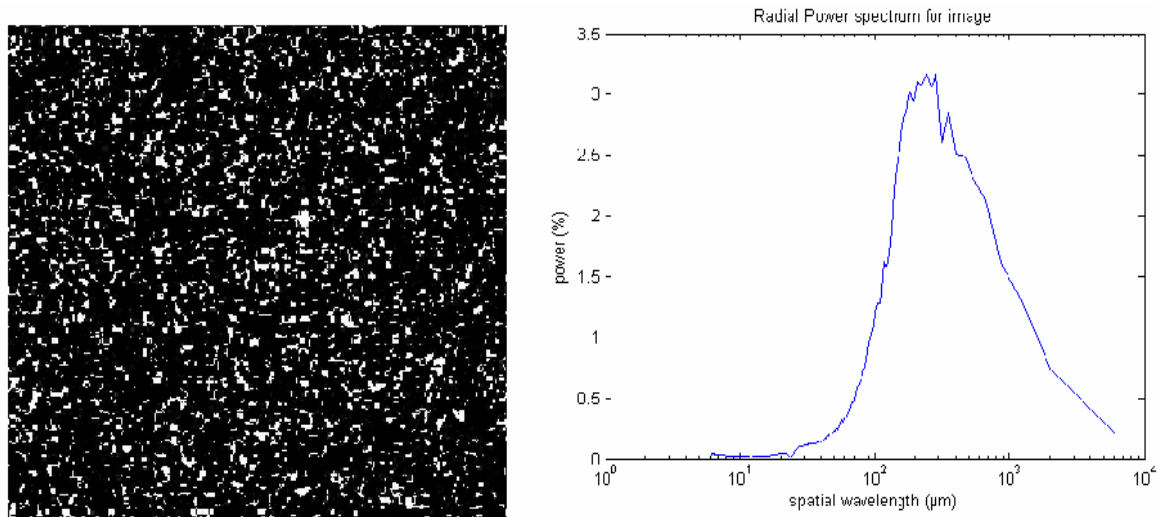
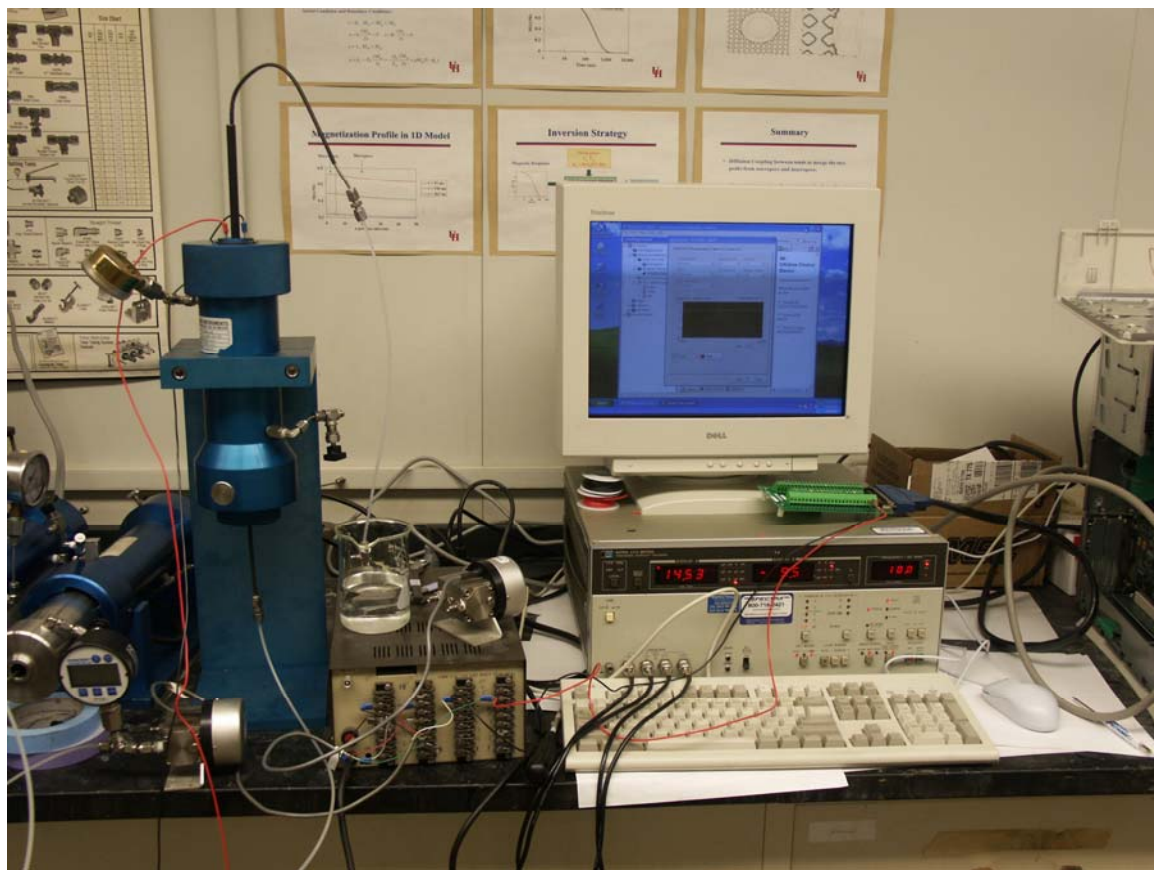


Figure 5: Core-Flood Apparatus with LABVIEW interface



III. Results

The routine data for these carbonate cores in the cleaned water-wet condition are listed in Table 1. Figure 6 shows the horizontal thin-section porosity contribution of each pore size of Sample 1. Figure 7 shows same data for its vertical thin-section. This sample is a peloid/fusulinid packstone/wackstone dolomite. The porosity is 15%. The matrix has very little intergranular porosity. The vugs are distributed more or less uniformly throughout the sample. Vugs are about 1 mm in size. There seems to be several micro fractures connecting the vugs. Thus the air permeability is high, 56 md.

Figure 6: Size distribution for Sample 1 horizontal thin section

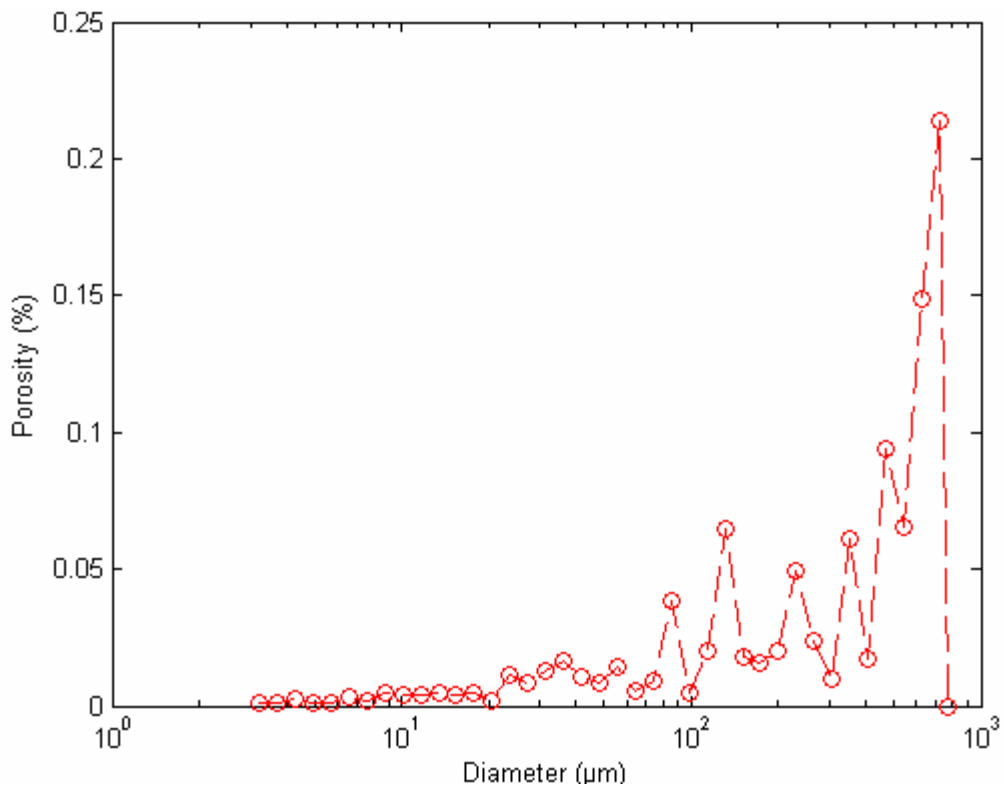


Figure 7: Size distribution for Sample 1 vertical thin section

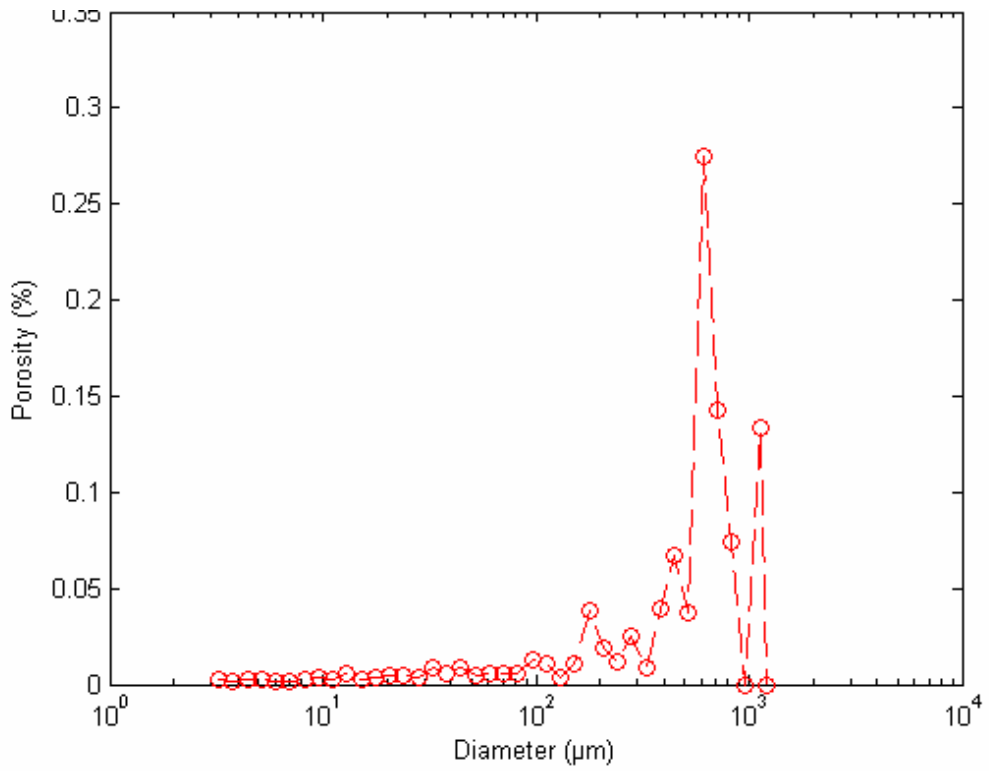


Table 1. Summary of routine core analysis data

<u>Sample</u>	<u>Porosity (%)</u>	<u>Air Permeability (md)</u>	<u>Soi</u>	<u>Sor</u>
1	15	56	33.7	23
2	7.4	0.023	22.8	20.7
3	6.6	0.022	44.2	26.5
4	6	0.08	26.8	14.4
5	15.7	140	45.2	26.9
6	21.8	2,321	51.7	41.7

Figure 8 shows the horizontal thin-section porosity contribution of each pore size of Sample 2. Figure 9 shows same data for the vertical thin-section. This sample is a fine peloid packstone/wackstone dolomite. The porosity is 7.4%. The matrix is filled with anhydride with intercrystalline pores. The vugs are small (<1 mm) and few. The vugs are connected through only very small intercrystalline pores, thus do not contribute to permeability. The permeability is 0.023 md.

Figure 8: Size distribution for Sample 2 horizontal thin section

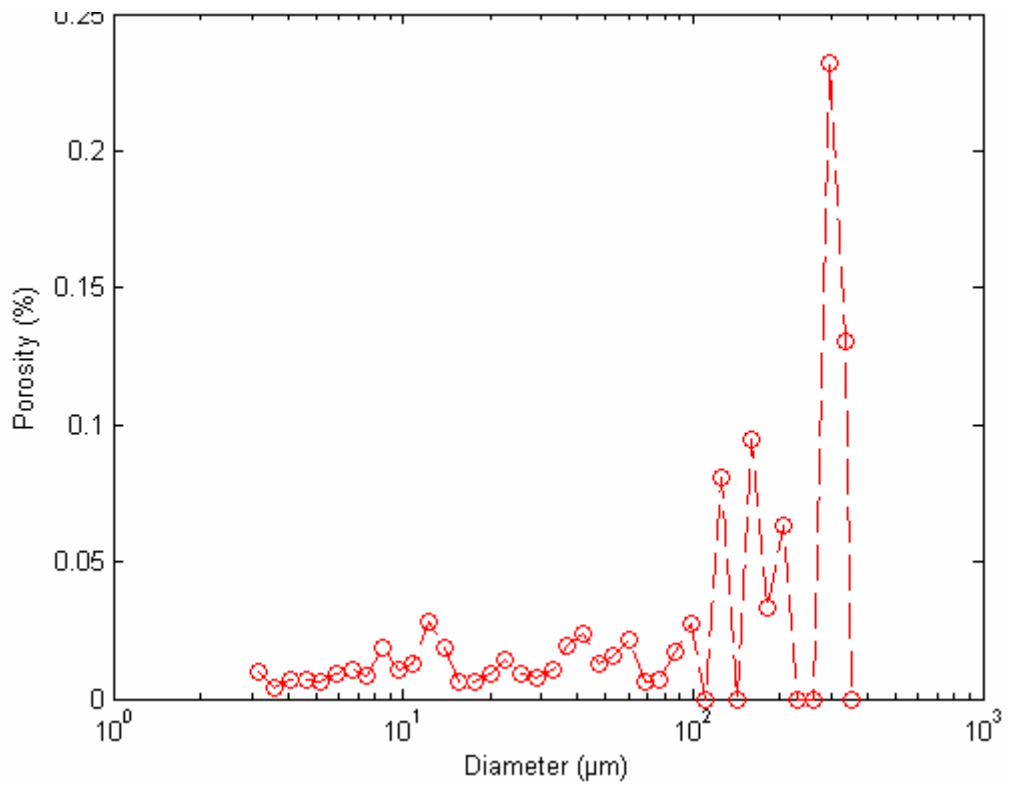


Figure 9: Size distribution for Sample 2 vertical thin section

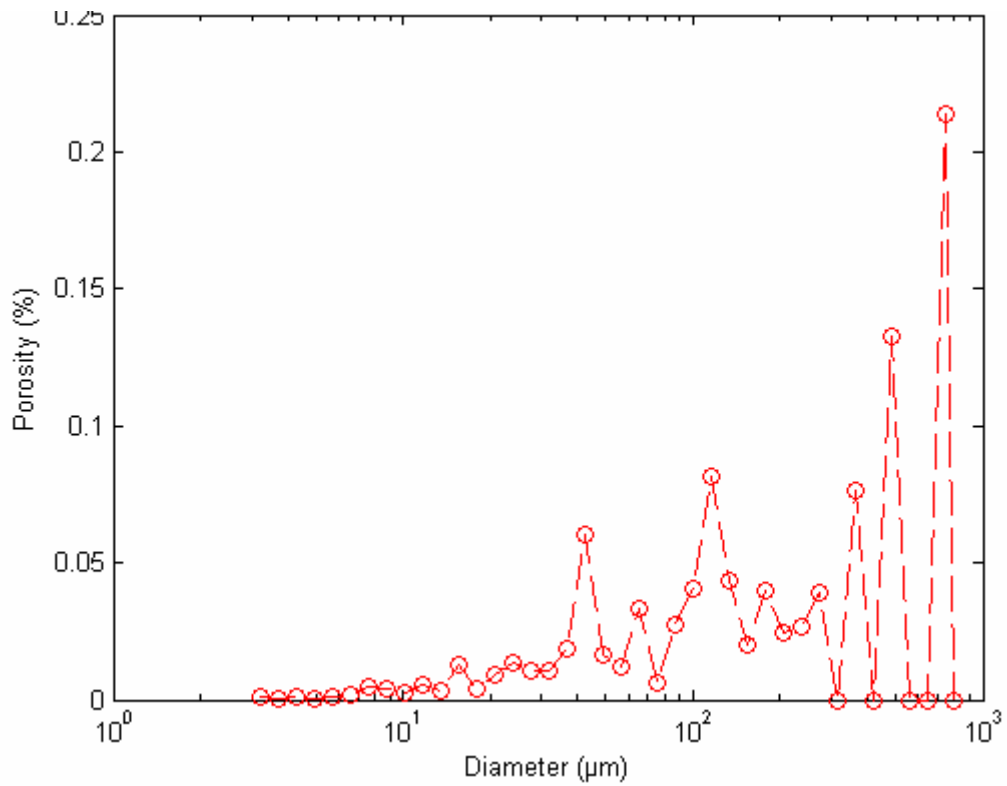


Figure 10 shows the horizontal thin-section porosity contribution of each pore size of Sample 3. Figure 11 shows same data for the vertical thin-section. The porosity is 6.6%. The vugs are large (1-5 mm), but connected through the intercrystalline pores which are very small. Thus the permeability is again very small, 0.022 md.

Figure 10: Size distribution for Sample 3 horizontal thin section

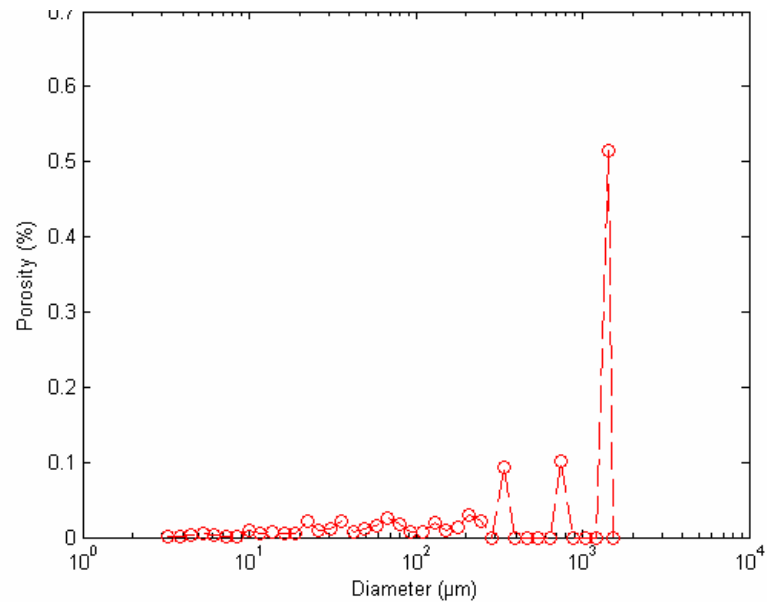


Figure 11: Size distribution for Sample 3 vertical thin section

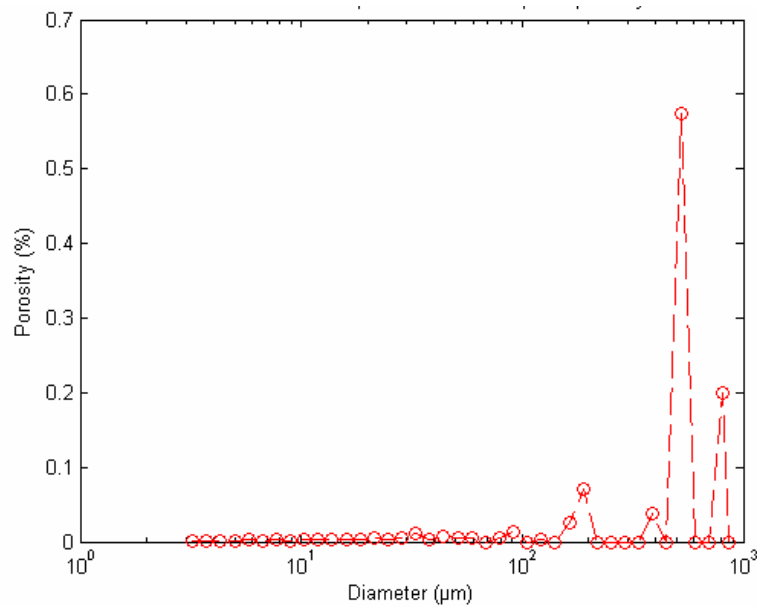


Figure 12 shows the horizontal thin-section porosity contribution of each pore size of Sample 4. Figure 13 shows same data for the vertical thin-section. The porosity is 6%. The vugs are large (1-20 mm) and connected through the intercrystalline pores, which are very small. The vugs do not contribute to permeability, which is 0.08 md.

Figure 12: Size distribution for Sample 4 horizontal thin section

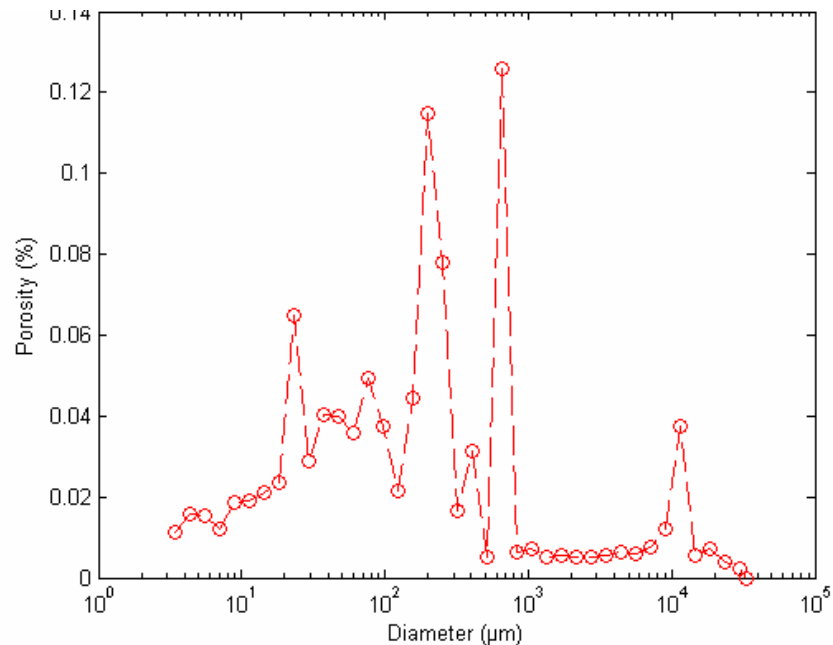


Figure 13: Size distribution for Sample 4 vertical thin section

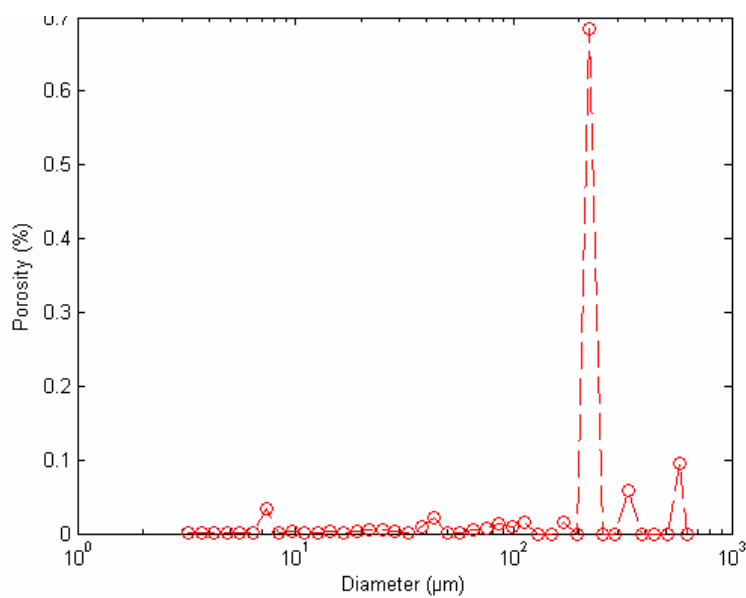


Figure 14 shows the horizontal thin-section porosity contribution of each pore size of Sample 5. Figure 15 shows same data for the vertical thin-section. Figures 16 and 17 show the same distributions for Sample 6. Both the samples 5 and 6 are very clumpy in appearance. The depositional texture cannot be seen. They look like breccia or agglomerate of different rocks. They may be formed from cave debris that recrystallized. Both samples have a lot of intergranular porosity that forms an interconnecting flow network as observed from the thin section images. Both samples are vuggy, with bigger vugs in Sample 6. The porosity and permeability for sample 5 are 15.7% and 140 md. The vugs are connected through large pores (10-100 μm range) leading to high permeability. The porosity and permeability for sample 5 are also high, 21.8% and 2,321 md. We are working on developing three-dimensional pore geometry from two-dimensional image analysis.

Figure 14: Size distribution for Sample 5 horizontal thin section

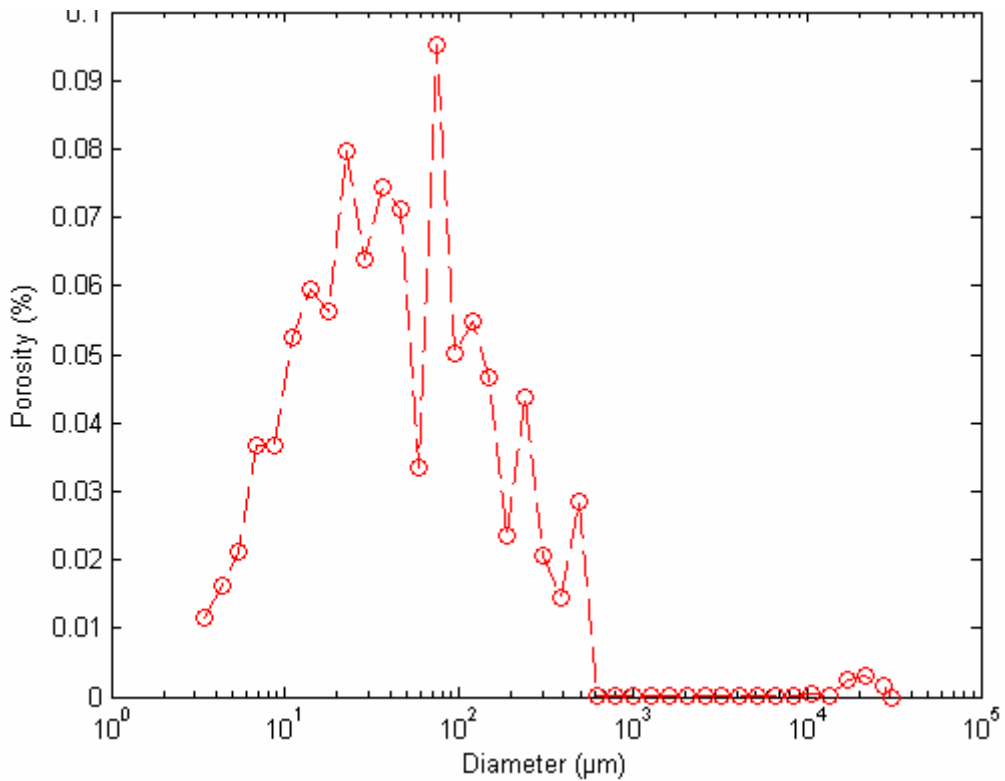


Figure 15: Size distribution for Sample 5 vertical thin section

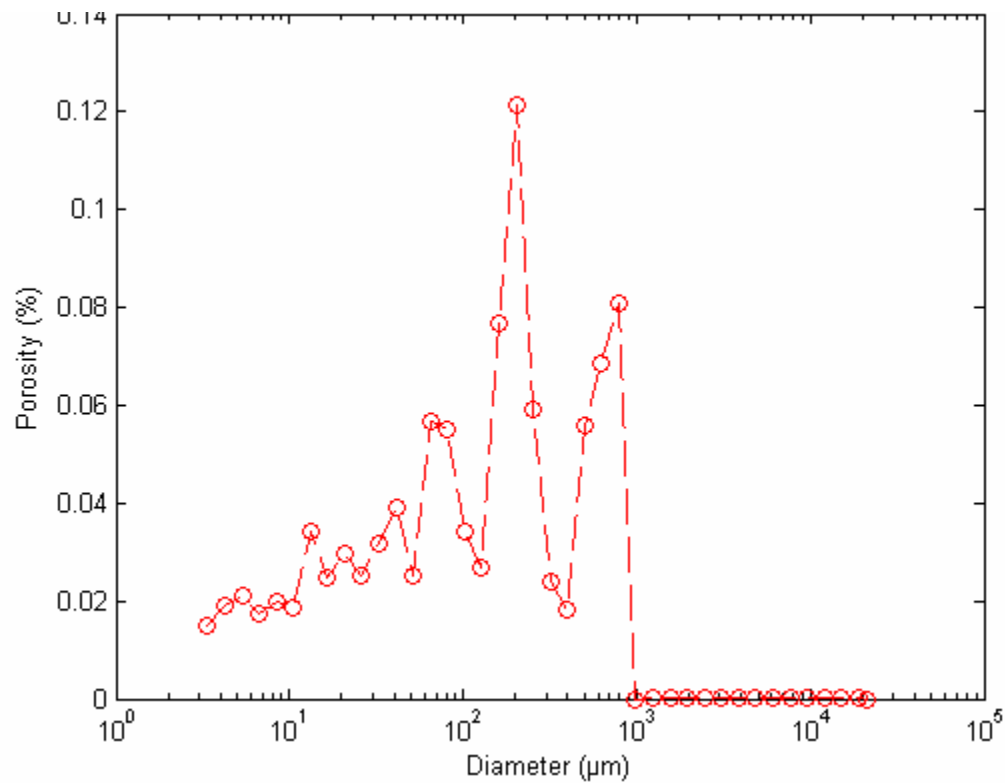


Figure 16: Size distribution for Sample 6 horizontal thin section

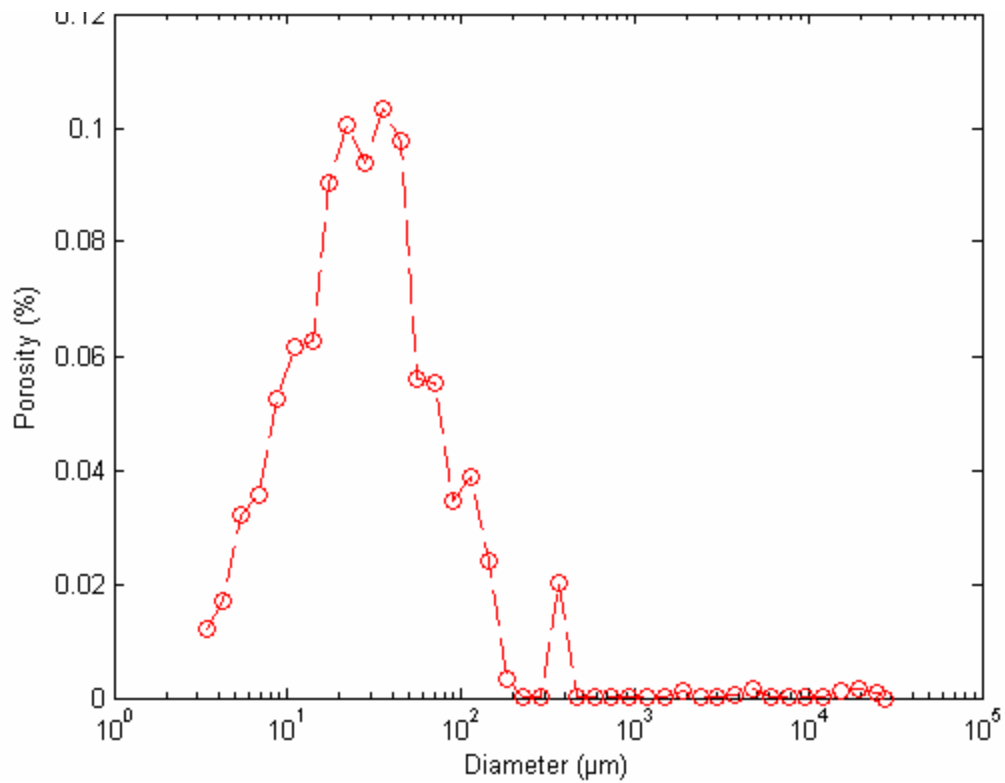
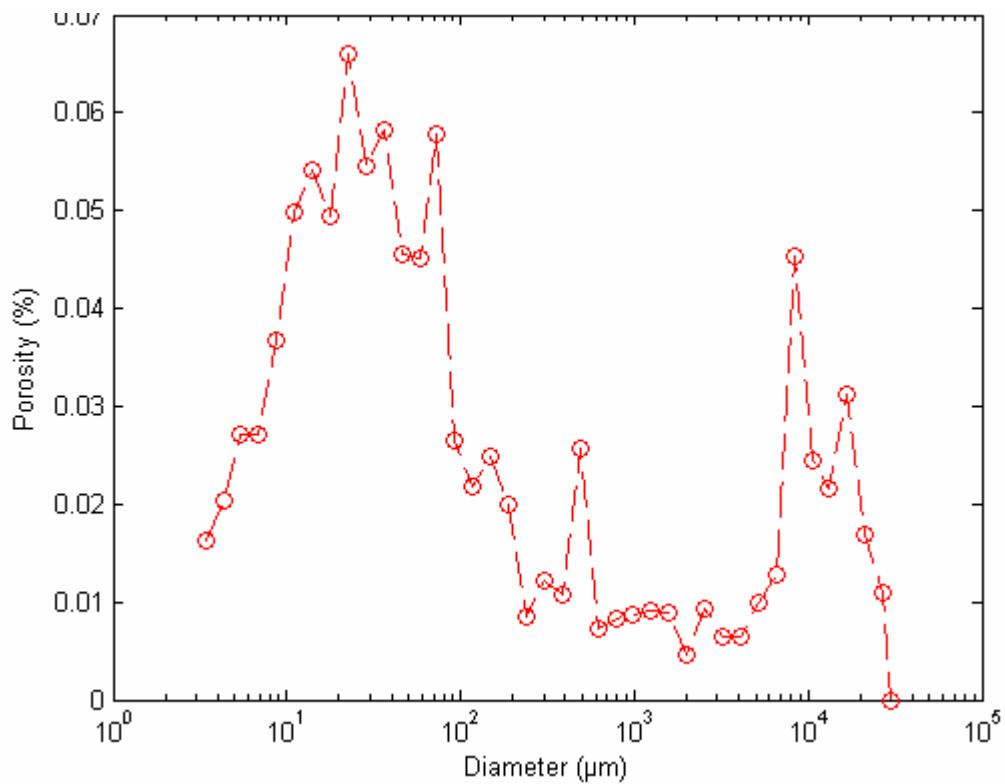


Figure 17: Size distribution for Sample 6 vertical thin section



A coreflood apparatus is assembled that can also be used for measuring electrical conductivity. Figure 18 shows the pressure drop in a carbonate core sample of length 2 inches and diameter 1.5 inches as the brine injection rate is increased. Figure 19 shows the electrical resistance, which is independent of brine flow rate. The carbonate cores will be flooded with oil and the electrical conductivity will be measured as a function of brine saturation.

Figure 18: Pressure drop and resistance as a function of brine flow rate

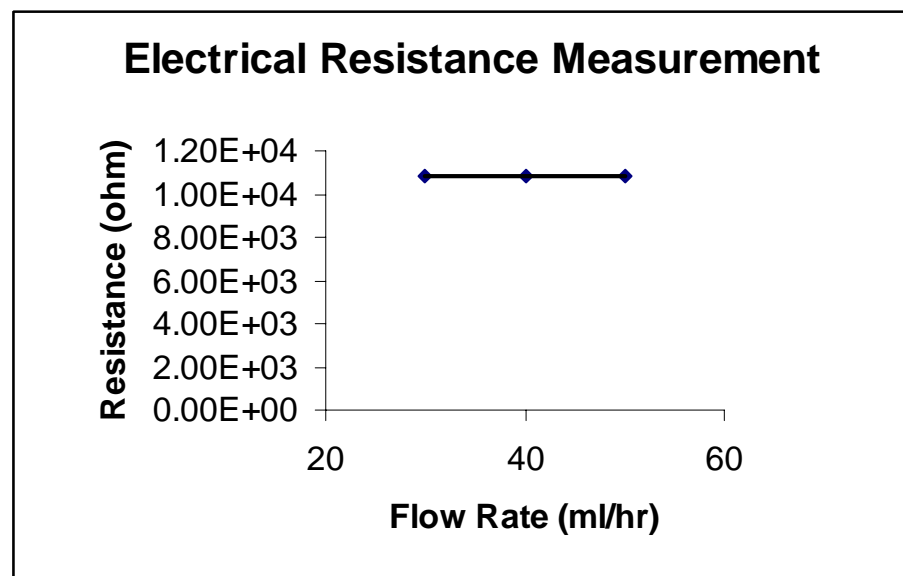
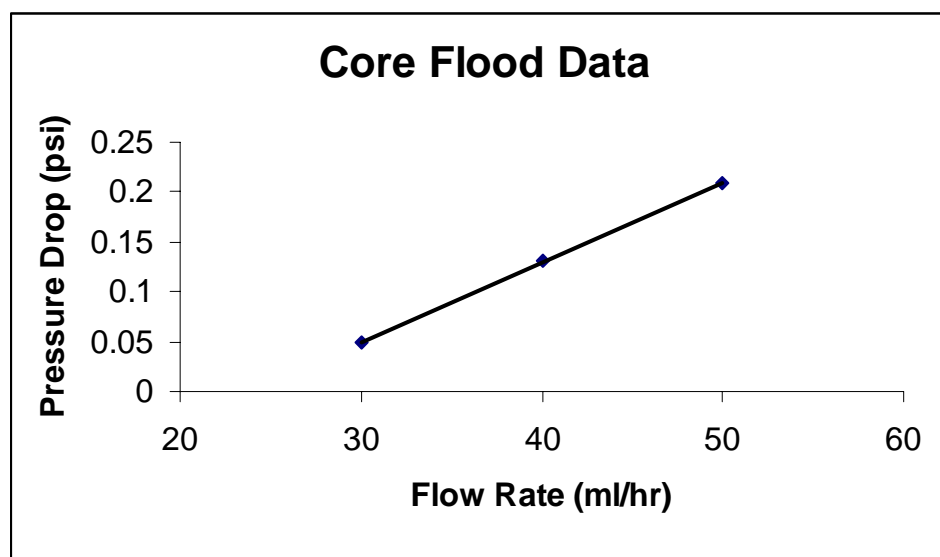


Figure 19: The NMR T₂ measurement and D-T₂ map for sample 4

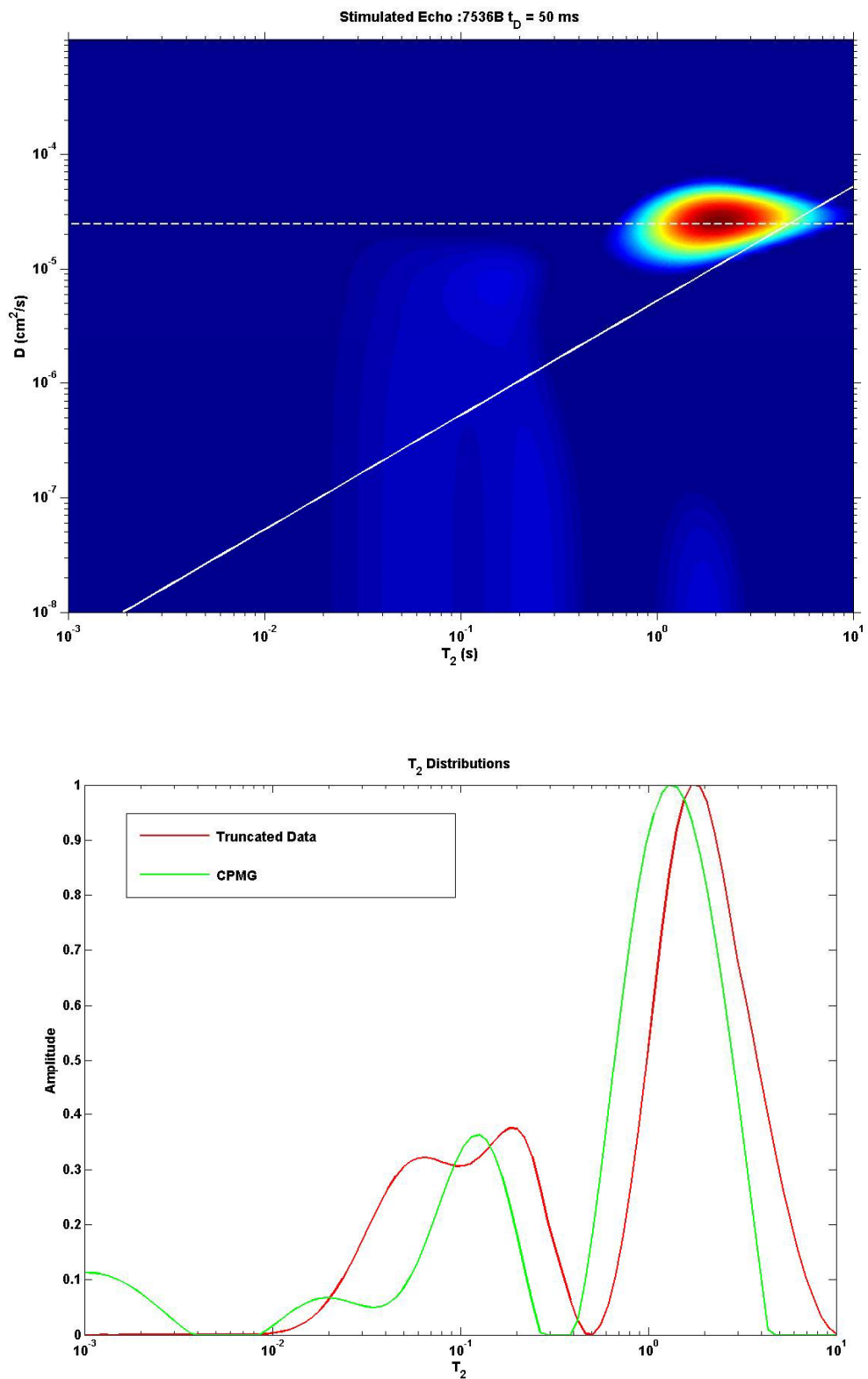


Figure 19 shows the NMR D-T2 map and T2 distribution for sample 4 completely saturated with brine. The color in the D-T2 map signifies the amplitude (or probability) at a particular D and T2. Red is the highest amplitude; blue is the lowest. The dashed line signifies molecular diffusivity of water. The slanted line is the so-called “dead oil line” on which signals from typical dead oils lie. As can be seen in Figure 19, the diffusivity of the water in the sample is close to that of bulk water. When the core is partially saturated with water and oil, the diffusivity signal from NMR can be used to identify the fluids. The T2 distribution peaks around 2-3 sec, the decay time for bulk water in vugular pores. The projection of map amplitudes on to the T2 axes (integration over the diffusivity axis) is plotted in the bottom graph. The T2 distribution is compared with that obtained directly from a CPMG pulse sequence. There is a shift in the signal whose origin is being studied.

IV. Conclusions

Characterization of pore structure has been completed on 6 carbonate samples. The vug size, distribution and interconnection vary significantly in these six samples. The thin sections have been characterized through their two-point correlation function, chord size distribution and lineal path function. The image analysis using Fourier transform and erosion-dilation algorithms has been completed. The work on NMR response, electrical conductivity and brine permeability has been initiated. We are working on reconstructing three-dimensional pore structures, wettability and relative permeability of these rock samples.

V. Plans for Next Reporting Period

- Wettability of carbonate samples (Sub-Task 3.2)
- NMR response of carbonate samples (Sub-Task 3.3)
- Relative permeability/conductivity of carbonate samples (Sub-Task 4.1)
- Pore-Network Modeling (Sub-Task 4.2)
- Permeability / Relative Permeability Correlation (Sub-Task 4.3)